Thesis for the Degree of Doctor of Philosophy

Design and Development of Confocal Off-axis Reflective System for Space Telescopes

Woojin Park

School of Space Research

Graduate School

Kyung Hee University

Seoul, Korea

August, 2020

Design and Development of Confocal Off-axis Reflective System for Space Telescopes

Woojin Park

School of Space Research

Graduate School

Kyung Hee University

Seoul, Korea

August, 2020

Design and Development of Confocal Off-axis Reflective System for Space Telescopes

by
Woojin Park

Advised by

Dr. Soojong Pak

Submitted to the School of Space Research
and the Faculty of the Graduate School of
Kyung Hee University in partial fulfillment
of the requirements for the degree of
Doctor of Philosophy

Dissertation Committee:

Dr. Ho Jin (Chairman)

Dr. Soojong Pak

Dr. Jongho Seon

Dr. Bongkon Moon

Dr. Sungho Lee

Contents

List of Figures

List of Tables

Abstract

Design and Development of Confocal Off-axis Reflective System for Space Telescopes

By Woojin Park
Doctor of Philosophy
Graduate School of Kyung Hee University
Advised by Dr. Soojong Pak

The optical system development is an interdisciplinary study of optics, mechanics, electronics, etc. Over the last decade, the optical system is tremendously developed in both industry and research. Especially, astronomical telescopes become a large and compound system, so they require high-end technology over many research fields. In this thesis, the optical system design and evaluation process for astronomical telescopes is introduced including optical design, tolerance analysis, alignments, performance tests, optical characterization, optomechanics design and analysis, and stray light suppression. Simple optical theories and aberrations are also summarized for the research backgrounds. This thesis refers to two main optical systems, Linear Astigmatism Free-Three Mirror System (LAF-TMS) and the limb telescope of the Mesospheric Airglow/Aerosol Tomography Spectroscopy (MATS) satellite, that are linear-astigmatism-free confocal off-axis systems applied for ground and space applications, respectively. Both systems provide high optical performance over a wide field of view thanks to their innovative linear-astigmatism-free configuration. Optical design, alignments, and mirror and optomechanical designs follow unconventional methods because of the confocal off-axis optical design. Transformable Reflective Telescope (TRT) Kit, which is an optical experiment kit, is also shown for alignments, stray light analysis, and baffle design. All methods introduced in this thesis are applicable not only to linear-astigmatism-free off-axis systems but to traditional telescope systems.

Chapter 1

Introduction

The design and the fabrication of an optical system have been improved for many years. Development of the optical system contributes to building larger and more accurate telescopes, and it activates modern astronomy and space science research. The first telescope was invented by Hans Lippershey from the Netherlands in 1609. He used two lenses for a magnification of about three. In the same year, Galileo Galilei made his version of a refractive telescope. However, the first generation of refractive telescopes is limited by chromatic aberration, so Christiaan Huygens builts the long focal length telescope with 10 cm diameter and 7 m focal length to reduce the aberration.

Reflective telescopes, which use optical mirrors instead of using lenses, can avoid the chromatic aberration. From 1663, James Gregory, Sir Isaac Newton, and Laurent Cassegrain invented their reflective telescopes, so they are called Gregorian, Newtonian, and Cassegrain telescopes, respectively. Based on these reflective telescopes, several modified two mirror systems have been developed such as Ritchey-Chrétien, Dall-Kirkham, etc.

By comparing to refractive telescopes, traditional reflective telescopes, also called on-axis reflective system, has a huge disadvantage from obscuration, scattering, and diffraction of the incident light by the secondary mirror. It degrades image quality and is particularly critical for observations of low brightness objects or extremely bright targets like the sun.

The on-axis reflective system is also limited to narrow field of view observations due to the size of the secondary mirror.

Classical off-axis (a.k.a. common off-axis) design avoids the obscuration problem, but it still has limitations for wide field of view observations because linear astigmatism becomes dominant in the image and degrades image quality significantly. Recently, linear-astigmatism-free confocal off-axis reflective system is starting to develop to overcome the critical optical aberration.

These days, meter-class large telescopes are popular to observe and study the early universe. Most of the large telescopes are reflective systems because optical mirrors are much easier to fabricate than lenses in large. Now, we are about to observe the universe with larger than 20 m aperture sized telescopes, e.g. Giant Magellan Telescope (24.5 m), Thirty Meter Telescope (30 m), and Extremely Large Telescope (39.3 m). These modern telescopes are complex systems that require an interdisciplinary research of optics, mechanics, electronics, computer engineering, etc.

In this thesis, three optical systems are introduced, Linear Astigmatism Free-Three Mirror System (LAF-TMS), the limb telescope of the Mesospheric Airglow/Aerosol Tomography Spectroscopy (MATS) satellite, and Transformable Reflective Telescope (TRT) Kit, that are developed with the interdisciplinary research of optics and mechanics.

LAF-TMS and the MATS satellite are linear-astigmatism-free confocal off-axis three mirror telescopes. LAF-TMS is designed for the wide field of view infrared satellite for all-sky surveys. It has an entrance pupil diameter of 150 mm, a focal length of 500 mm, and field of view of $5.51^\circ \times 4.14^\circ$. Therefore it is appropriate for wide field of view Pa-α galactic plane survey, all-sky brightness of zodiacal emission observations, Cosmic Infrared Background (CIB) observations, etc.

The MATS satellite is a Swedish microsatellite mission that observes noctilucent clouds (NLCs) (80-86 km altitudes) and O_2 atmospheric band dayglow/nightglow (75-110 km altitudes) over a wide field of view ($5.67^\circ \times 0.91^\circ$) in two ultraviolet (UV) channels and four infrared (IR) channels within a wavelength range between 270 and 772 nm. The main

optical system of the MATS satellite is the limb-viewing telescope, which is designed with a 35 mm entrance pupil diameter and a focal ratio of 7.4.

The TRT Kit is a transformable telescope that is reconfigured to Newtonian, Cassegrain, and Gregorian optical systems by simply changing the secondary mirror. This telescope is developed for an educational purpose and for performing various optical tests such as mirror surface error measurements, alignment module tests, and stray light measurements.

This thesis summarizes the process of optical system design and evaluation for these three ground and space based astronomical telescopes including optical design, tolerance analysis, alignments, optical tests, characterizations, optomechanical design, finite element analysis, stray light analysis, and baffle design (the blue area in Figure 1.1).

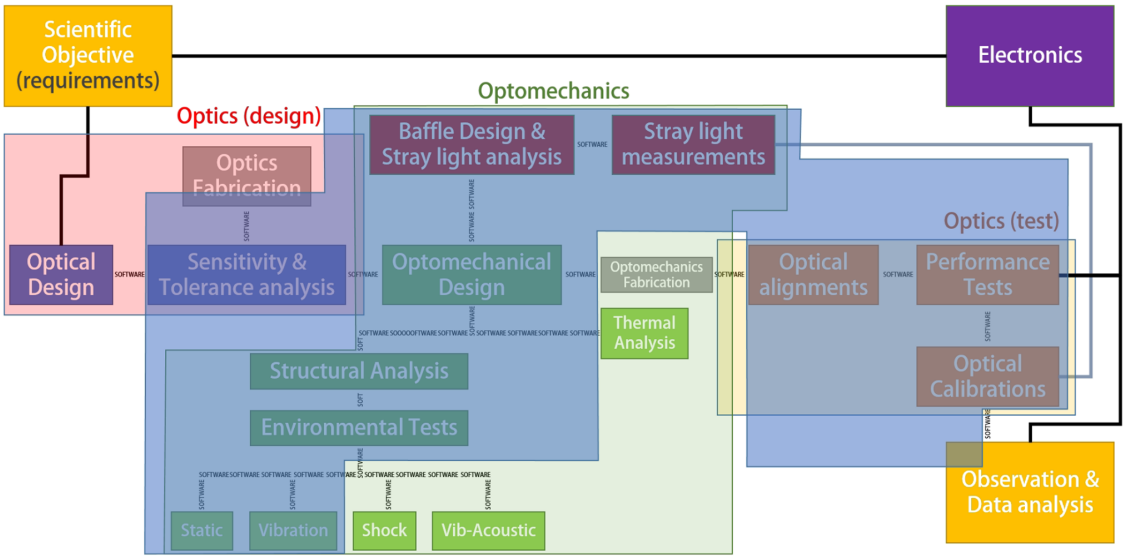

Figure 1.1: Research fields for the developing optical telescope system. The blue area indicates research fields which this thesis covers.

Chapter 2

Geometrical Optics

An optical system consists of optical and optomechanical elements in order to control the light. It includes mirrors, lenses, gratings, detectors, filters, housings, baffles, etc. Geometrical optics explains the propagation of the light in terms of rays to understand the basics of the light refraction and reflection. Most of optical designs use ray-tracing software such as CODE V and OpticStudio (ZEMAX). They automatically calculate optical parameters, and even optimize or suggest better design configurations. However, the basic layout of the elements should be established based on first order optical parameters such as focal length, entrance pupil diameter, magnification, among others.

The optical parameters and first order optical equations are defined with the Cartesian coordinate system (Figure 2.1) and sign convention that is the rule of the optical parameters of sign. In optics, the Cartesian sign convention is commonly used for measuring distances, heights, angles, etc. following the rules below:

- The origin of the Cartesian coordinate system (O) is the center of the optical component.
- The distance along the z-axis (s) is positive, and measured in the reverse direction of the ray is negative.
- Ray height along the y-axis (y) is positive for above the optic axis, and negative for

below the axis.

- Slope angles (u, k, and ϕ) are positive for a counterclockwise rotation of the corresponding ray to the optic axis.
- Incidence and reflection (or refraction) angles, i, are positive for a clockwise rotation of the corresponding ray to the line PC.
- The radius of curvature (R) is positive when the center of the curve (C) is on the right side of the center of the optical component (O).
- Focal length (f) is positive for the converging light by the convex lens or the concave mirror.
- The names of parameters after reflection (or refraction) add prime ($'$) from the names just before reflection (or refraction).

Note that, two focal lengths (f) in the top and bottom layouts of Figure 2.1 are positive, even though the focal position is located on the left side of the origin (O) for the reflecting system (bottom).

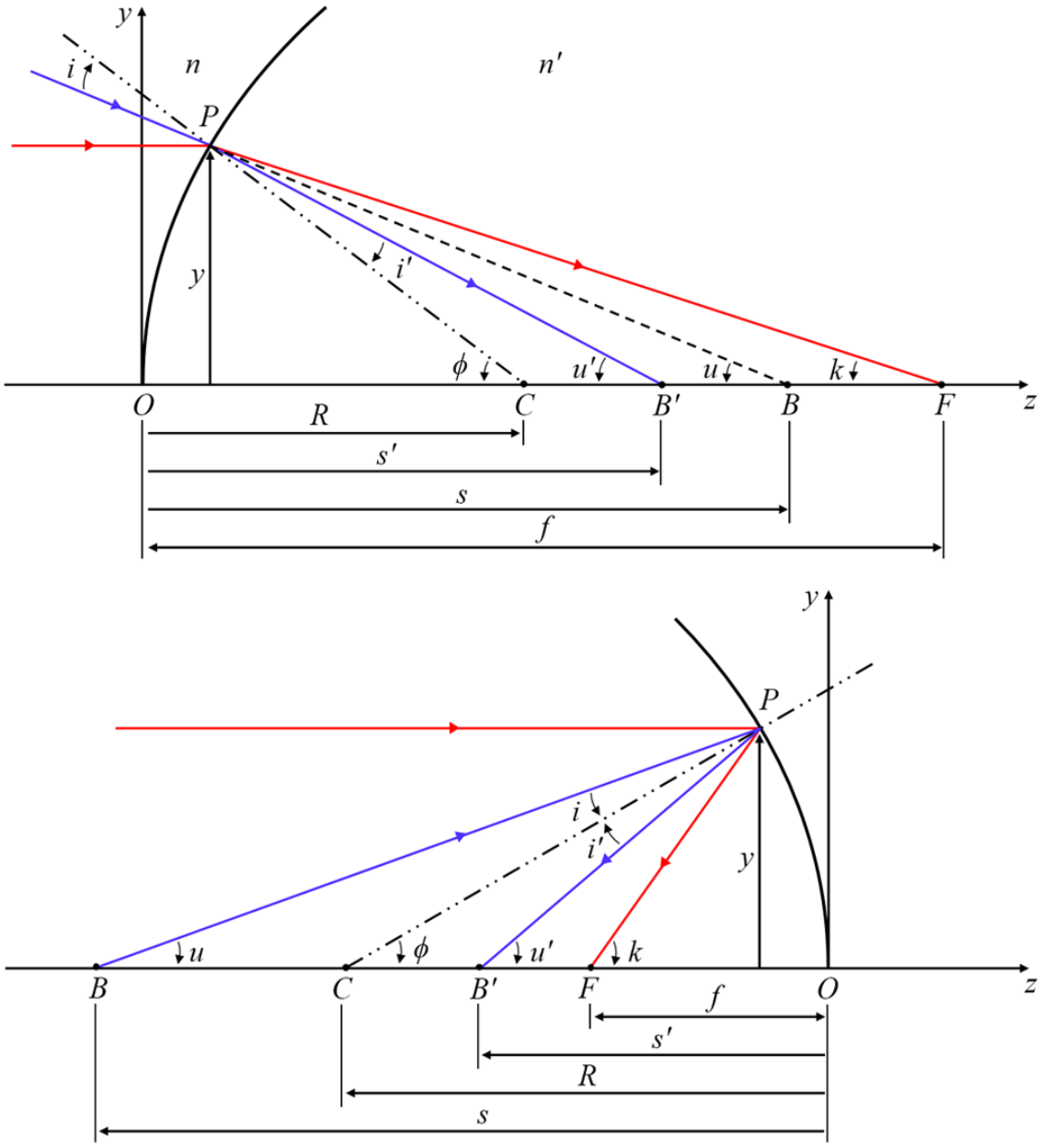

Figure 2.1: Refraction (top) and reflection (bottom) at the spherical surface. The red incident light is parallel to the optical axis.

2.1 Paraxial equations

The principal equations of geometrical optics are based on Gaussian optics that describes optical layout of the system when ray height (y) and all angles are small enough. If the point P is close enough to point O, ray height and angles approximate to zero, and trigonometric functions are expressed by

$$\sin\theta = \theta - \frac{\theta^3}{3!} + \frac{\theta^5}{5!} - \frac{\theta^7}{7!} + \cdots \approx \theta \tag{2.1.1}$$

$$\cos\theta = 1 - \frac{\theta^2}{2!} + \frac{\theta^4}{4!} - \frac{\theta^6}{6!} + \cdots \approx 1 \tag{2.1.2}$$

$$\tan\theta = \theta + \frac{\theta^3}{3} + \frac{\theta^5}{5} + \frac{\theta^7}{7} + \cdots \approx \theta \tag{2.1.3}$$

which in the paraxial approximation of terms become $\sin\theta = \theta$, $\cos\theta = 1$, and $\tan\theta = \theta$.

Snell's law describes the relationship between incident and refraction angles of the light when the light propagates into the interface of lens, water, air, or the other media.

$$n\sin i = n'\sin i' \tag{2.1.4}$$

where, n and n' are the refractive index of the media. Snell's law in the paraxial approximation becomes

$$ni = n'i'. \tag{2.1.5}$$

From the top layout Figure 2.1, we derive

$$i = \phi - u, \qquad i' = \phi - u'. \tag{2.1.6}$$

Substituting into Equation 2.1.5, gives

$$n(\phi - u) = n'(\phi - u') \tag{2.1.7}$$

$$nu - n'u' = \phi(n - n'). \tag{2.1.8}$$

Applying the paraxial approximation to the layout in Figure 2.1, we derive

$$\phi = \frac{y}{R}, \qquad u' = \frac{y}{s'}, \qquad u = \frac{y}{s} \tag{2.1.9}$$

and, combining Equation 2.1.8 and 2.1.9

$$n\Big(\frac{y}{s}\Big) - n'\Big(\frac{y}{s'}\Big) = \frac{y}{R}(n - n') \tag{2.1.10}$$

$$\frac{n}{s} - \frac{n'}{s'} = \frac{n - n'}{R}. \tag{2.1.11}$$

Image distance (s') becomes the focal length (f), $s' = f$, when object distance (s) is infinite, and vise versa.

Paraxial equations for the reflective system is also derived in the same way. Optical parameters for reflective systems (bottom in Figure 2.1) in consideration of the sign convention are

$$i = \phi - u, \qquad i' = u' - \phi, \qquad \phi = \frac{y}{R}, \qquad u' = \frac{y}{s'}, \qquad u = \frac{y}{s}. \tag{2.1.12}$$

From the Snell's law (Equation 2.1.5), we derive

$$n(\phi - u) = n'(u' - \phi). \tag{2.1.13}$$

Refractive indexes for the reflective system are the same before and after the reflection, $n = n'$. Therefore,

$$\phi - u = u' - \phi \tag{2.1.14}$$

$$u + u' = 2\phi \tag{2.1.15}$$

$$\tag{2.1.16}$$

The focal length (f) of the optical system is one of the key optical parameter that measures how powerfully the system converges or diverges the incident light. So, it is also related to optical power (P),

$$f = -\frac{n}{P}. \tag{2.1.17}$$

Applying law of reflection and paraxial approximation, k is equal to 2ϕ. Thus the focal length for the reflecting system with the spherical surface is half of the radius of curvature (R), $R = 2f$. So,

$$\frac{1}{s} + \frac{1}{s'} = \frac{2}{R} = \frac{1}{f}. \tag{2.1.18}$$

The focal length in the thick lens system is defined with the distance from a principal plane to the focus (see, Figure 2.4).

2.2 Other optical equations

2.2.1 Magnification

The optical system magnification represents the ratio of optical parameters in an object frame to its in an image frame. Figure 2.2 is the layout of lateral and angular magnifications.

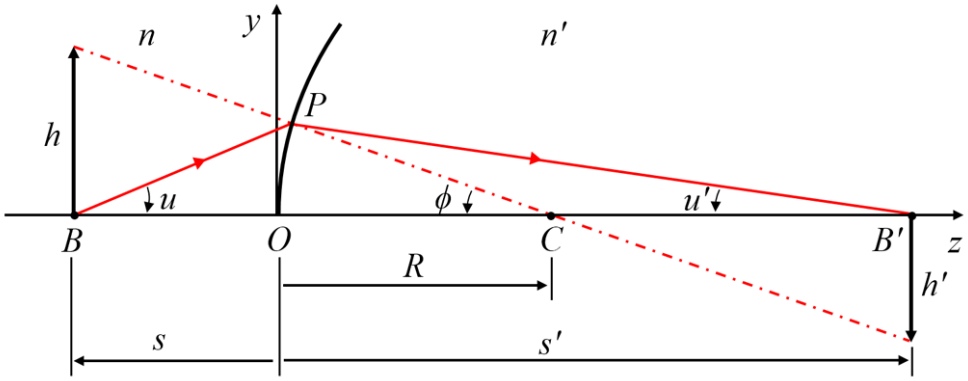

Figure 2.2: The layout of lateral and angular magnifications.

The figure and paraxial approximation derives

$$h = (R - s)\tan\phi, \qquad h' = (R - s')\tan\phi \tag{2.2.1}$$

$$h(s' - R) = h'(s - R) \tag{2.2.2}$$

Lateral magnification (m) is defined as the ratio of image height to object height.

$$m \equiv \frac{h'}{h} = \frac{s' - R}{s - R}. \tag{2.2.3}$$

Figure 2.2 illustrates the inverted image, $h' < 0$. Thus, lateral magnification is positive for the erect image and negative for the inverted image.

Angular magnification (M) is the ratio of $\tan u'$ to $\tan u$, which approximating to

$$M \equiv \frac{\tan u'}{\tan u} = \frac{s}{s'}. \tag{2.2.4}$$

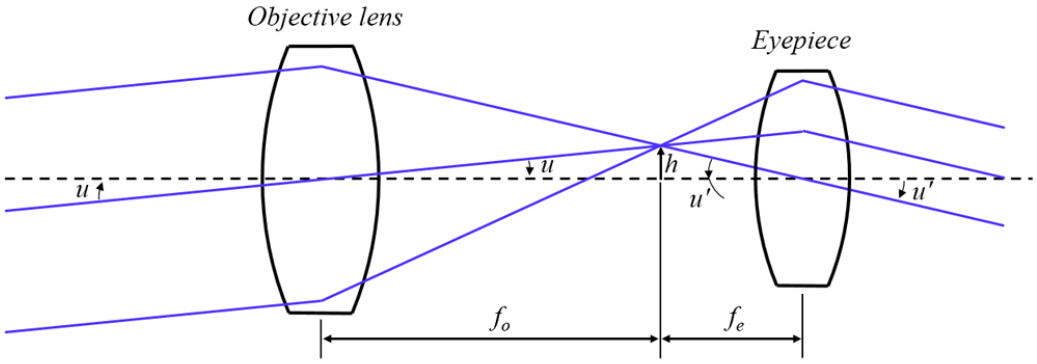

Figure 2.3: The layout of the telescope.

Magnification of telescopes (M_{tel}) with an eyepiece is derived from Equation 2.2.4. Figure 2.3 illustrates the layout of the telescope,

$$M_{tel} \equiv \frac{\tan u'}{\tan u} = \frac{h/f_e}{h/f_o} = \frac{f_o}{f_e}. \tag{2.2.5}$$

where, f_o is the focal length of the objective lens and f_e is the focal length of the eyepiece.

2.2.2 Newtonian's lens equation

The focal length of the optical system can be expressed with the distance from F (or F') to B (or B') instead of using s and s' (Figure 2.4).

$$\frac{h}{x} = \frac{h'}{f}, \qquad \frac{h'}{x'} = \frac{h}{f} \tag{2.2.6}$$

$$\frac{f}{x} = \frac{x'}{f}, \tag{2.2.7}$$

and the equation is summarized to

$$f^2 = xx' \tag{2.2.8}$$

that we called the Newtonian's lens equation.

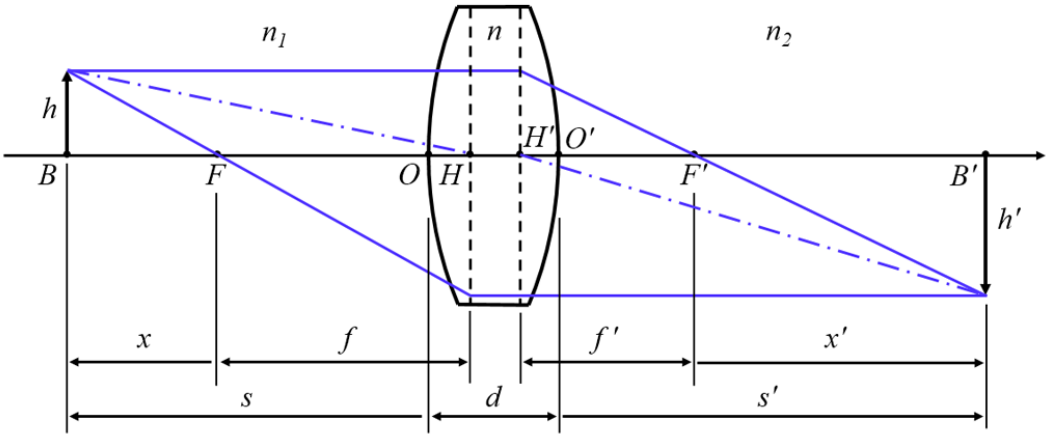

Figure 2.4: Thick lens layout. Black dashed lines represent the front and rear principal planes.

2.2.3 The lens-maker's formula

Assuming that the thin lens, which has negligible lens thickness, is surrounding by the air that has the refractive index, n_1 and n_2, of 1 (see Figure 2.4). The lens-maker's formula is derived starting from the Equation 2.1.11. For the front surface,

$$\frac{1}{s_1} - \frac{n}{s_1'} = \frac{1-n}{R_1} \tag{2.2.9}$$

where, s_1 and s_1' are object and image distance of the front surface, and R_1 is a radius curvature of the front surface. For the rear surface,

$$\frac{n}{s_2} - \frac{1}{s_2'} = \frac{n-1}{R_2} \tag{2.2.10}$$

where, s_2 and s_2' are object and image distance of the rear surface, and R_2 is a radius curvature of the rear surface. Since it is the thin lens, image distance of the front surface

is equal to object distance of the rear surface, $s_2 = s_1'$. Equation 2.2.9 and 2.2.10 give

$$\frac{1}{s_2'} - \frac{1}{s_1} = \frac{n-1}{R_1} + \frac{1-n}{R_2} \tag{2.2.11}$$

$$\frac{1}{s_2'} - \frac{1}{s_1} = (n-1)\Big(\frac{1}{R_1} - \frac{1}{R_2}\Big). \tag{2.2.12}$$

s_2' and s_1 are also expressed in s' and s, respectively. Image distance becomes the focal length (f) when the object distance is infinite. We therefore finally derive the lens-maker's formula for the thin lens to

$$\frac{1}{f} = (n-1)\Big(\frac{1}{R_1} - \frac{1}{R_2}\Big). \tag{2.2.13}$$

This equation transforms into

$$\frac{1}{f} = (n-1)\Big(\frac{1}{R_1} - \frac{1}{R_2} + \frac{(n-1)d}{nR_1R_2}\Big) \tag{2.2.14}$$

for the thick lens with lens thickness of d.

2.2.4 Numerical Aperture (NA) and F/#

The light-gathering power (LGP) of the optical system is decided by the entrance pupil diameter (D)

$$LGP = \frac{\pi D^2}{4}. \tag{2.2.15}$$

On the other hand, the image brightness is related to a cone angle of the light on the image plane. The light-gathering capability of the lens is generally described in Numerical aperture (NA) that defined by the refractive index of the medium (n) and the half-angle of the cone of the light.

$$NA = n \sin \alpha. \tag{2.2.16}$$

where, α is the half-angle of the cone of the light, which is generally the angle of the marginal ray of the system. For the astronomical telescopes, the numerical aperture is not

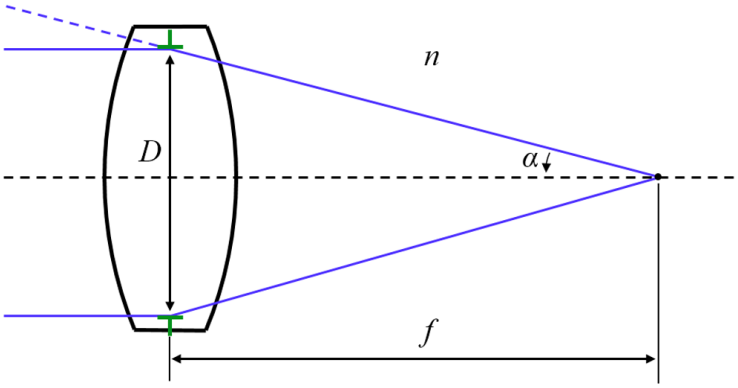

Figure 2.5: Simple lens layout. Green symbols indicate the location of the stop.

commonly used. Instead, F/# represents the angular aperture of the incident light by using the focal length (f) and the entrance pupil diameter (D),

$$\texttt{F/\#} = \frac{f}{D}. \tag{2.2.17}$$

A low F/# system has a relatively large entrance pupil diameter to its focal length that can gather more light at the image plane. Therefore, we call a bright (or fast) system for the low F/# optical systems and a dark (or slow) system for the high F/# optical systems.

These two equations (Equation 2.2.16 and 2.2.17) are exchangeable that we can find geometrical relationships between them from the simple lens layout (Figure 2.5).

$$\alpha = \arctan\left(\frac{D}{2f}\right) \tag{2.2.18}$$

combining with Equation 2.2.16,

$$NA = n\sin\left(\arctan\left(\frac{D}{2f}\right)\right) \tag{2.2.19}$$

$$NA = n\sin\left(\arctan\left(\frac{1}{2\texttt{F/\#}}\right)\right). \tag{2.2.20}$$

When the optical system is surrounding by air ($n = 1$), Equation 2.2.20 in paraxial approximation becomes

$$NA \approx \frac{1}{2\texttt{F/\#}} \qquad or \qquad \texttt{F/\#} \approx \frac{1}{2NA}. \tag{2.2.21}$$

2.3 Stops and pupils

In an optical system, there are stops and pupils which are useful to know to understand optical design and their parameters. The entrance pupil is the image of the aperture stop from the object side. Its location is decided by the point that extension of the chief ray from the object side meeting to the optical axis, and its size is limited to extension lines of the marginal rays from the object side (Figure 2.6).

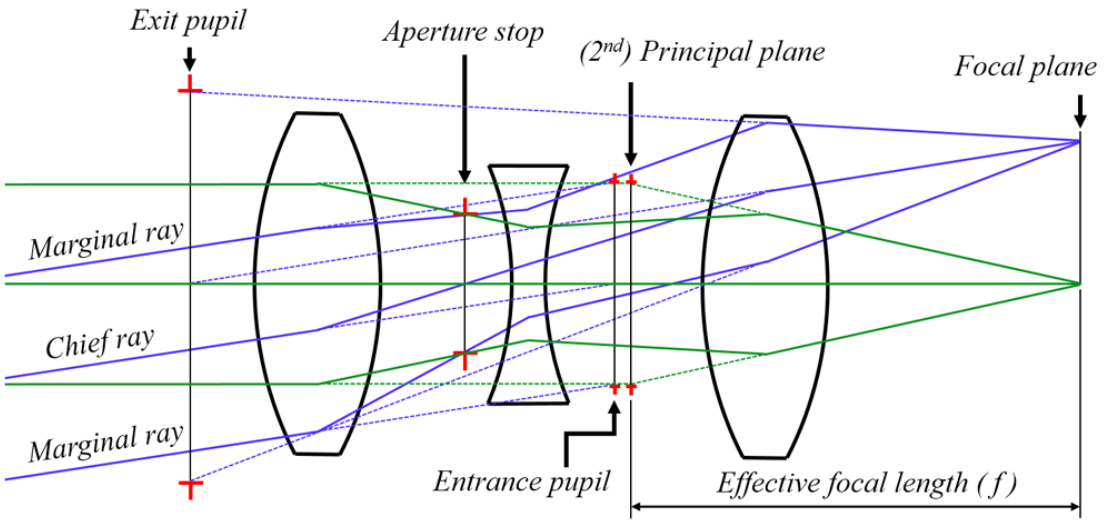

Figure 2.6: An aperture stop and entrance/exit pupil locations and their sizes. The effective focal length of the system is indicated as a distance from the second principal plane to the focal plane.

The location and size of the exit pupil are also decided by the same way of those of the entrance pupil but all rays are extended from the image side. Entrance pupil diameter (D or EPD) is commonly known as an aperture size for telescopes, so it relates to the light-gathering power as we discussed in Section 2.2.4. It is also an important parameter that decides an image resolution. We will discuss this in Section 3.1.

The exit pupil is a key parameter when we relay optical systems. For example, the exit pupil is used for the combination of a telescope and an eyepiece which is designed for

observing celestial bodies with human eyes. To do that, the exit pupil of the eyepiece that mounted on the telescope is located at the entrance pupil of the eyes (Figure 2.7).

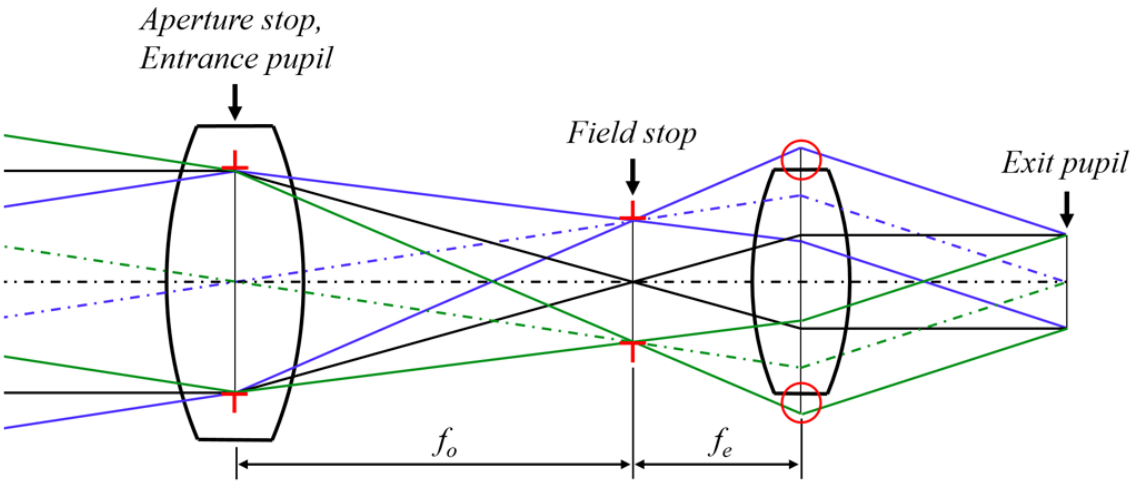

Figure 2.7: The illustration for stop and pupil locations. Solid and dot-dashed rays represent marginal and chief rays, respectively. Red circles indicate the light path where vignetting effect occurs.

The exit pupil can be utilized to instrument calibrations. For instance, Gregorian telescopes have the exit pupil between primary and secondary mirrors, so instrument calibration sources such as flat fielding targets or spectral lamps can be located on the exit pupil for telescope calibrations. The exit pupil in Cassegrain telescopes is located behind the secondary mirror, so it is impossible to implement the calibration in the same way of the method for Gregorian telescopes (Figure 2.8).

The aperture stop is located at the point where chief rays meet to the optical axis. It limits ray bundles of the incident ray, so it is commonly used with a physical stop in camera lenses for stopping down the incident light and for reducing aberrations. For most of two mirror and prime focus systems set the primary mirror as the aperture stop to maximize the entrance pupil diameter within the limited size of the mirror.

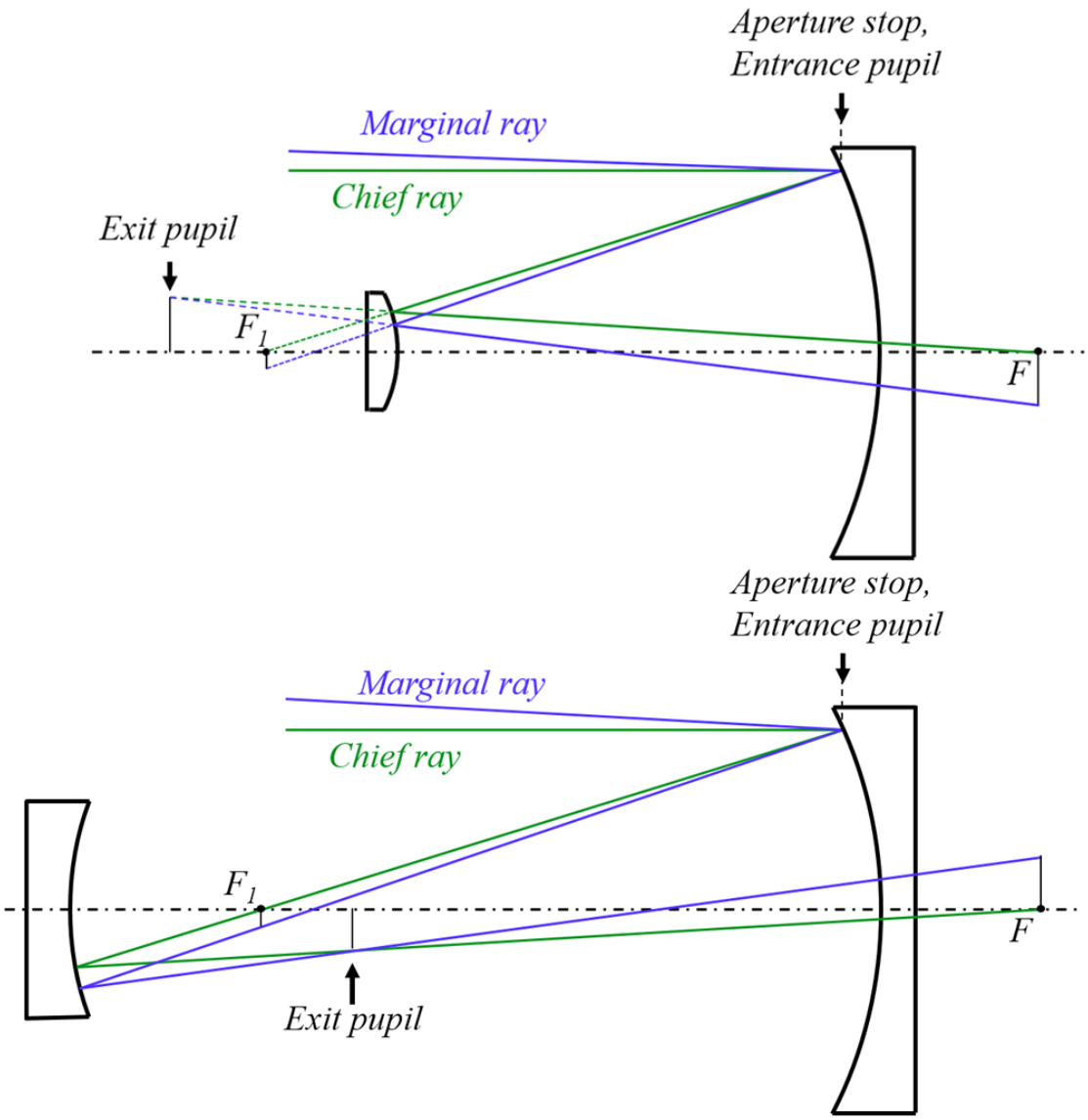

Figure 2.8: Optical layout of Cassegrain (top) and Gregorian (bottom) telescopes.

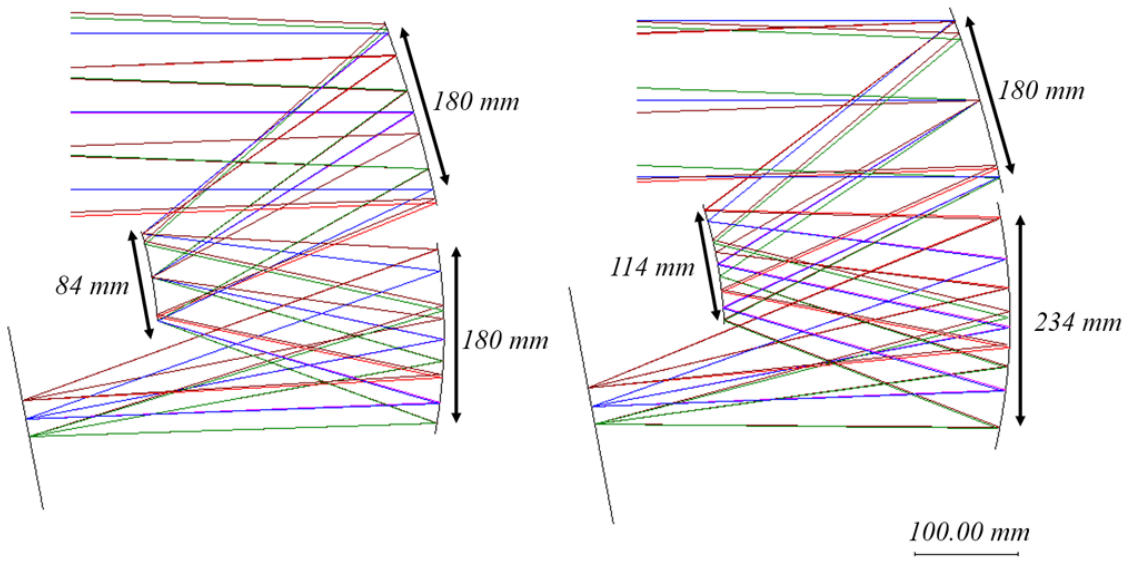

Figure 2.9: Three mirror off-axis systems with the same specifications and the aperture stop located at the secondary mirror (left) and at the primary mirror (right).

The off-axis three mirror systems put the aperture stop at the secondary mirror instead of setting it at the primary mirror. It is the reason for minimization of optical component sizes. Figure 2.9 illustrates two off-axis three mirror designs with the same specifications but the left one has an aperture stop at the secondary mirror, and the other one has an aperture stop at the primary mirror. In this case, the tertiary mirrors have a 54 mm in size difference between them which extremely more challenging in fabrication to the larger one.

The field stop limits angular acceptance of the chief ray, in other words limiting field of view (see Figure 2.7). Therefore it is useful for stray light suppression or for the cold stop. The cold stop is a common window for infrared cameras keeping the temperature of the detector.

2.4 Plate scale and field of view

The plate scale is extensively used especially by astronomers to describe the relation between an incident angle of the ray (u) and the image height (h) (see, Figure 2.10):

$$Plate\ scale\ [1/mm] = \frac{1}{f} \tag{2.4.1}$$

$$[''/mm] = \frac{180}{\pi} \times 3600 \times \frac{1}{f} = \frac{206265}{f}. \tag{2.4.2}$$

From the plate scale we simply calculate the field of view of the system ($2u$):

$$2u\ [^{'}] = \frac{206265}{f} \times \frac{1}{60} \times 2h\ [mm]. \tag{2.4.3}$$

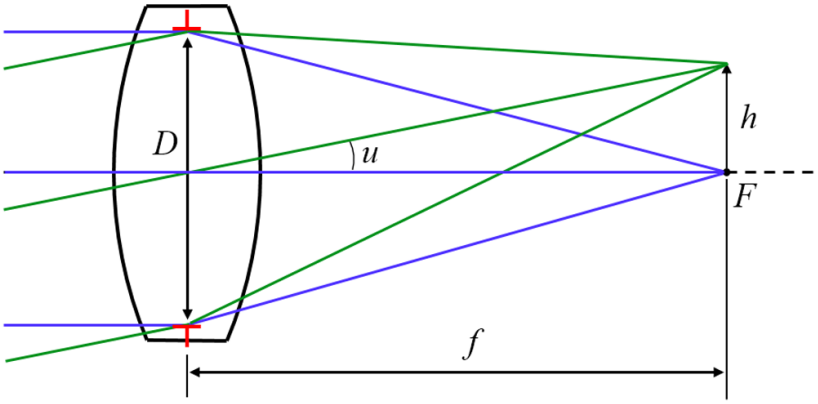

Figure 2.10: Optical layout of the simple lens design.

The plate scale is also useful in the optical design step to avoid undersampling or oversampling of the system by comparing h with the pixel size of the sensor.

Chapter 3

Introduction to Optical Aberrations

Optical aberration describes a phenomenon of the light from the point source spreading out to a certain size or patterns after the optical system rather than focusing at the point. Aberration does not exist in paraxial optics, so it is also defined as the deviation of the performance from the expectation of paraxial approximations.

Aberration is divided into monochromatic aberration and chromatic aberration. Chromatic aberration is caused by dispersion from lens material. Monochromatic aberration comes from geometrical shapes of lenses or mirrors, e.g., spherical aberration, coma aberration, astigmatism, field curvature, and distortion. These five monochromatic aberrations are known as The Five Seidel Aberrations named for Ludwig von Seidel. Especially, spherical aberration, coma aberration, astigmatism, and field curvature directly degrade the image resolution.

3.1 Airy disk

Point source images never become an ideal point even with a perfect optical system, because the light after the optical system is limited by the diffraction of the light. The airy disk (or airy pattern) is the pattern of the best-focused spot with the perfect optical system. Since the airy disk is the result of the diffraction, there is no airy disk considered in geometrical

optics. The angle to the first minimum (intensity) of the airy disk is

$$\sin\theta \approx \frac{1.22\lambda}{D} \tag{3.1.1}$$

where, λ is the wavelength, and D is the aperture diameter. From this equation, the airy disk diameter is calculated with the equation below

$$D_{Airy} = \frac{2.44\lambda f}{D} \tag{3.1.2}$$

where, f is the focal length of the optical system. So shorter focal length and larger aperture diameter telescopes focus the smaller spot image.

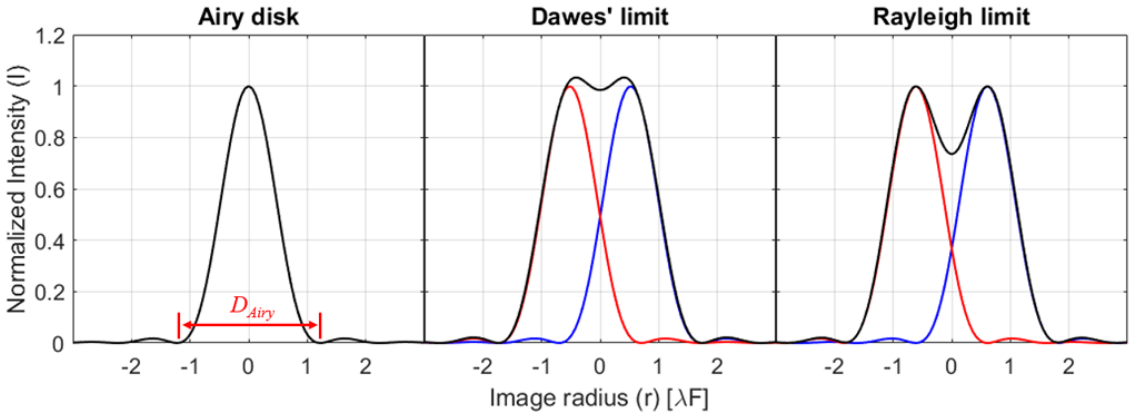

Figure 3.1: Airy disk patterns and image resolution limits, Dawes' limit (middle) and Rayleigh limit (right).

Figure 3.1 illustrates airy disk patterns with image resolution limits. Note that the unit of the image radius (r) is λF and F is `F/#` in Equation 2.2.17. The equation of normalized intensity (I) of the airy disk pattern is given by

$$I(r) = \left(1 + \sum_{i=1}^{\infty}(-1)^i \frac{((r \pm 0.5s)\pi/2)^{2i}}{i!(i+1)!}\right)^2. \tag{3.1.3}$$

The maximum separation (s) for the single airy pattern is 0. The fraction of total energy contained within the first, second, and third dark rings for the single airy pattern are 83.8%, 91.08%, and 93.88%, respectively (Born & Wolf, 1999; Mahajan, 2011).

Dawes' limit is the empirical resolution limit with the maximum separation of $s = 1.04$ that is considered as the maximum resolution of the telescope. Rayleigh limit is a formal resolution criterion with the maximum separation of $s = 1.22$ (Vladimir Sacek, 2019). Each limit represents image contrast (intensity difference of the maximum and dip between two points) of 5% and 26.3% for Dawes' limit and Rayleigh limit, respectively (Michalet & Weiss, 2006).

3.2 Zernike polynomial

Zernike polynomial is extremely useful to express wavefront or surface figure of the optics. It is firstly derived by Fritz Zernike in 1934. Each term of the polynomial expresses the type of the optical aberration, which is easily comparable to optical test results (see aberration patterns in Figure 3.2). Zernike polynomials are defined in radial coordinates, radial distance R and azimuth θ. Azimuth θ is positive to counter-clockwise from the +x-axis (Table 3.1).

3.3 Defocus

Defocus is an aberration in which an image plane located out of focus. It is removable by precisely refocusing the imaging system. The degree of blurring by the focal position is accounted to the depth of focus. Sharpness and contrast of the image for defocus are more sensitive for a small `F/#` optics (small depth of focus) than a large `F/#` optics (large depth of focus) as illustrated in Figure 3.3.

Table 3.1: Standard Zernike polynomial terms

Term	Standard Zernike Polynomial	Aberration type
1 (Z_0^0)	1	Piston (constant)
2 (Z_1^{-1})	$Rcos\theta$	Distortion - Tilt (x-axis)
3 (Z_1^1)	$Rsin\theta$	Distortion - Tilt (y-axis)
4 (Z_2^{-2})	$R^2cos2\theta$	Astigmatism, Primary (axis at 0° or 90°)
5 (Z_2^0)	$2R^2 - 1$	Defocus - Field curvature
6 (Z_2^2)	$R^2sin2\theta$	Astigmatism, Primary (axis at ±45°)
7 (Z_3^{-3})	$R^3cos3\theta$	Trefoil, Primary (x-axis)
8 (Z_3^{-1})	$(3R^3 - 2R)cos\theta$	Coma, Primary (x-axis)
9 (Z_3^1)	$(3R^3 - 2R)sin\theta$	Coma, Primary (y-axis)
10 (Z_3^3)	$R^3sin3\theta$	Trefoil, Primary (y-axis)
11 (Z_4^{-4})	$R^4cos4\theta$	Tetrafoil, Primary (x-axis)
12 (Z_4^{-2})	$(4R^4 - 3R^2)cos2\theta$	Astigmatism, Secondary (axis at 0° or 90°)
13 (Z_4^{-0})	$6R^4 - 6R^2 + 1$	Spherical Aberration, Primary
14 (Z_4^2)	$(4R^4 - 3R^2)sin2\theta$	Astigmatism, Secondary (axis at ±45°)
15 (Z_4^4)	$R^4sin4\theta$	Tetrafoil, Primary (y-axis)
16 (Z_5^{-5})	$R^5cos5\theta$	Pentafoil, Primary (x-axis)
17 (Z_5^{-3})	$(5R^5 - 4R^3)cos3\theta$	Trefoil, Secondary (x-axis)
18 (Z_5^{-1})	$(10R^5 - 12R^3 + 3R)cos\theta$	Coma, Secondary (x-axis)
19 (Z_5^1)	$(10R^5 - 12R^3 + 3R)sin\theta$	Coma, Secondary (y-axis)
20 (Z_5^3)	$(5R^5 - 4R^3)sin3\theta$	Trefoil, Secondary (y-axis)
21 (Z_5^5)	$R^5sin5\theta$	Pentafoil, Primary (y-axis)
⋮	⋮	⋮

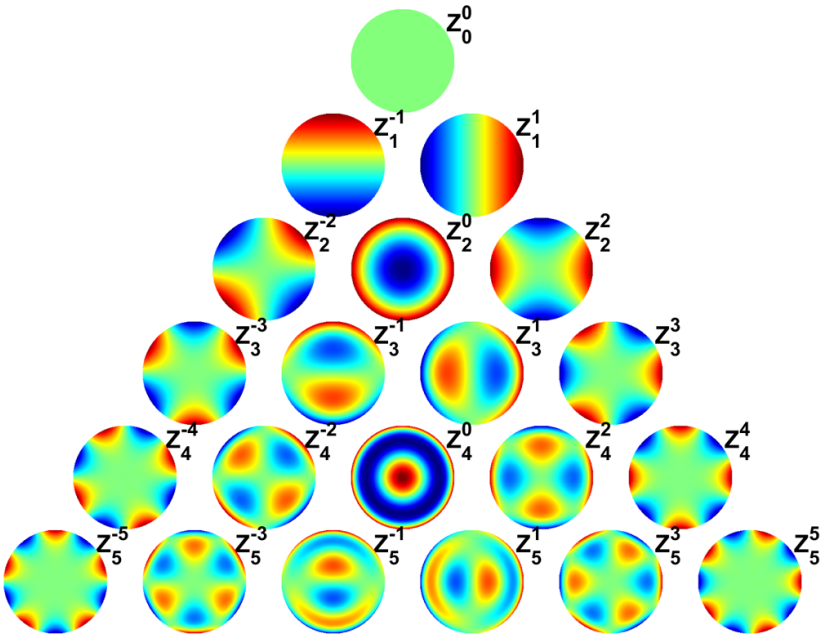

Figure 3.2: The first 21 Zernike polynomials, ordered by radial (R, vertical) and azimuth (θ, horizontal) degree.

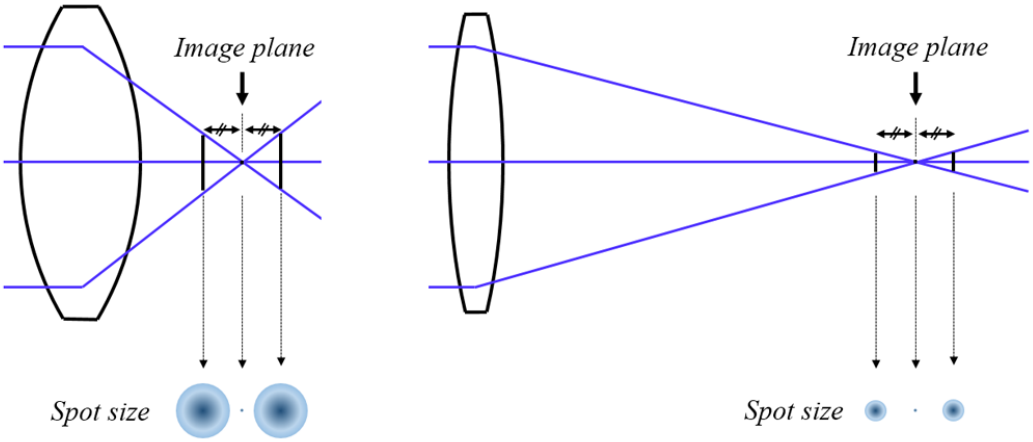

Figure 3.3: Depth of focus for a small (left) and large (right) `F/#` optics.

3.4 The Seidel Aberrations

3.4.1 Spherical aberration

The incident light close to the optical axis (chief ray) less refract or reflect than the light close to the edge of the optics (marginal ray) resulting in the focus position is closer for the marginal ray than the chief ray (Figure 3.4). This deviation degrades image quality. It happens when the light passing through a spherical surface of lenses or mirrors, so it is called spherical aberration. Combinations of spherical convex and concave surfaces reduce the spherical aberration, or it is also eliminated by using aspheric lenses or mirrors.

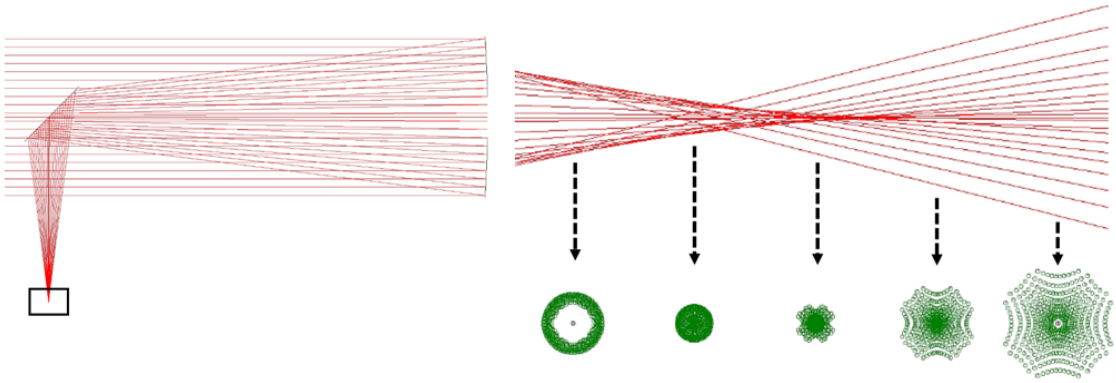

Figure 3.4: Spherical aberration in the Newtonian telescope with the spherical primary mirror. The Black square area is zoomed on the right panel.

Optimization of spherical aberration generally relies on the ray-tracing method. However, the aberration is also analytically minimized for simple lenses (Wikipedia, 2020).

$$\frac{R_1 + R_2}{R_1 - R_2} = \frac{2(n^2 - 1)}{n + 2}\left(\frac{s + s'}{s - s'}\right) \tag{3.4.1}$$

where, s is object distance, s' is image distance, n is the refractive index of the lens, and R_1 and R_2 are the radius of curvature of front and back surfaces of the lens.

3.4.2 Coma

Coma is an off-axis aberration that results in distorted point sources thus appearing like a comet with a tail (Figure 3.5). Coma correctors can reduce the aberration by using a combination of lenses like a plano-convex and a plano-concave lens (also called as spaced doublet lens). A Ritchey-Chrétien telescope is one of a two mirror telescope that adapts two hyperbolic mirrors designed for eliminating coma aberration.

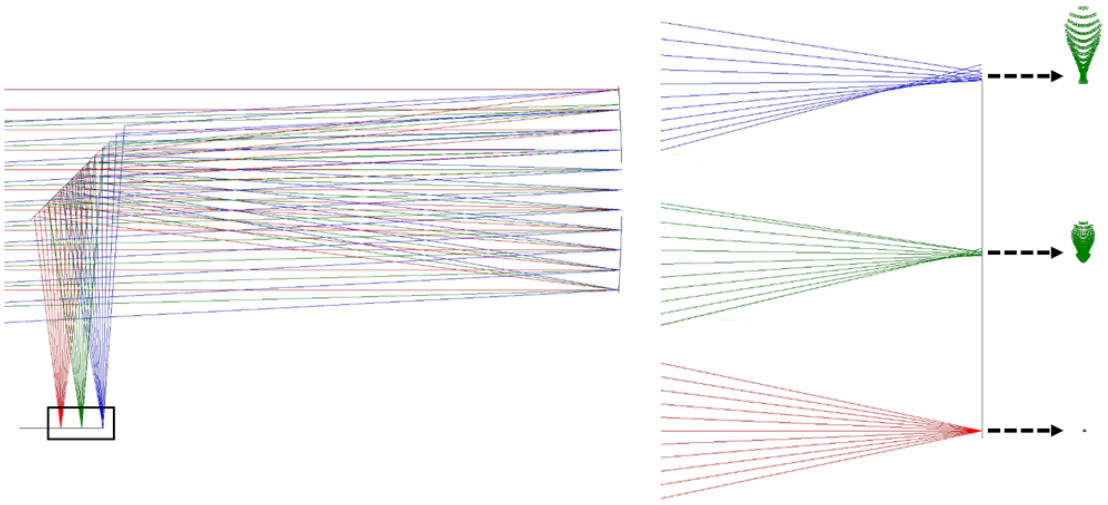

Figure 3.5: Coma in the Newtonian telescope. The Black square area is zoomed on the right panel.

3.4.3 Astigmatism

Astigmatism is an off-axis aberration that rays in a sagittal image plane and a tangential image plane have different focuses (Figure 3.6). The most common astigmatism is third-order astigmatism, which exists when the object away from the optical axis. It is the off-axis aberration but also very common for on-axis images when the optical system is misaligned.

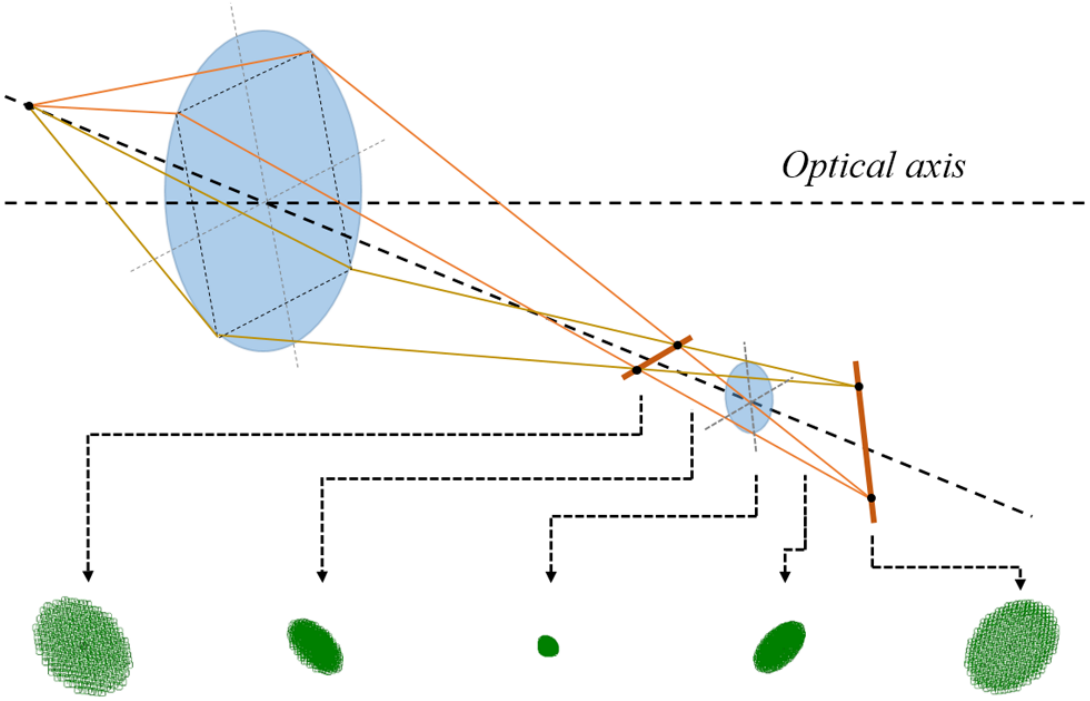

Figure 3.6: Astigmatism diagram and spot shapes at each focal position.

3.4.4 Field curvature

Most optical lenses or mirrors are curved for focusing the incident light, so these optical elements project the image in the curved surface rather than the flat image surface. This aberration is called field curvature, also known as Petzval field curvature. Since commercial digital sensors (CCD or CMOS) are flat, the image with field curvature is defocused at the off-axis fields while well-focused at the image center (see, the right panel in Figure 3.7).

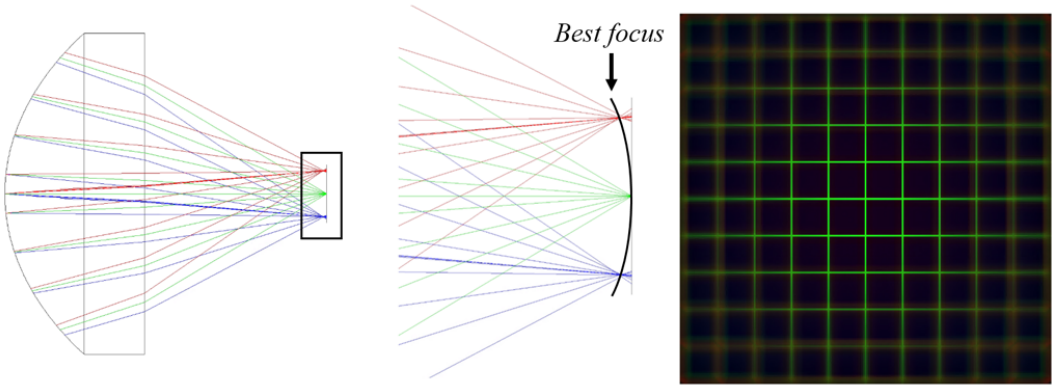

Figure 3.7: Field curvature in the simple lens. The Black square area is zoomed on the middle panel. Image simulation indicates the best focus at the center but defocused at the off-axis fields (right).

3.4.5 Distortion

Distortion geometrically deforms the image occurring dislocation of the off-axis image from the expected position. Comparing to other monochromatic aberrations, distortion does not degrade image quality. In most cases, we can calculate or measure distortion from the optical system to correct the aberration. There are two patterns of the most commonly encountered distortions, barrel (or positive) and pincushion (or negative) distortion (Figure 3.8).

Distortion is defined with the relation of predicted distance (PD) and actual distance

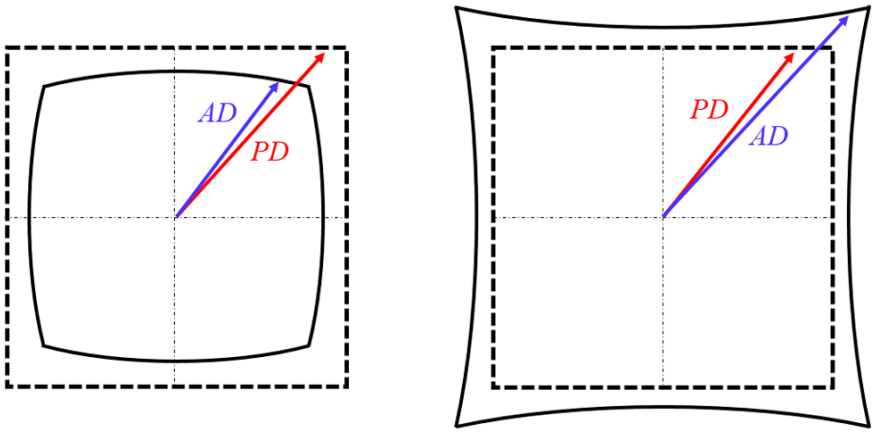

Figure 3.8: Barrel (left) and pincushion (right) distortion.

(AD) (Edmund Optics, 2011):

$$Distortion\ (\%) = \left(\frac{AD - PD}{PD}\right) \times 100\%. \tag{3.4.2}$$

3.5 Chromatic aberration

Chromatic aberration is a wavelength-dependent optical aberration that the multi-color light after a lens focuses at the different position by wavelength. Because the refractive index is the function of wavelength, short wavelength light focuses closer than longer wavelength light. For this reason, chromatic aberration only exists in a lens system. Achromatic (doublet) or apochromatic (triplet) lens corrects chromatic aberration by using combinations of flint (high dispersion) and crown (low dispersion) lenses (Figure 3.9).

3.6 Linear astigmatism

The classical off-axis reflective design alleviates wavelength limitations and avoids the obscuration problem, but it still faces limitations for wide field of view observations due to linear astigmatism. Linear astigmatism is a dominant aberration of classical off-axis

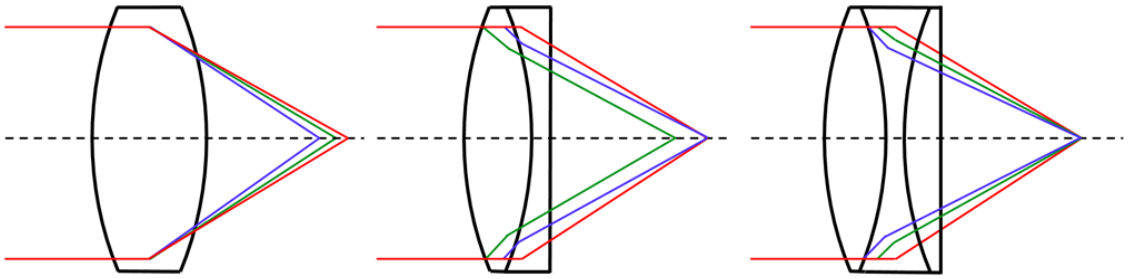

Figure 3.9: Chromatic aberration with the single lens (left), the achromatic lens (middle), and the apochromatic lens (right).

telescopes, and it significantly degrades image quality, especially for wide field of view systems (Chang, 2013, 2016).

For the conventional off-axis systems, tangential and sagittal planes are tilted, and it causes an astigmatic image. Figure 3.10 illustrates tangential and sagittal image planes from the single off-axis mirror. Each plane is tilted by i degree from the nominal image plane (dotted line).

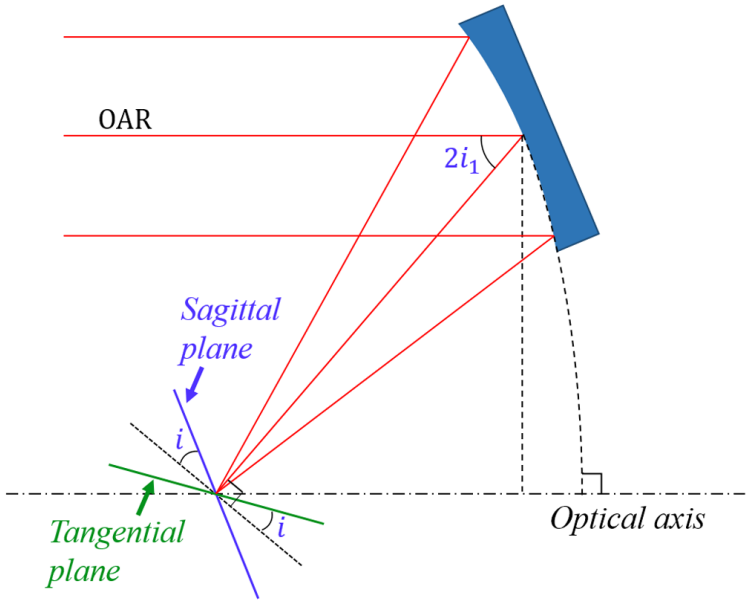

Figure 3.10: Tangential and sagittal planes from a single off-axis mirror (Chang, 2015).

The Seidel aberrations, which introduced in Section 3.4, are third order aberrations, and linear astigmatism is a second order aberration that is more critical to image quality (Chang & Aluizio Prata, 2005). Figure 3.11 shows spot diagrams of the on-axis and common off-axis classical Cassegrain telescopes. The on-axis classical Cassegrain has dominant coma for off-axis fields, but linear astigmatism is much more dominant for the common off-axis telescope.

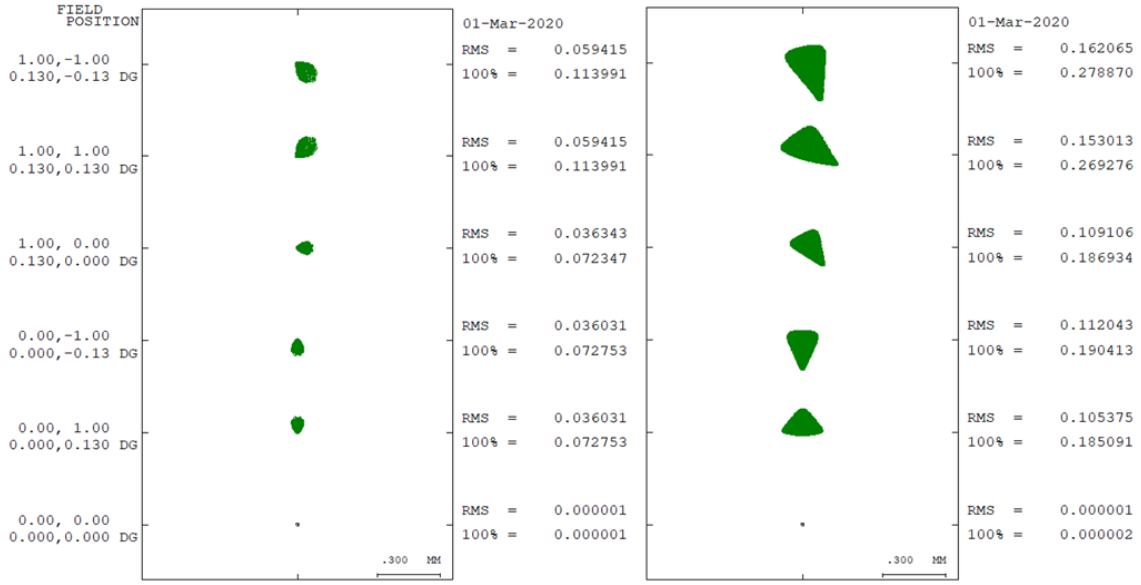

Figure 3.11: Spot diagrams of an on-axis classical Cassegrain telescope (left) and a common off-axis classical Cassegrain telescope (right). Dominant linear astigmatism is clearly seen in the common off-axis system.

Linear astigmatism can reduce by using correcting lenses, but also it can be eliminated by confocal off-axis design. We will introduce linear-astigmatism-free systems in Section 4.3.

Chapter 4

Reflecting Telescopes

Reflecting telescopes are the most common telescope optical design, because optical mirrors are relatively easy to fabricate and are light-weighted than optical lenses. For this reason, most of the large telescopes (miter scale) are the reflecting telescope. On-axis reflective optical system, however, is limited to narrow field of view observations since the wider the field of view observations, the larger the secondary mirrors become, resulting in serious obscuration. The secondary mirrors and their supports also cause diffraction and scattering of the incident light. Off-axis telescopes are an alternative approach to avoid these problems. In this section, we will briefly review the conventional on-axis reflecting telescopes and will introduce off-axis telescopes.

4.1 Conic section

A conic section is a curve coming from the intersection of a cone with a plane. Conic surfaces, also called aspheric surfaces, are widely adapted to optical surfaces to reduce or eliminate aberrations. The aspheric surface has the form of the conic section with the surface sag defined as

Contents of this chapter are published in the publication [3] and [5].

$$z = \frac{cr^2}{1 + \sqrt{1 - (1+k)c^2r^2}} \tag{4.1.1}$$

where, k is conic constant, c is surface curvature, and r is radial coordinate of the surface from the vertex.

There are three types of conic surfaces, parabola, hyperbola, and ellipse that are decided by the conic constant (Table 4.1).

Table 4.1: Conic surface type

Surface type	Conic constant
Sphere	0
Hyperboloid	k < -1
Paraboliod	k = -1
Prolate ellipsoid	-1 < k < 0
Oblate ellipsoid	k > 0

Two mirror telescopes combine two aspheric or spheric surfaces to optimize aberrations. Cassegrain, Gregorian, Maksutov, Ritchey-Chrétien, Schmidt, Schmidt-Cassegrain, Dall-Kirkham telescopes are popular two mirror telescopes. Figure 4.1 illustrates optical configurations of Newtonian, Cassegrain, and Gregorian telescopes. In each case, incident rays are reflected from the paraboloidal primary mirror and the secondary mirror sequentially, so that rays converge to a single focal point as depicted in the figure. The Newtonian, Cassegrain, and Gregorian systems use flat, convex hyperboloidal, and concave ellipsoidal secondary mirrors, respectively.

Table 4.2 lists two mirror telescopes, their surface types, and characteristics. Newtonian and Schmidt telescopes are technically single mirror telescopes but we include them in this table for comparison. Ritchey-Chrétien telescopes are the most popular optical type for meter-scale large telescopes. Schmidt-Cassegrain telescopes are more popular for small size telescopes because the correcting plate becomes hard to fabricate and heavy in large.

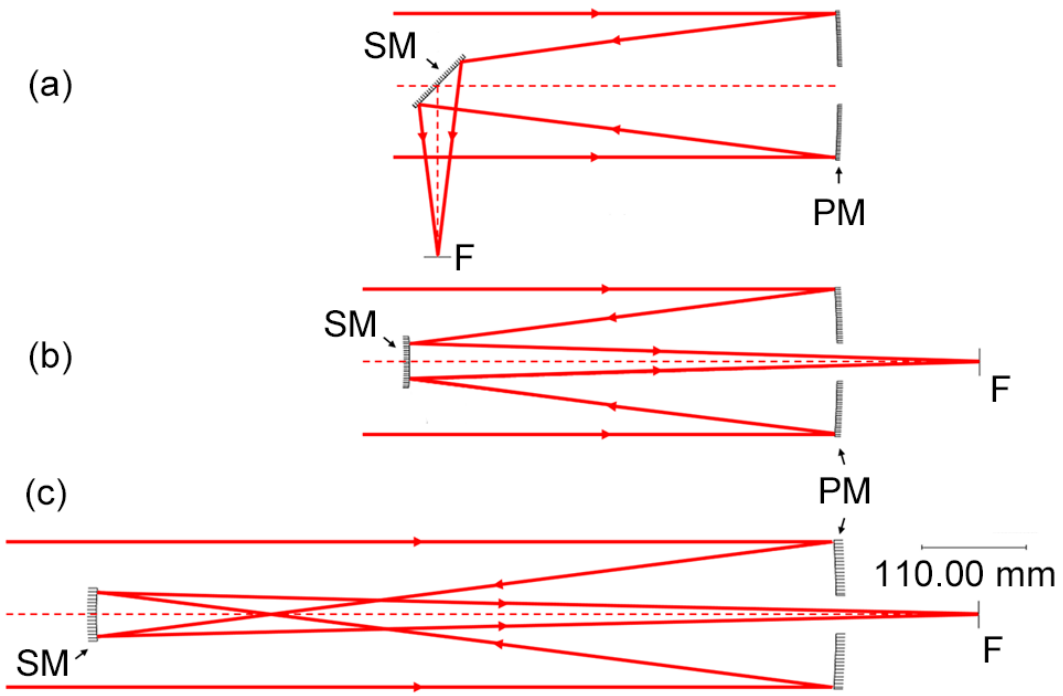

Figure 4.1: Optical layout of (a) Newtonian, (b) Cassegrain, and (c) Gregorian telescope for the TRT Kit. (PM: primary mirror, SM: secondary mirror, F: focal point).

Table 4.2: List of two mirror telescopes and their characteristics

Telescope type	Surface type	Characteristic
Newtonian	Pri.: Paraboloid, Sec.: flat	Simple, Easy alignments, Dominant Coma
Schmidt	Pri.: Spherical, Prime focus, Corrector plate	Small F/#, Large obscuration
Cassegrain	Pri.: Paraboloid, Sec.: Hyperbola	Large off-axis aberration
Gregorian	Pri.: Paraboloid, Sec.: Ellipsoidal	Erect image, Exit pupil BTW mirrors, Large F/#
Ritchey-Chrétien	Pri.: Hyperbola, Sec.: Hyperbola	Free Coma, Small F/#, Large telescopes
Maksutov-Cassegrain	Pri.: Spherical, Sec.: A.S., Meniscus lens	Free Coma and astigmatism, Large F/#
Schmidt-Cassegrain	Pri.: Spherical, Sec.: Hyperbola, Corrector plate	Compact, Easy to Fabricate, Small telescopes
Dall-Kirkham	Pri.: Ellipsoidal, Sec.: Spherical	Require corrector, Small off-axis aberration, Easy alignments

Pri.: Primary, Sec.: Secondary, A.S.: Aluminized spot on the meniscus lens

4.2 On-axis vs. Common off-axis vs. Confocal off-axis

Classical two mirror on-axis reflective telescopes are limited to narrow field of view observations due to the secondary mirror that located in front of the primary mirror, so off-axis optical systems become popular for telescopes and other optical systems since they avoid scattering, diffraction, and obscuration by the secondary mirror.

We have categorized off-axis telescopes into common and confocal off-axis systems. Primary and secondary mirrors in both on-axis and common off-axis systems share their optical axes but only off-axis sections of mirrors are used for the common off-axis system. Optical mirrors of the confocal off-axis system share their focuses instead of sharing their axes. Figure 4.2 illustrates optical layout of on-axis, common off-axis, and confocal off-axis systems. All three optical designs are based on the Cassegrain reflecting telescope. Optical axis ray (OAR) (Sasian, 1994) is indicated in a red solid line.

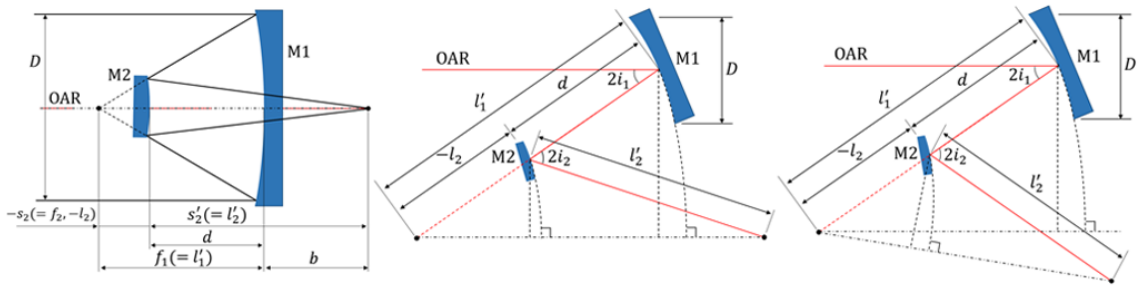

Figure 4.2: Optical layouts of on-axis (left), common off-axis (middle), and confocal off-axis (right).

Optical design methods for the on-axis, common off-axis, and confocal off-axis Cassegrain systems are methodologically summarized in Schroeder (2000) and Chang (2015). We set the tilt angle of the primary mirror (M1) to 15° for two off-axis systems to design unobscured off-axis telescopes. All the Cassegrain telescopes have the same entrance pupil diameter (EPD) of 1000 mm, and effective focal length (EFL) of 8000 mm. M1 is set to the aperture stop. Calculated optical design parameters are listed in Table 4.3. Field of

view is based on typical 36 mm × 36 mm detectors.

Table 4.3: Specifications of on-axis, common off-axis, and confocal off-axis two mirror systems.

Type	On-axis	Common off-axis	Confocal off-axis
Primary D	1000 mm		
System f	8000 mm		
Field of view	0.26° (H) × 0.26° (V)		
Pixel scale	0.31″/pixel (12 μm)		
A_{eff}[a]	0.705 m^2	0.785 m^2	0.785 m^2
f_1	2000 mm	1866.025 mm	1866.025 mm
K_1	-1	-1	-1
l_1'	2000 mm	2000 mm	2000 mm
i_1	0°	15°	15°
K_2	-2.777	-2.597	-2.577
l_2	-800 mm	-600 mm	-600 mm
l_2'	2400 mm	2400 mm	2400 mm
m_2	4	4	4
i_2	0°	-18.590°	-19.660°

[a] Effective light collecting area.

All systems have an ideal focus at the image center, but coma aberration exists on the other fields for the on-axis system. Optical performance of the common off-axis system dramatically degrades for the wide field angles because of linear astigmatism. The confocal off-axis system can eliminate linear astigmatism by satisfying the linear astigmatism-free condition, so optical performance of the system becomes identical to its of the on-axis system. The linear astigmatism-free conditions for off-axis systems will be introduced in Section 4.3.

Spot diagrams show that coma aberration is dominant for on-axis and confocal off-axis

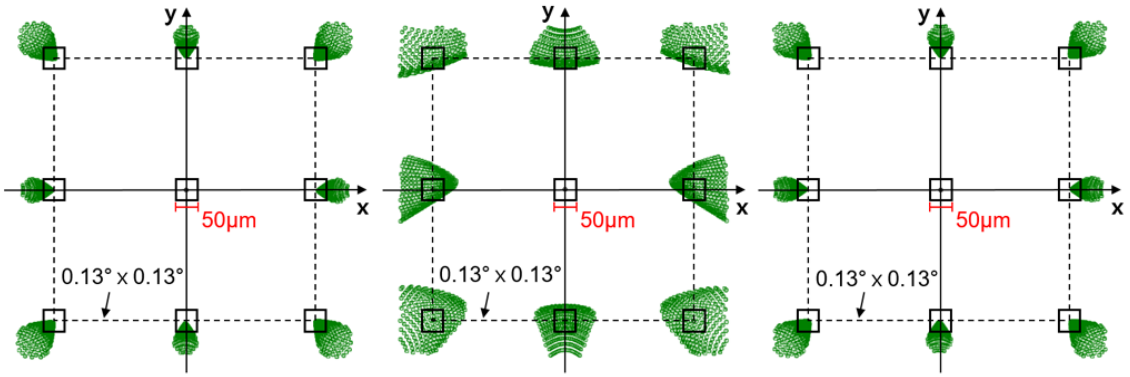

Figure 4.3: Spot diagrams of on-axis (left), common off-axis (middle), and confocal off-axis (right).

Cassegrain systems, while linear astigmatism critically degrades the performance of the common off-axis system (Figure 4.3).

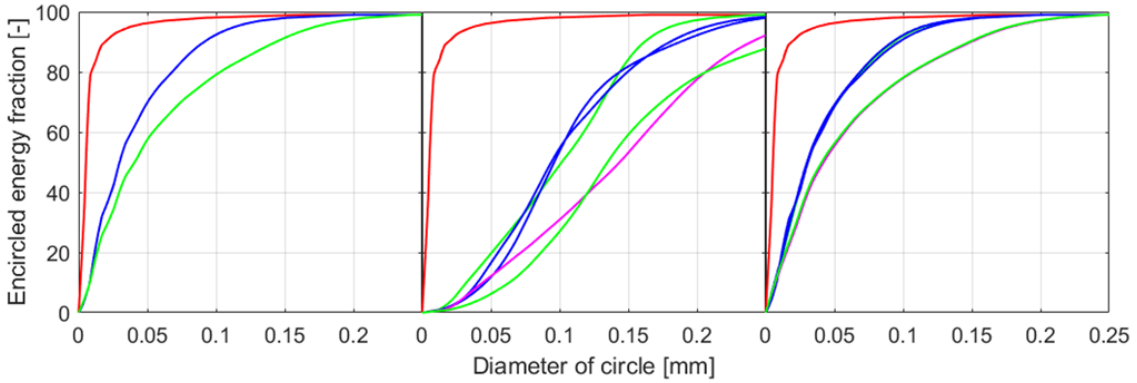

Figure 4.4: Encircled energy diameters over different field of views (colors) of on-axis (left), common off-axis (middle), and confocal off-axis (right).

Figure 4.4 represents encircled energy diameter (EED) of three systems. EEDs of on-axis and confocal off-axis systems have the same optical performance with <0.10 mm 80% EED for both systems. On the other hand, 80% EED of the common off-axis system is <0.20 mm, which is the twice spot size to other systems because of linear astigmatism.

4.3 Linear-astigmatism-free off-axis system

Linear-astigmatism-free confocal off-axis reflective system overcomes both the field of view and wavelength limits without the need for correcting lenses. Confocal off-axis design whose optical components share focuses instead of sharing axis can eliminate linear astigmatism by properly selecting mirror surface parameters and tilt angles (Chang et al., 2006).

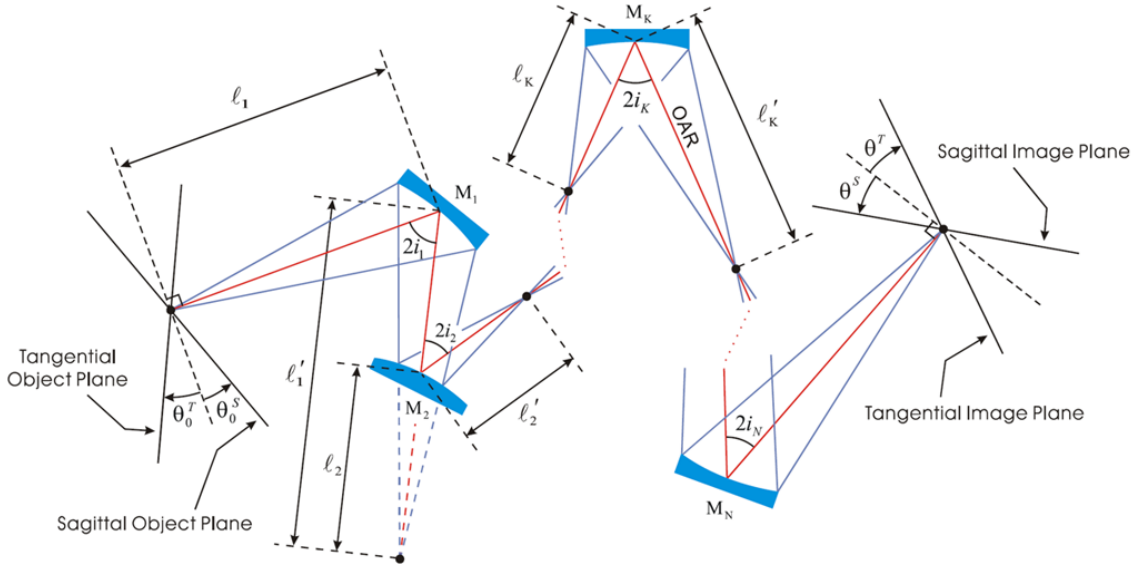

Figure 4.5: A confocal off-axis system design concept (from Chang (2015) Figure 4).

Chang (2015) derived the linear-astigmatism-free condition for N-conic mirror system (Figure 4.5) that is

$$\tan\theta_N^T - \tan\theta_N^S = \sum_{p=1}^{N-1}\left[(1+m_p)\tan i_p \prod_{q=p+1}^{N} m_q\right] + (1+m_N)\tan i_N \tag{4.3.1}$$

$$= \frac{1}{2}(\tan\theta_0^T - \tan\theta_0^S)\prod_{p=1}^{N} m_p \tag{4.3.2}$$

where, θ_N^T and θ_N^S are tilt angles of the tangential and the sagittal image planes, i_N is an incident angle of the light for the N-th mirror, and m_N is magnification that given by

$$m_N = \frac{l'_N}{l_N}. \tag{4.3.3}$$

Equation 4.3.1 can be solved to Equation 4.3.4 and Equation 4.3.5 for two mirror system and three mirror system, respectively.

$$(1 + m_1)m_2 \tan i_1 + (1 + m_2) \tan i_2 = 0 \tag{4.3.4}$$

$$(1 + m_1)m_2m_3 \tan i_1 + (1 + m_2)m_3 \tan i_2 + (1 + m_3) \tan i_3 = 0 \tag{4.3.5}$$

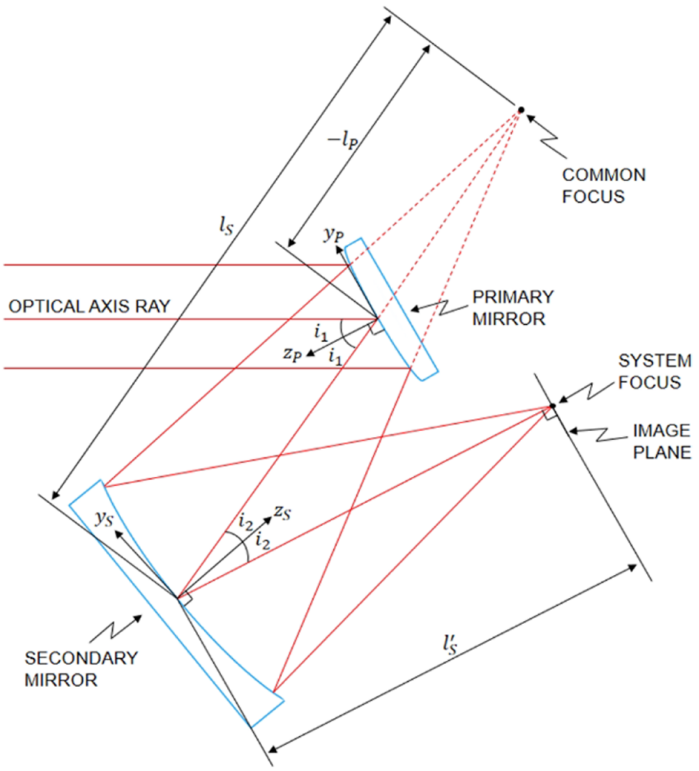

Figure 4.6: The optical layout of a Schwarzschild-Chang off-axis telescope.

Schwarzschild-Chang off-axis telescope is the first telescope designed for a linear-astigmatism-free two mirror system (Figure 4.6). Kim et al. (2010) verified the feasibility of linear-astigmatism-free three-mirror optical design. It is an inverse-Cassegrain type telescope,

which uses a parabolic convex primary mirror and an ellipsoidal concave secondary mirror, so the secondary mirror size is large by comparing to EPD of the system. An aperture stop is located at the secondary mirror surface. Since it is a confocal off-axis system, there is a common focus of the primary and secondary mirrors.

Three mirror system has a more compact size than that of two mirror system whose has the same first-order-optical specifications such as EPD and focal length. Linear Astigmatism Free - Three Mirror System (LAF-TMS) is a linear-astigmatism-free confocal off-axis three mirror telescope. Figure 4.7 illustrates the optical layout of LAF-TMS, where the optical path is indicated by red-solid lines. The mirror surface combination of the base confocal off-axis system is a parabolic concave primary mirror (M1), an ellipsoidal convex secondary mirror (M2), and an ellipsoidal concave tertiary mirror (M3). Thus, M1 shares its focus with M2. Two M2 focuses are shared with M1 and M3, respectively. One of the M3 focuses is shared with M2, and the other one is the system focus. The M1 & M2 common focus and the M2 & M3 common focus are labeled in Figure 4.7.

Mirror tilt angles and inter mirror distances, also called despace, are accurately calculated to satisfy the linear-astigmatism-free condition, as expressed in Equation 4.3.6 (Chang, 2013)

$$\frac{l_2'}{l_2}\frac{l_3'}{l_3}\tan i_1 + \left(1+\frac{l_2'}{l_2}\right)\frac{l_3'}{l_3}\tan i_2 + \left(1+\frac{l_3'}{l_3}\right)\tan i_3 = 0. \tag{4.3.6}$$

In equation (4.3.6), $i_{1,2,3}$ are tilt angles of each mirror, and $l_{2,3}$ and $l'_{2,3}$ are the front and the back focal lengths of each mirror, respectively, as denoted in Figure 4.7. This equation is the same as Equation 4.3.5 but only magnifications are converted to the distance between the front or rear focus of the mirror and the corresponding mirror surface.

The optical design of the MATS satellite is another application of linear-astigmatism-free confocal off-axis three mirror system. Figure 4.8 indicates spot diagrams of Schwarzschild-Chang off-axis telescope, the MATS satellite, and LAF-TMS representing that linear astigmatism is completely removed over all field of view for all three systems.

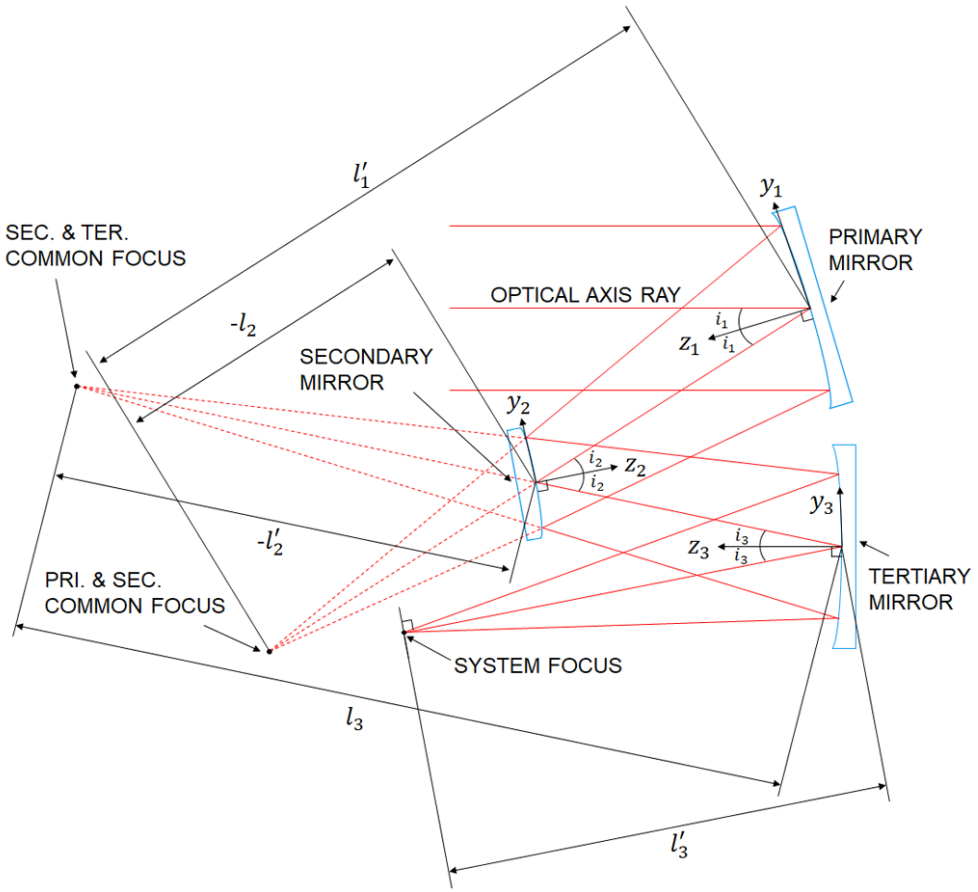

Figure 4.7: The optical layout of LAF-TMS. The optical path is drawn in red solid lines.

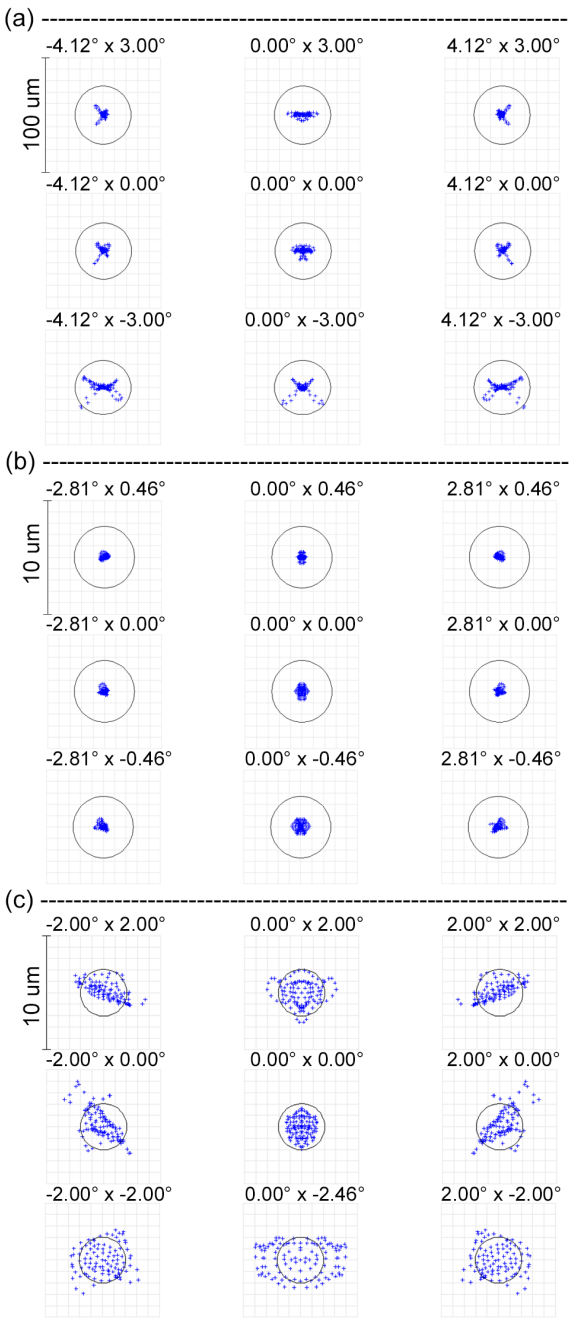

Figure 4.8: Spot diagrams of linear-astigmatism-free systems: (a) Schwarzschild-Chang off-axis telescope, (b) the MATS satellite, (c) LAF-TMS. Airy disks for 10 μm, 0.270 μm, and 0.500 μm wavelength are shown in black circles for (a), (b), and (c), respectively.

4.4 Freeform aluminum mirrors

Linear astigmatism is eliminated by applying confocal optical design, but high-order aberrations, generally, can be reduced by using additional correcting lenses or mirrors if we use spherical or aspherical surfaces to the main optics. High-order aberrations can be minimized by selecting freeform mirror surfaces. It becomes more popular to high performance optical systems thanks to technology development for freeform mirror fabrications in low surface errors. On the other hand, aluminum mirrors are conveniently mounted on the same aluminum-based optomechanics. Applying the same material to optics and optomechanics increases the thermal stability of the system.

Precision manufacturing of the aluminum freeform mirrors is produced through a Single Point Diamond Turning (SPDT) - Nickel plating - Polishing process. For example, Nanotech 450 UPL and QED Q-FLEX 300 machines are able to used to fabricate freeform aluminum mirrors. The polishing process is required when using SPDT to aluminum alloy to remove toolmarks on the mirror surface that generated from the diamond turning machining process (Figure 4.9). Because aluminum mirror is too soft to directly polish the surface, Nickel plating is necessary before we polish diamond turned aluminum surface. The finished surface is coated on protected or enhanced aluminum to protect and increase reflectivity in visible. Metal mirror surface coating for infrared applications uses gold or silver for high reflectivity in infrared. The surface measurement of freeform mirrors with interferometers is challenging, so the Ultrahigh Accurate 3-D Profilometer (UA3P, Panasonic) is commonly used to measure it.

Freeform mirror surfaces can be expressed in the xy polynomial equations (4.4.1) and (4.4.2):

$$z = \frac{cr^2}{1+\sqrt{1-(1+k)c^2r^2}} + \sum_{j=2}^{66} C_j x^m y^n \tag{4.4.1}$$

$$j = \frac{(m+n)^2+m+3n}{2} + 1 \tag{4.4.2}$$

In the Equation 4.4.1 and 4.4.2, z is the sag of the mirror surface parallel to the z-axis, c is

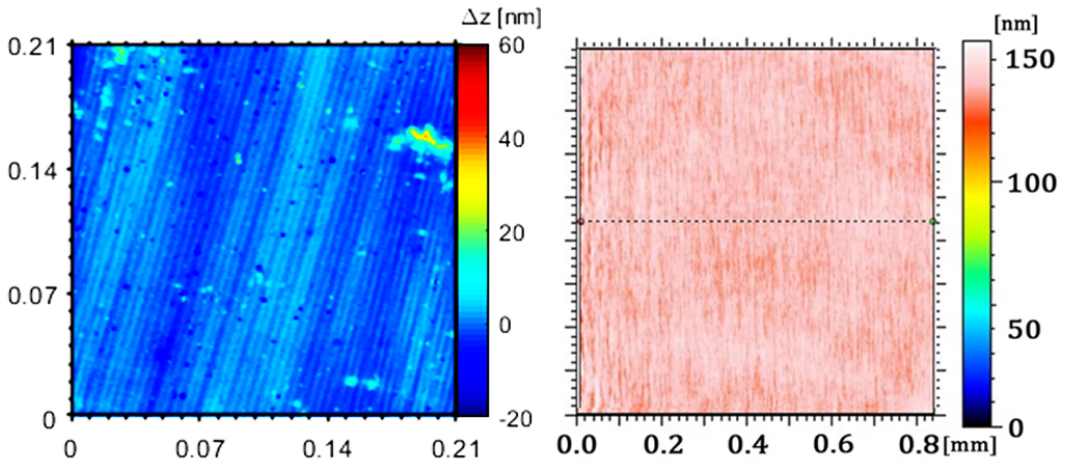

Figure 4.9: Aluminum mirror surface roughness from diamond turning machining without (left) and with (right) polishing process.

the vertex curvature, k is the conic constant, C_j is the coefficient of the monomial $x^m y^n$, and r^2 is $x^2 + y^2$. Coefficients of odd power of x terms are zero since mirror surfaces are symmetric to x variables (Chang, 2019).

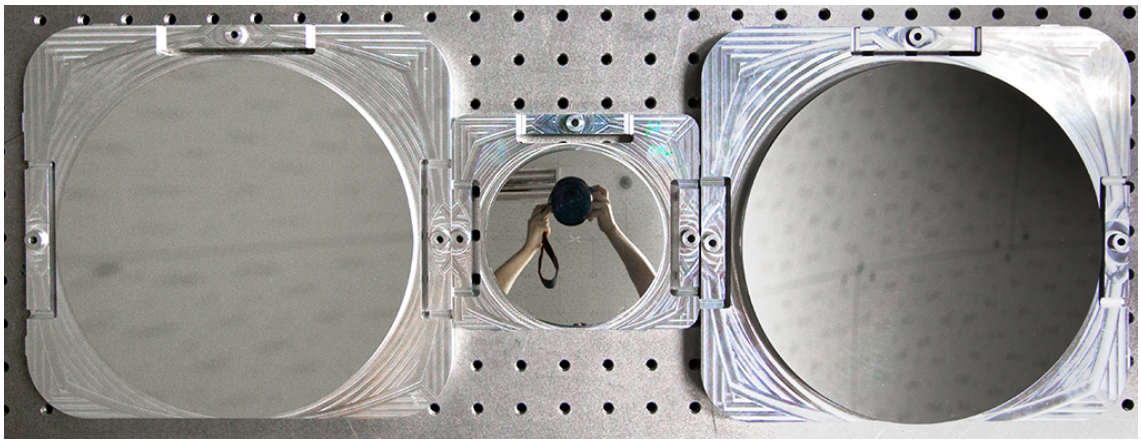

Figure 4.10: Fabricated freeform 6061-T6 aluminum mirrors: primary (left), secondary (middle), and tertiary (right) mirrors of LAF-TMS.

Figure 4.10 displays the fabricated freeform mirrors of LAF-TMS. The thermal expan-

sion slots and bent features in the mirror structure are designed to suppress thermal and mechanical stress on the reflecting surface. Mechanical deformations on the mirror surfaces due to the assembly process are minimized by optimizing these features.

Chapter 5

Tolerance Analysis

Optical performance can be degraded by fabrication, assembly process, thermal conditions, vibration environments from the launch system, and satellite platform vibration environments, so tolerance analysis has been considered an important step in optical system development to improve reliability and practicality of the system (Wang et al., 2013; Chen & Chen, 2015). The main objectives of tolerance analysis are to determine optical performance degradation due to external environments and to decide tolerance ranges of the system for fabrication and alignment (Bauman & Schneider, 2018).

Tolerancing parameters are x- and y- decenter, α-, β-, and γ- tilt, despace, and focus for general reflecting optics. Decenter and tilt are adapted to each mirror, while despace corresponds to inter mirror distance (Kim et al., 2010). The coordinate system for tolerance analysis is shown in Figure 5.1. Since we adjust the focal position to get the best image, the performance degradation from tolerances is compensated by the focal position.

At the start, the individual tolerance budget of each parameter and their sensitivity are explored with sensitivity analysis. Then, a statistical analysis based on the Monte Carlo method is performed to assess the system performance. Cumulative probability, which is the result of the Monte Carlo simulation, enables us to estimate the expected final system performance.

Contents of this chapter are published in the publication [1].

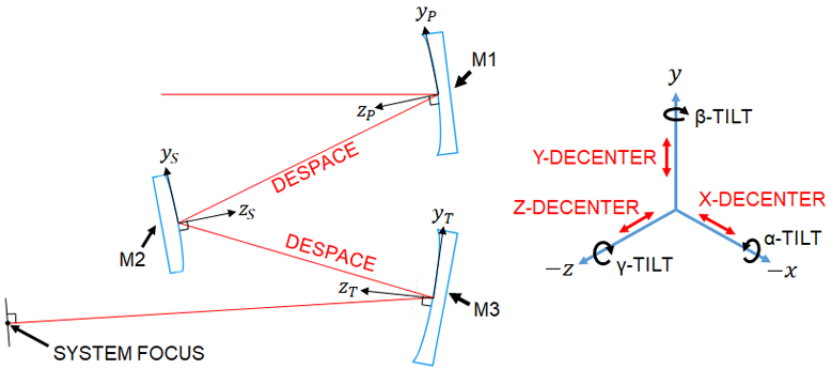

Figure 5.1: The coordinate system for tolerance analysis.

5.1 Sensitivity analysis

Optical component sensitivities are explored by individually implementing tolerance parameters (Lee et al., 2010). Performance criterion of the analysis is decided by scientific objective of the optical system. For instance, the modulation transfer function (MTF), root mean square (RMS) spot size, encircled energy diameter (EED), and RMS wavefront error are the typical criterion. Sensitivity analysis is performed at a few field angles within the field of view then they are averaged for each tolerance parameter. Initial tolerance ranges for sensitivity analysis are considered from typical fabrication tolerances listed in Table 5.1.

Table 5.1: Typical fabrication tolerances for optical astronomical applications

Quality	Surface figure error	Surface roughness	Tilt	Linear dimension
Precision	$\sim \lambda/16$	< 2 nm	arcsec	± 0.01 mm
General	$\sim \lambda/8$	2 - 4 nm	arcmin	± 0.05 mm
Low cost	$\sim \lambda/4$	> 5 nm	degree	± 0.1 mm

Figure 5.2 illustrates sensitivity analysis results of each tolerance parameter of the MATS satellite (Park et al., 2020). All parameters of M1 (primary mirror), M2 (secondary mirror), and M3 (tertiary mirror) correspond to red, blue, and magenta colors for plots (a

- c), (e - g), and (i - k). Inter mirror distances of M1-M2 and M2-M3 are indicated with green circles and green squares, respectively.

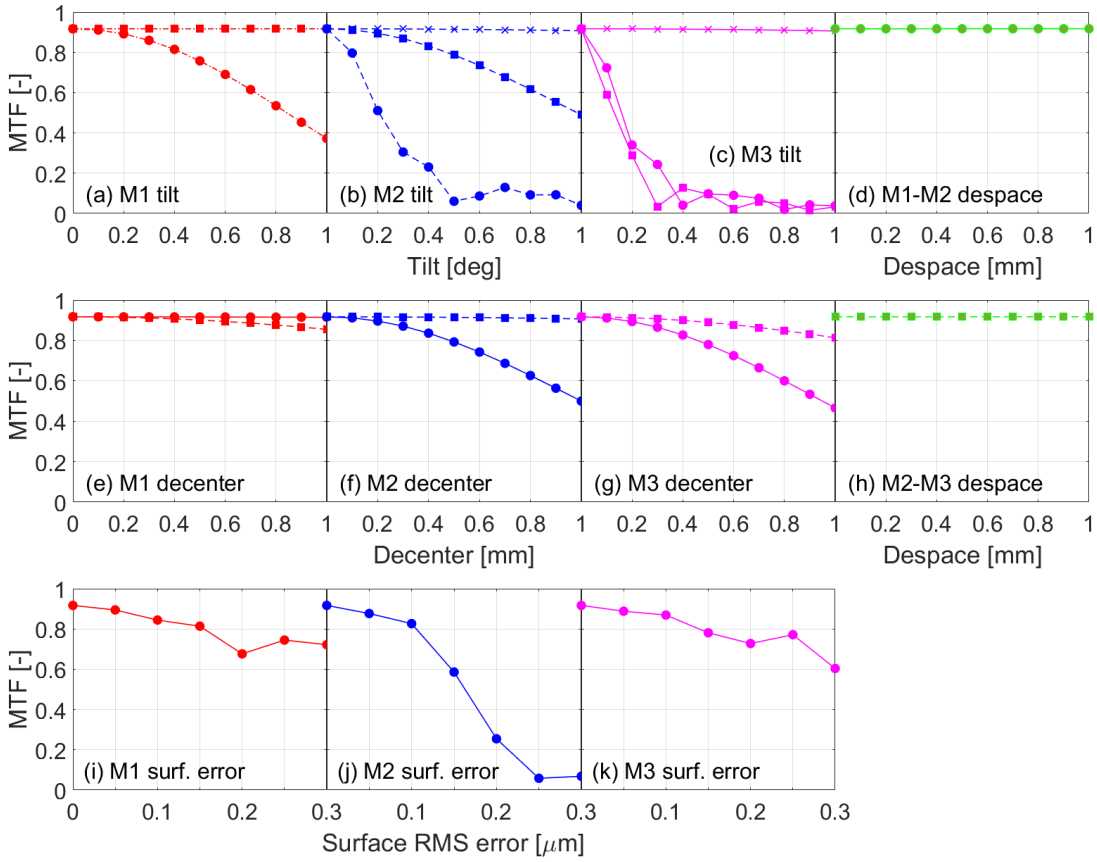

Figure 5.2: Sensitivity analysis results of M1 (red), M2 (blue), and M3 (magenta) of the MATS satellite: (a - c) α- (circle), β- (square), and γ- (cross) tilt, (e - g) x- (circle) and y- (square) decenter, (i - k) surface RMS error, (d) M1-M2 (circle), and (h) M2-M3 (square) despace. γ-tilt of M1 is overlapped with its β-tilt.

From the sensitivity analysis, we expect that α- tilt of M2, α- and β- tilt of M3, and surface RMS error of M2 are the parameters most critical for image quality degradation. On the other hand, the image quality is significantly less sensitive to γ- tilt and despace for all mirrors. In this system, α- or β- tilt of M3 is critical for image quality, so it can be set to the compensator for realignments.

Figure 5.3 summarizes sensitivity analysis of LAF-TMS on each surface's tilt, decenter, despace, and root mean square (RMS) error. The criterion of the sensitivity analysis is the 80 % encircled energy diameter (EED) for the point source with 0.532 μm wavelength. Sensitivities are calculated at five field angles, i.e., [α = -2.75°, β = -2.07°], [-1.38°, -1.03°], [0.00°, 0.00°], [1.38°, 1.03°], and [2.75°, 2.07°]. The mean values of 80 % EED from the five fields are taken for overall performance variation to decide tolerance limits of Monte Carlo simulation (Lee et al., 2010).

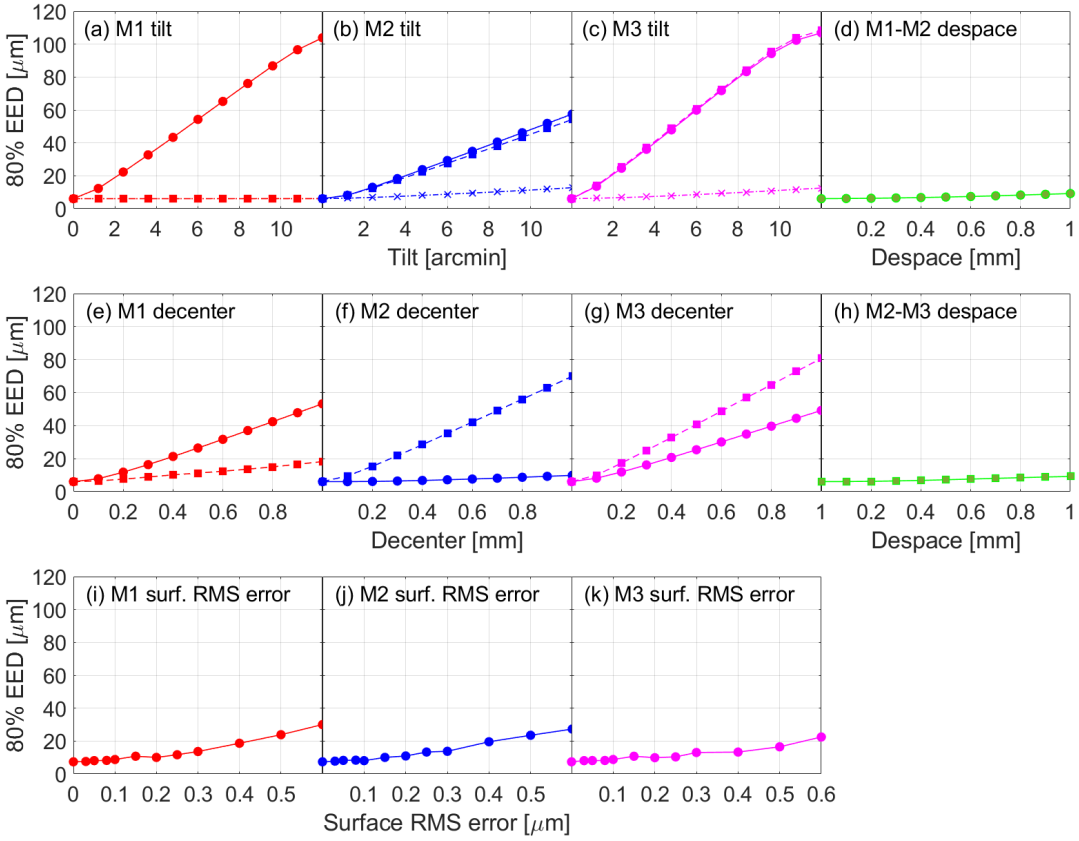

Figure 5.3: Sensitivity analysis results of M1 (red), M2 (blue), and M3 (magenta) of LAF-TMS: (a - c) α- (circle), β- (square), and γ- (cross) tilts, (e - g) x- (circle), and y- (square) decenters, (i - k) surface RMS errors, and (d) M1-M2 (circle), (h) M2-M3 (square) despaces. γ-tilt of M1 overlaps with its β-tilt, and α-tilt of M3 also overlaps with its β-tilt.

M1, M2, and M3 are indicated in red, blue, and magenta, respectively. Calculated EED results of negative and positive tolerances are symmetry. Analysis results show that despaces, γ- tilts for all three mirrors, β- tilt, y-decenter of M1, and the x-decenter of M2 are practically insensitive parameters, which highlight the robustness of the LAF-TMS design solution. By considering mechanical fabrication tolerances, α- and β- tilts are the most sensitive parameters. Decenter is less sensitive compared to tilt as we often assemble and align optical components within $\pm$0.1 mm tolerances. M3 is slightly less sensitive than the other mirrors in terms of the surface RMS error.

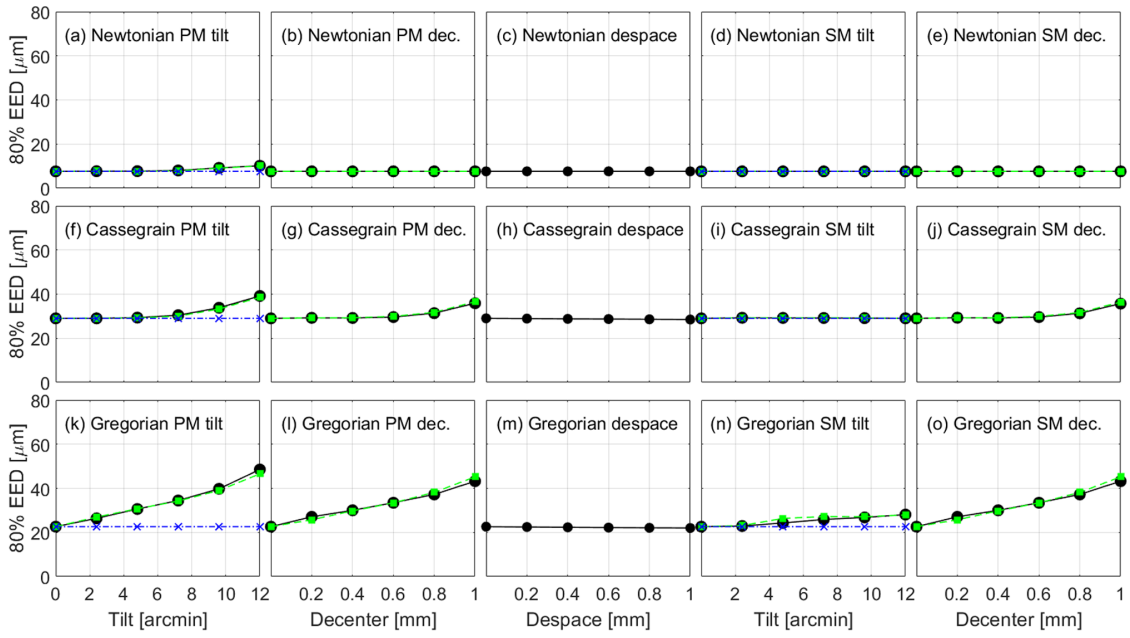

Figure 5.4: Sensitivity analysis of Newtonian (top), Cassegrain (middle), and Gregorian (bottom) systems: (a, d, f, i, k, n) α- (circle), β- (square), and γ- (cross) tilts, (b, e, g, j, l, o) x- (circle) and y- (square) decenters, and (c, h, m) despace.

Figure 5.4 indicates sensitivity analysis of the TRT Kit for the image center. Surface α-, β-, and γ- tilts, x- and y- decentration of each mirror, and despace are examined for sensitivity in the Newtonian, Cassegrain, and Gregorian telescope configurations. The criterion of the analysis is 80% encircled energy diameter (EED) for the 550 nm wavelength,

and the focus is set as the compensator. 80% EED is displayed for each of the perturbed system parameters across all three telescope configurations. Calculated sensitivities for negative perturbations are symmetric to the positive cases.

The Newtonian secondary mirror is a simple flat used to fold the optical path and does not affect optical performance. It is shown as constant 80% EED curves across decenters of the primary and secondary mirrors, tilts of the secondary mirror, and despace in Figure 5.4. Despace is not critical to optical performance for all three systems. Decenters of the primary and secondary mirrors have the same trends because they are directly coupled to each other. α- and β- tilts of the primary mirror are the most sensitive parameters for all three systems.

5.2 Monte Carlo simulation

Sensitivity analysis provides performance sensitivity for each of the optical component errors. However, it is necessary to confirm the system tolerance limits when all tolerances simultaneously affect the system. The Monte Carlo method is the most common way to predict the cumulative probability for meeting specific performance requirements (Kuś, 2017; Burge et al., 2010).

Initial tolerance limits are estimated from the root sum square of each parameter of optical components calculated from sensitivity analysis, and they are optimized within fabrication and alignment error budgets (Funck & Loosen, 2010). OpticStudio and CODE V are used for the Monte Carlo simulation. Table 5.2 lists tolerance parameters and the final tolerance limits of the MATS satellite and LAF-TMS that are calculated using the iterative method. In this case, tolerance limits are the same for all mirrors. Focus is selected as a compensator, and the reference wavelength is the same as the one used in the sensitivity analysis.

Tolerance distributions for the Monte Carlo simulation follow a normal distribution. Figure 5.5 shows the histograms of 5,000 Monte Carlo tries that are binned as a function of MTF or RMS spot diameter. Required optical performances of the MATS satellite (i.e.,

Table 5.2: Tolerance limits for the Monte Carlo simulations for the MATS satellite and LAF-TMS

Parameter	Tolerance limits[a]	
	The MATS satellite	LAF-TMS
x-, y- Decenter	±0.5 mm	±0.15 mm
α-, β- Tilt	±0.15°	±1.2′ (=±0.02°)
Despace	±1.0 mm	±0.5 mm
Focus[b]	±1.0 mm	±0.5 mm

[a] Tolerance limits are the same for M1, M2, and M3.

[b] Focus is used as the compensator.

0.3 MTF) and LAF-TMS (i.e., 12 μm) are met at 96% and 91% cumulative probabilities, respectively. Surface RMS errors of freeform mirrors are not simple to be applied to the Monte Carlo simulation. Instead, we estimate effects of surface errors on optical performance. From the sensitivity analysis of the surface RMS errors (Figure 5.2), as an example, we expect that ∼0.03 MTF could be additionally degraded when taking count the fabricated surface RMS errors of ∼0.05 μm in the case of the MATS satellite.

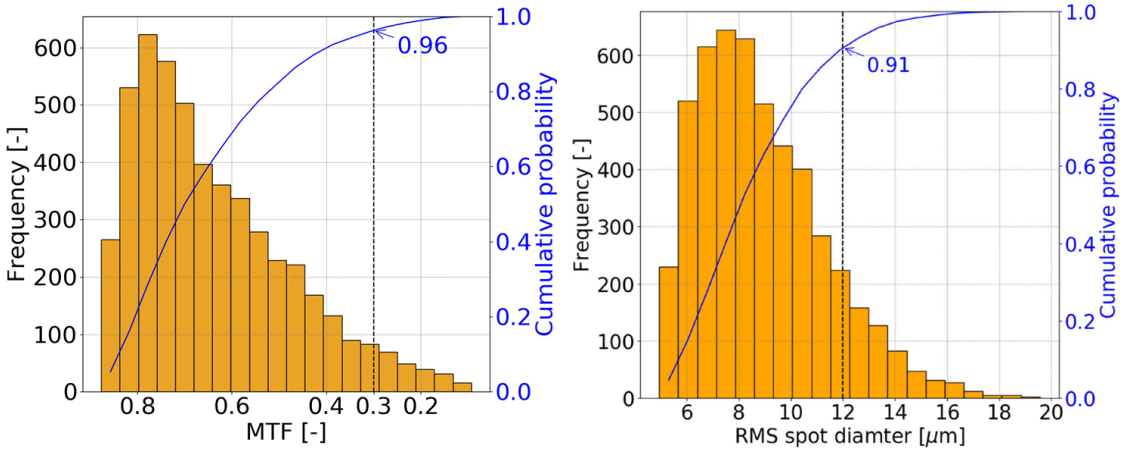

Figure 5.5: Monte Carlo simulation results of the MATS satellite (left) and LAF-TMS (right). The performance limit is indicated by a black dashed line. The blue solid line represents a cumulative probability curve.

Monte Carlo simulation of the TRT Kit is performed for α- and β- tilts, x- and y- decenters, despace, and surface irregularity. All three TRT configurations have conic mirror surfaces, so it is possible that we directly examine the surface irregularity on the Monte Carlo simulation. The simulation is evaluated with 5000 trials at the 550 nm reference wavelength. The focus is set as the compensator to recover performance. The performance criterion is 12 μm for 80% EED which is based on the Nyquist sampling requirement for a sensor with 6 μm pixels.

Tabel 5.3 lists the final tolerance ranges of three TRT configurations from the Monte Carlo simulation. The Gregorian is the most sensitive of the three systems analyzed. Overall tolerance ranges are acceptable and are within general fabrication and alignment errors.

Table 5.3: Tolerance limits of Newtonian, Cassegrain, and Gregorian from the Monte Carlo simulations.

Parameter		Newtonian	Cassegrain	Gregorian
α-, β- Tilt	Primary mirror	$\pm\ 23'$	$\pm\ 4'$	$\pm\ 2.5'$
	Secondary mirror	$\pm\ 32'$	$\pm\ 10'$	$\pm\ 5'$
x-, y- Decenter		$\pm$ 1 mm	$\pm$ 0.6 mm	$\pm$ 0.5 mm
Despace		$\pm$ 3 mm	$\pm$ 1 mm	$\pm$ 0.7 mm
Surface Irregularity		$\pm$ 2.5 λ	$\pm$ 0.50 λ	$\pm$ 0.35 λ
Focus[a]		$\pm$ 20 mm		

[a] The focus is set as the compensator.

Chapter 6

Optical Alignment

6.1 Three-point laser alignment

Optical alignment is performed before we verify and demonstrate the optical performance of the system. The purpose of the alignment is to compensate for coordinate errors of fabricated optical components. There are a few practical methods to align on-axis systems but off-axis system alignments are not very common. Shack-Hartmann wavefront sensors and Coordinate Measurement Machines (CMM) are generally used for optical alignment (Wu et al., 2016). Three-Point Laser Alignment (TPLA) is another practice used to align optics. TPLA uses three mounted lasers aligned parallel to the optical axis of the primary mirror.

The laser mount for TPLA contains a screen with holes at points optically conjugate to the sources. A flat mirror is placed at the focal plane of the optical system. First, the laser sources are emitted at the screen. Then, the beams reflect off of the primary mirror and converge towards the secondary mirror. For the Newtonian design, the flat secondary mirror then folds the optical path. Finally, the beams reflect off of the flat at the focal

Contents of this chapter are published in the publications [2] and [3].

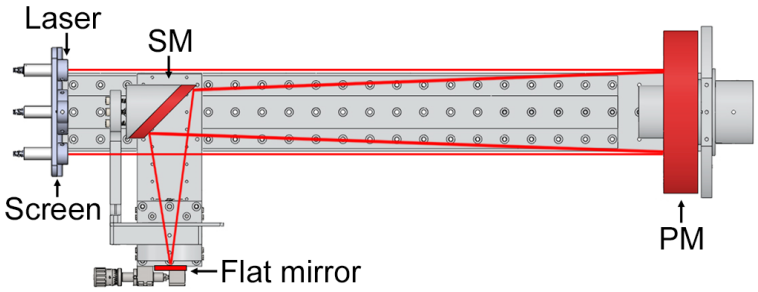

Figure 6.1: Layouts of TPLA for the Newtonian telescope. This method can be adapted to the other types of telescopes (PM: primary mirror, SM: secondary mirror, F: focal point).

point and return through the optical system to the screen. The laser sources reflect back through the optical system to the conjugate points of the sources only when all optical components are well aligned (see, Figure 6.1).

Figure 6.2 shows pictures of TPLA alignment process applied to the TRT Kit. There are 3 mm diameter alignment holes at the conjugate points of the laser sources (panel (a) in Figure 6.2) that are used for fine alignments. We measure coincidence of the laser point and the hole by eyes within 0.5 mm uncertainty that corresponds to $0.71'$, $0.18'$, and $0.14'$ tilt errors of the secondary mirror in Newtonian, Cassegrain, and Gregorian, respectively. These alignment accuracy are acceptable by comparing to tolerances of the telescopes (Table 5.3).

6.2 3-2-1 position alignment

The 3-2-1 position principle is an optical alignment and positioning method that uses three, two, and one contact points for each cubic surface of an optical component and an optomechanics (Trappey & Liu, 1990). Figure 6.3 represents the mechanical design of the LAF-TMS mirror and the alignment mechanism that allow the adjustment capability to compensate for any residual manufacturing errors beyond the tolerance limits.

Shims are placed between mirrors and the mirror holder and the L-bracket is mounted underneath the mirror to support it. The mirror and shims contact at three points. The

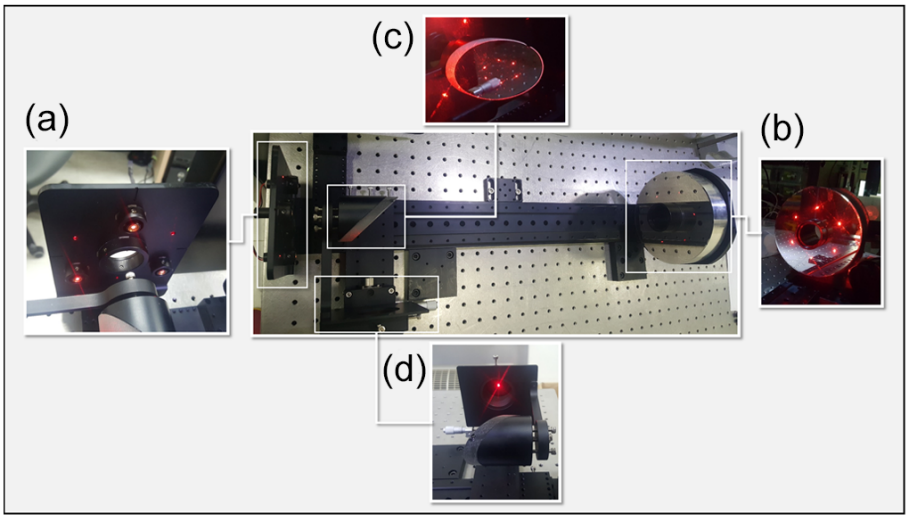

Figure 6.2: The TRT Kit alignment with TPLA method. (Center) The laser mount attached to the TRT Kit. (Sub-pictures) (a) The lasers come from the source, (b) and are reflected by the primary mirror, (c) the secondary mirror, (d) and the flat mirror. After traveling back through the system, (a) the beams reach the screen.

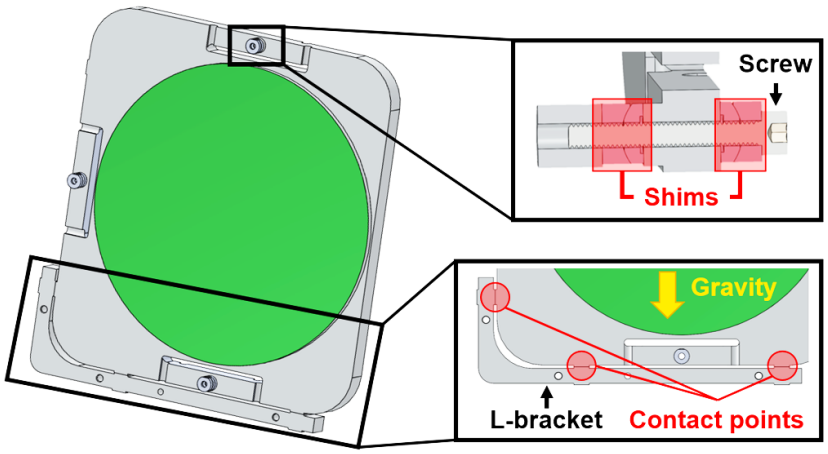

Figure 6.3: Mechanical design of the freeform aluminum mirror. (sub-figures) Precision made with the same aluminum material and alignment mechanisms are shown.

mirror and the L-bracket meet at two and one contact points for each surface. Tilt and decenter errors can be compensated thanks to shims and L-brackets that can be chosen in different thicknesses for relocations of the optical components.

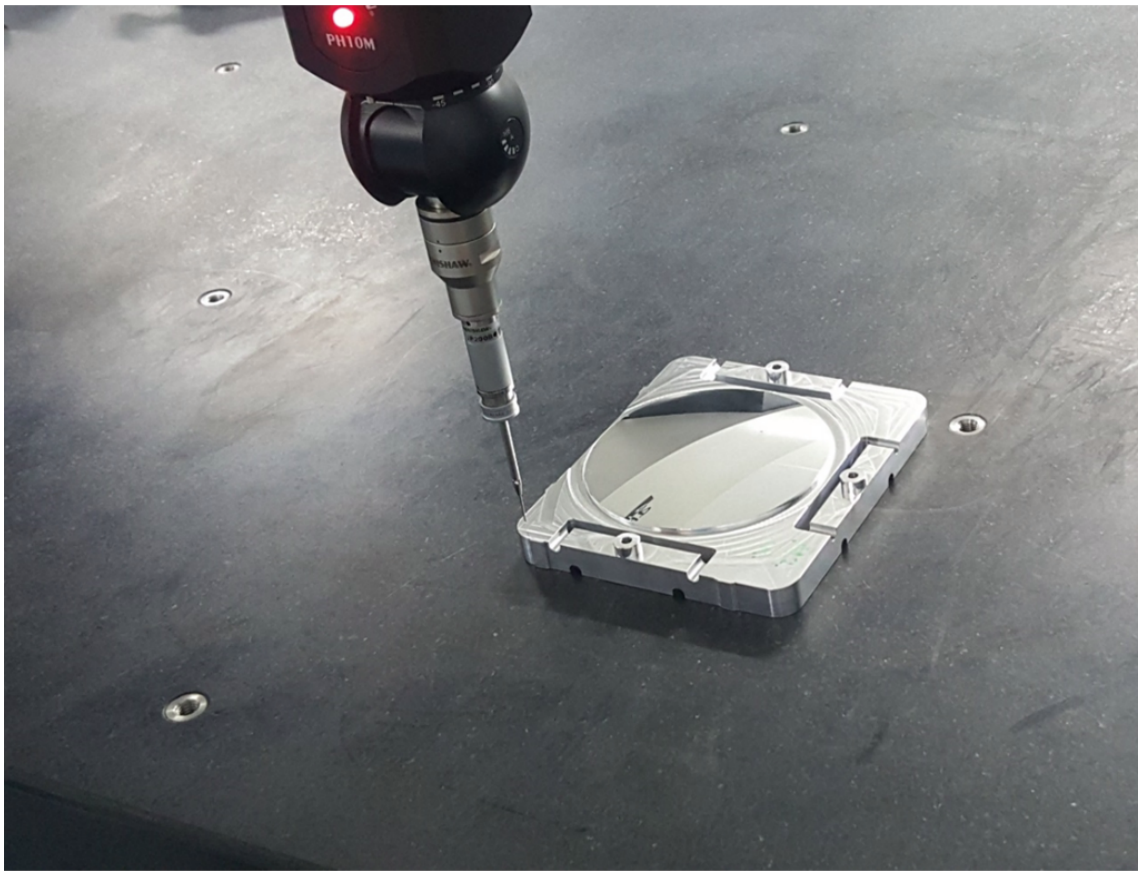

Figure 6.4: The picture of a CMM measurement process to get the LAF-TMS mirror coordinates.

In order to know alignment errors, coordinates of optomechanical structure and mirrors are measured with coordinate measurement machine (CMM) like the Dukin MHB CMM (Figure 6.4). Measured data points of each mechanical surface are fitted by using the least square fitting algorithm. All the fitted surfaces are compared with those of the designed nominal surfaces to calculate tilt and decenter of the mirrors.

Alignment accuracy of the 3-2-1 position alignment method depends on the mirror

size and fabrication accuracy of shims or L-brackets. For instance, alignment accuracy of x- and y-decenters and despace are ± 0.02 mm, when we fabricate shims and L-brackets within ± 0.02 mm fabrication tolerance. Alignment accuracy of α- and β-tilts are $2.20'$ and $0.71'$ for the M1 of the MATS satellite, and $0.60'$ and $0.30'$ for the M1 of LAF-TMS for ± 0.02 mm fabrication tolerance of shims. All alignment accuracy of the MATS satellite and LAF-TMS are acceptable by comparing to each of tolerance limits which simulated from the Monte Carlo simulations (Table 5.2).

Chapter 7

Performance Tests

Performance of the optical system must be evaluated through indoor or outdoor (field) tests. Indoor optical tests take place in a dry cleanroom to prevent contamination of optical components from dust particles and moisture. Temperature should be considered for performance tests especially of infrared cameras. Figure 7.1 displays the imaging test setup of the MATS satellite that installed on an optical table and a rotary stage so that the optical tests could be performed not only at the image center but also over full image fields. The collimator generates some targets such as a point source, a USAF target, an edge target which is for MTF measurements, a distortion target, etc.

7.1 USAF target and MTF measurement

The 1951 USAF target is a useful indicator for finding the approximate focus and for visually inspecting the optical performance. Horizontal and tangential three bar patterns are listed across the target that separated by group (numbered on the top of patterns) and element (numbered on the side of patterns) numbers. Spatial frequency of each element is calculated by

Contents of this chapter are published in the publications [1], [2], and [3].

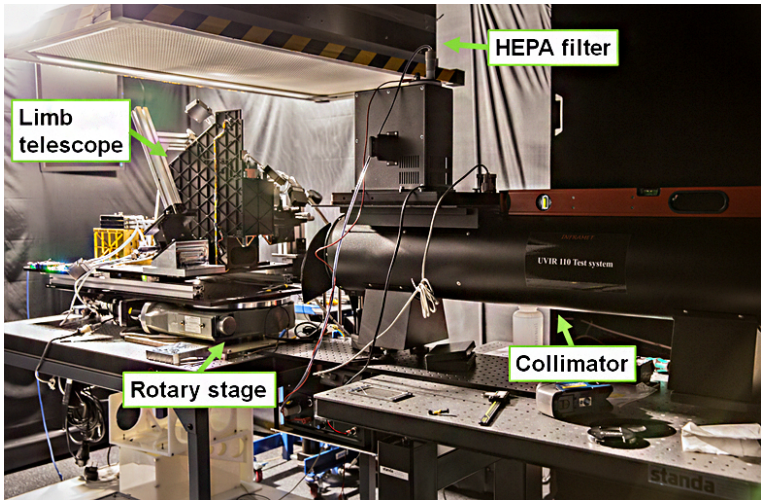

Figure 7.1: The optical test setup for characterization and optical performance measurements of the MATS satellite. The limb telescope is installed under the HEPA filter and the fan (left-side), and the collimator sits in front of the limb entrance aperture (right-side).

$$2^{(Group\ No.+(Element\ No.-1)/6)}[lp/mm] \tag{7.1.1}$$

where, lp indicates line pair. Table 7.1 lists spatial frequency of each USAF target element.

Table 7.1: Spatial frequency of the 1951 USAF target in lp/mm

Group\Element	1	2	3	4	5	6
0	1.00	1.12	1.26	1.41	1.59	1.78
1	2.00	2.24	2.52	2.83	3.17	3.56
2	4.00	4.49	5.04	5.66	6.35	7.13
3	8.00	8.98	10.08	11.31	12.70	14.25
4	16.00	17.96	20.16	22.63	25.40	28.51
5	32.00	35.92	40.32	45.25	50.80	57.02

Figure 7.2 shows the USAF target images in UV2, IR1, IR2, IR3, and IR4 observed by the MATS satellite, which has a focal length of 261 mm. The USAF target images are generated by the collimator with a 1000 mm focal length (see Figure 7.1). Spatial frequency

of the USAF target image needs to be re-calculated by considering the magnification of the test setup. In the case the target is generated by the collimator and is taken by the camera system, the final USAF target image resolution is

$$2^{(Group\ No.+(Element\ No.-1)/6)} \times \frac{f_{collimator}}{f_{camera}}[lp/mm]. \tag{7.1.2}$$

For example, spatial frequency of group 2 element 4 bars with the MATS satellite imaging system is calculated to 5.66 × 1000 / 261 = 21.67 lp/mm.

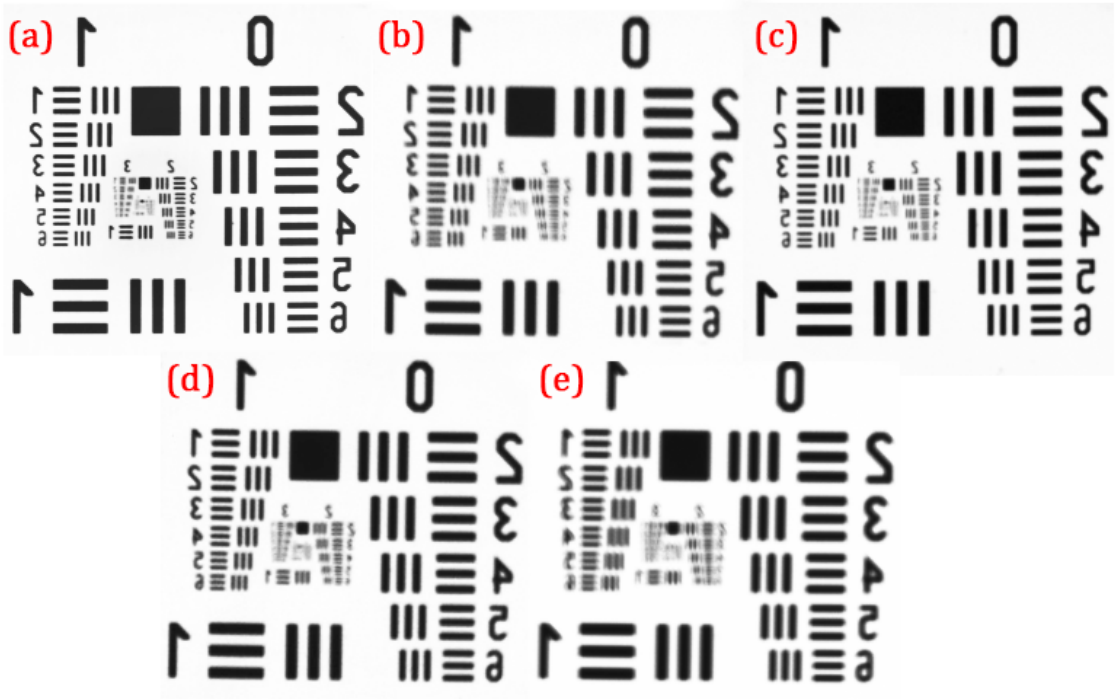

Figure 7.2: USAF target images from the limb telescope in (a) UV2, (b) IR1, (c) IR2, (d) IR3, and (e) IR4. A USAF image in UV1 not exists because of the low transmission of the target in 270±1.5 nm wavelength.

MTF, also called contrast, is the most common optical performance criterion, especially for imaging cameras. MTF is defined by

$$MTF = \frac{I_{max} - I_{min}}{I_{max} + I_{min}} \tag{7.1.3}$$

where, I_{max} and I_{min} are the maximum and minimum intensity of the target (Figure 7.3).

(Spatial) Cutoff frequency defines the maximum spatial frequency of the optical system that corresponds to the smallest object resolvable by the system. It depends on wavelength and F-ratio of the system,

$$\xi_{Cutoff} = \frac{1}{\lambda \times \texttt{F/\#}}[lp/mm]. \tag{7.1.4}$$

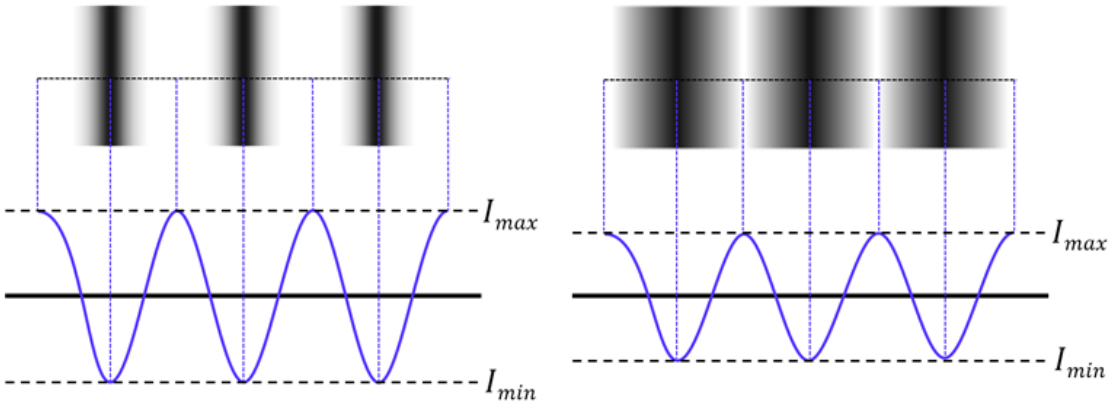

Figure 7.3: Definition of MTF in the high contrast image (left) and the low contrast image (right).

In general, the optical system is not able to resolve the target to cutoff frequency due to limitations from the pixel size of the detector. So we define another frequency limit, the maximum spatial resolution of the optical system with considering the pixel size, called Nyquist frequency that only takes into account the pixel size,

$$\xi_{Nyquist} = \frac{1}{2 \times Pixel\ size}[lp/mm]. \tag{7.1.5}$$

MTF can be measured using the USAF target but this measurement is limited by a resolution of spatial frequency, uncertainty from the target size, and a pixel size of the detector. To overcome these problems, a slanted edge test target is used for MTF measurements. The slanted edge target has a slanted angle (θ) of 1° - 6° to minimize MTF uncertainty from the pixel size (Figure 7.4).

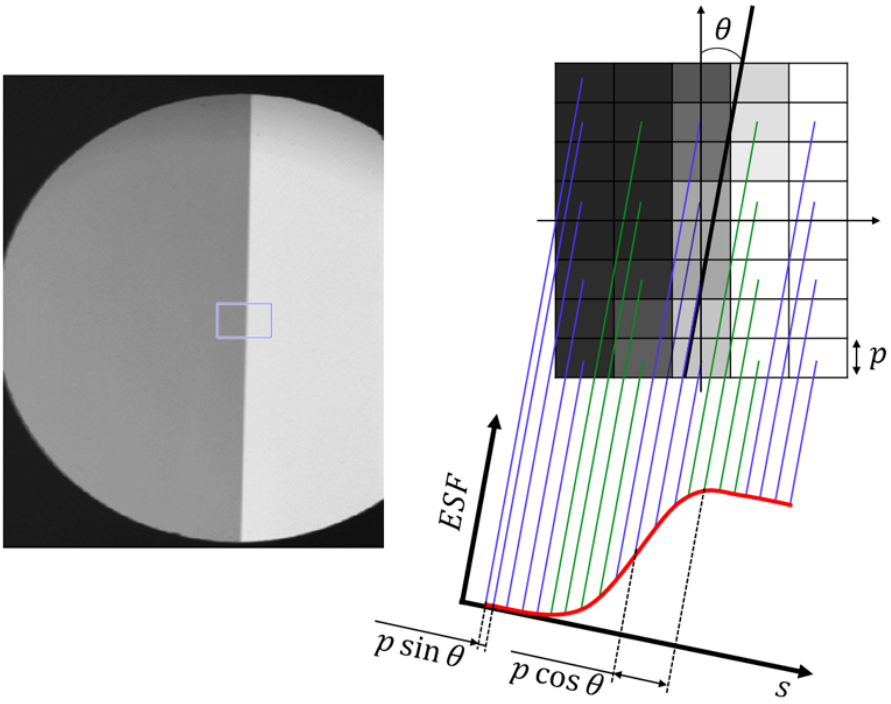

Figure 7.4: The slanted edge target for MTF measurements (left) and the ESF calculation mechanism.

Sharpness of the edge across the image position can be expressed with the edge spread function (ESF). It is transformed into line spread function (LSF) by taking derivative of the ESF. The final MTF curves are derived by taking the Fourier transform and normalizing it (Fujita et al., 1992; Judy, 1976; Padgett & Kotre, 2006; Samei et al., 1998; Zhang et al., 2012). Figure 7.5 illustrates MTF curve of the MATS satellite that calculated from the slanted edge target measurements. The resolution criterion is different by the scientific purpose but generally it takes 0.3 or 0.5 MTF to required spatial frequency. Resolution requirement of the MATS satellite is 0.3 MTF at 20 lp/mm for UV channels and at 10 lp/mm for IR channels. MTF measurement results (Figure 7.5) show that the optical performance in UV2 is very close to its requirement and the performance in IR channels satisfy their requirements.

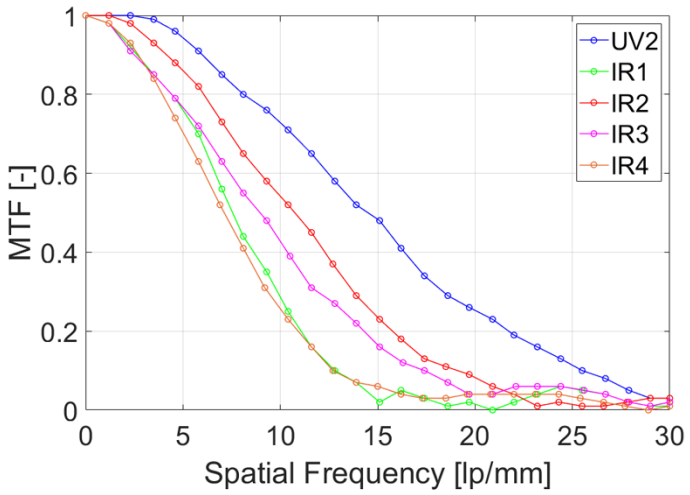

Figure 7.5: Measured MTF curves of UV and IR channels of the MATS satellite.

7.2 Point source test

Point source tests are useful to precisely found focal positions, evaluate optical aberrations, and measure the system performance. The size of a point source image can be evaluated by various methods, measuring RMS spot size, full width at half maximum (FWHM), 80% EED, and Strehl ratio. RMS spot size is the average ray deviation root square, and is mostly calculated from optical design software such as CODE V, OpticStudio, LightTools, etc. FWHM is commonly used in astronomy to measure the size of observed point source targets. 80% EED and Strehl ratio are useful to performance measurements for evaluation of the system. Encircled energy of the airy disk is given by

$$EE(r) = 1 - \left(1 + \sum_{i=1}^{\infty}(-1)^i \frac{(\pi r/2)^{2i}}{i!}\right)^2 - I_{(r)}(\pi r/2)^2 \tag{7.2.1}$$

where, r is image radius in the unit of λF and $I_{(r)}$ is a normalized intensity that calculated from Equation 3.1.3. Strehl ratio (S) approximately calculated as a function of an RMS wavefront error (σ),

$$S \approx \exp\left[-(2\pi\sigma)^2\right] \tag{7.2.2}$$

but this approximation is acceptable when the wavefront error is smaller than 0.1 wave (Mahajan, 1982; Smith, 2007).

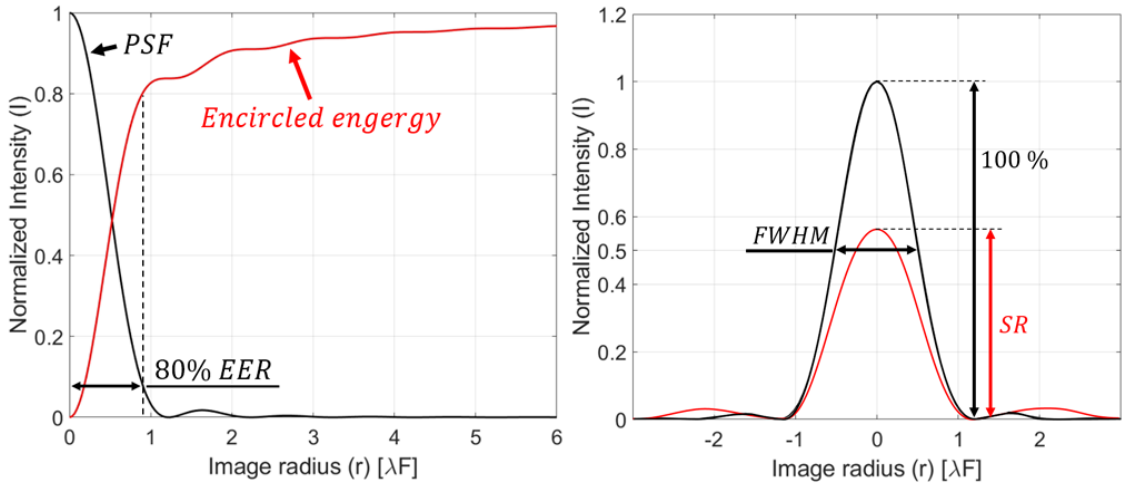

Figure 7.6: The relation between encircled energy and point spread function (PSF) of the perfect optics (left), and Strehl ratio (SR) of the aberrated PSF (red) and FWHM of the perfect optics are indicated (right). EER represents an encircled energy radius, which is the half of EED.

Figure 7.6 illustrates the relation between point spread function (PSF) of the airy disk and its encircled energy on the left panel, and Strehl ratio and FWHM are indicated on the right panel.

For optical performance tests, the collimator system is required that can be also tilted for full field tests. It consists of a white Light Emitting Diode (LED, or other light sources), integrating cylinder, diffuser, a pinhole (or other targets), and high quality collimation lens. Figure 7.7 illustrates the layout of the imaging test setup, including the collimator and LAF-TMS prototype.

Figure 7.8 shows the contour plot of the point source image and its spot size of LAF-TMS at the field center. The test setup is used a 3.75 μm pixel-sized CCD, QHY 5-II mono, to minimize measurement errors. The position of the sensor is controlled by a linear stage with 0.01 mm accuracy. The final image is subtracted dark frames and stacked 10

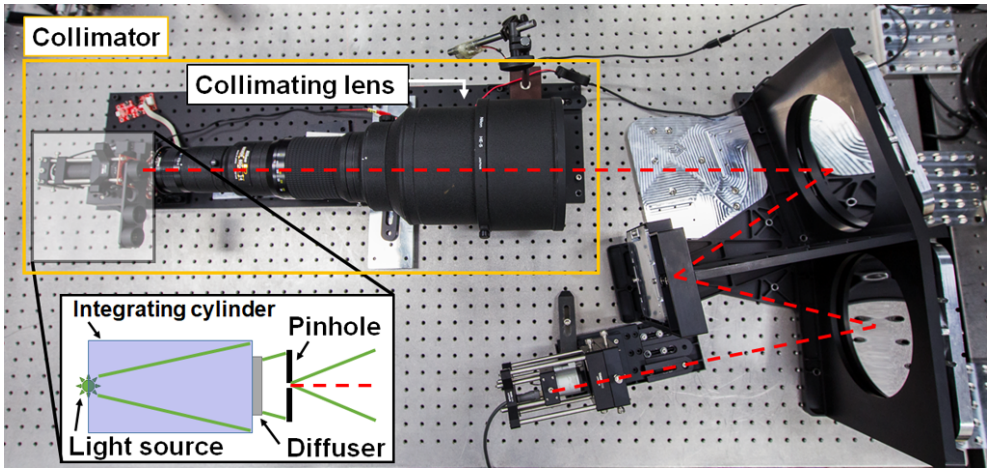

Figure 7.7: Optical test setup for point source imaging tests. The collimator is located on the left side, and LAF-TMS is installed on the right side. Optical axis ray is indicated in a red dashed line. (sub-figure) The optical layout of the collimator is illustrated in the black box.

images to increase signal to noise ratios. LAF-TMS has imaging performance with the full width at half maximum (FWHM) of 37.3 μm (the right panel in Figure 7.8). Since optical performance of LAF-TMS targets the H2RG SCA infrared detector with the pixel size of 18 μm (Blank et al., 2012), the spot size closely meets the Nyquist sampling theorem.

The large wing in the point spread function of the LAF-TMS point source image is the result of large surface micro roughness of its mirrors (Ingers & Breidne, 1989; Harvey, 2013).

In addition to the center-field imaging performance verification, it is critical to perform the full field of view tests to confirm off-axis aberrations such as coma, astigmatism, field curvature, linear astigmatism, etc. The whole instruments or the collimator should be rotated with a rotational axis at the center of the primary mirror surface for the full field of view tests.

Figure 7.9 illustrates full field of view test results in IR2 of the MATS satellite. In this case, as we can clearly see in the figure, there are no dominant off-axis aberrations detected

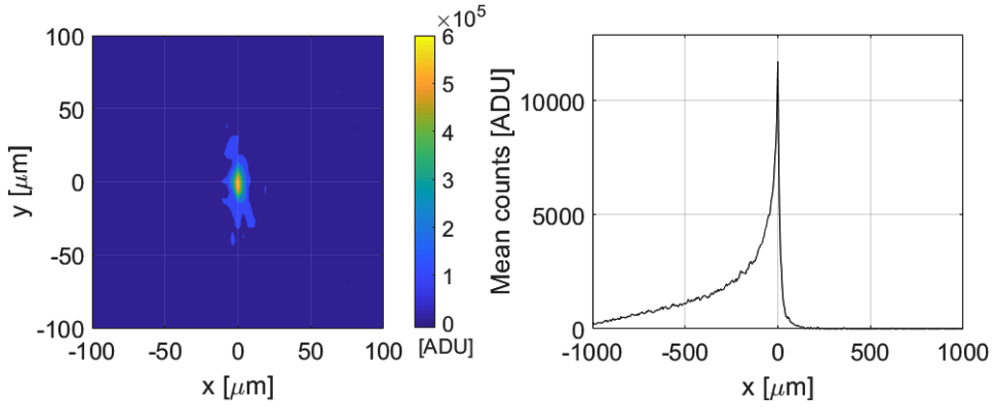

Figure 7.8: The contour plot of the point source image at the field center (left), and its spot size of LAF-TMS (right).

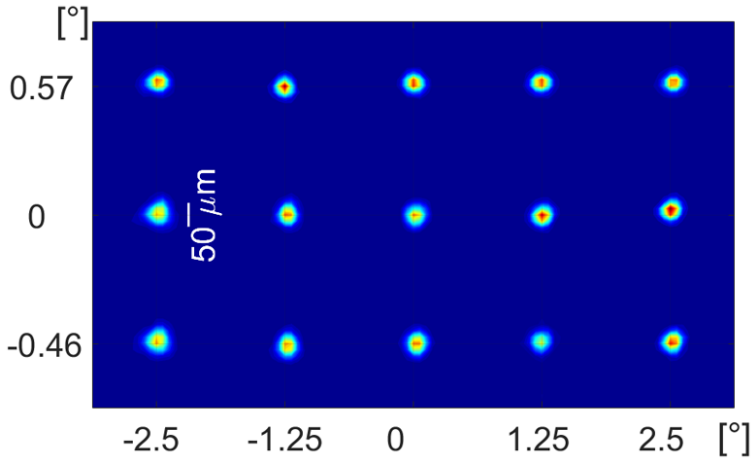

Figure 7.9: Full field imaging results with the 100 μm pinhole in IR2. The white scale bar indicates 50 μm. The designed spot diagram of the MATS satellite is shown in Figure 4.8, (b).

over a full field of view. The geometry of the spot images is almost uniform while optical performance degradations are not noticeable, indicating that field curvature is negligible.

7.3 Field test

Optical tests in the cleanroom can evaluate the system performance, but field tests are important especially for outdoor optical systems such as telescopes, digital camera lenses, etc. Temperature, atmospheric, and stray light effects are measurable through the field tests.

Figure 7.10 includes field test pictures that are taken with (a) the Newtonian, (b) Cassegrain, and (c) Gregorian telescopes of the TRT Kit. Optical layout of the TRT Kit is shown in Figure 4.1. These three pictures clearly indicate the difference in field of view of the three configurations. The picture captured with the Gregorian telescope also shows the optically reversed image (see, (c) in Figure 4.1).

Figure 7.10: The TRT Kit field test pictures. The pictures were captured with the (a) Newtonian, (b) Cassegrain, and (c) Gregorian telescopes, respectively.

Figure 7.11 depicts the Messier 27 (M27) nebula captured using the Newtonian TRT Kit configuration. The observation demonstrates great optical performance capable of imaging detailed structures of the extended source and the fine circular shapes of stars across the field.

Figure 7.11: The M27 nebula with stars that were observed using the Newtonian telescope.

Chapter 8

Optical Characterization

Optical system calibration allows estimations of power and incident angles of the light entering the entrance pupil (Hagen, 2014). It considers not only systematic noise corrections that are bias, dark, and flat-field corrections in CCD data (Birney et al., 2005), but also characterizations of total system throughput, relative pointing, distortion, etc. It is important to characterize total system throughput and relative pointing of each channel for multi-channel telescopes. In this chapter, we will introduce some characterization process of the limb telescope that has six channels and 19 optical components including mirrors, beam splitters, broad, and narrow bandpass filters.

8.1 Total system throughput

In the splitter box of the MATS telescope system, the incident beam from the off-axis telescope is split into six channels (see Figure 8.1). Verification of transmittance and reflectivity of each optical component is necessary to calculate the total throughput of the system and then to decide the CCD gain, the exposure time, etc. Furthermore, reflectivity of the optical mirror needs to be measured for the characterization of the scattered light

Contents of this chapter are published in the publication [1].

from high surface roughness mirrors (Harvey, 2013; Ingers & Breidne, 1989).

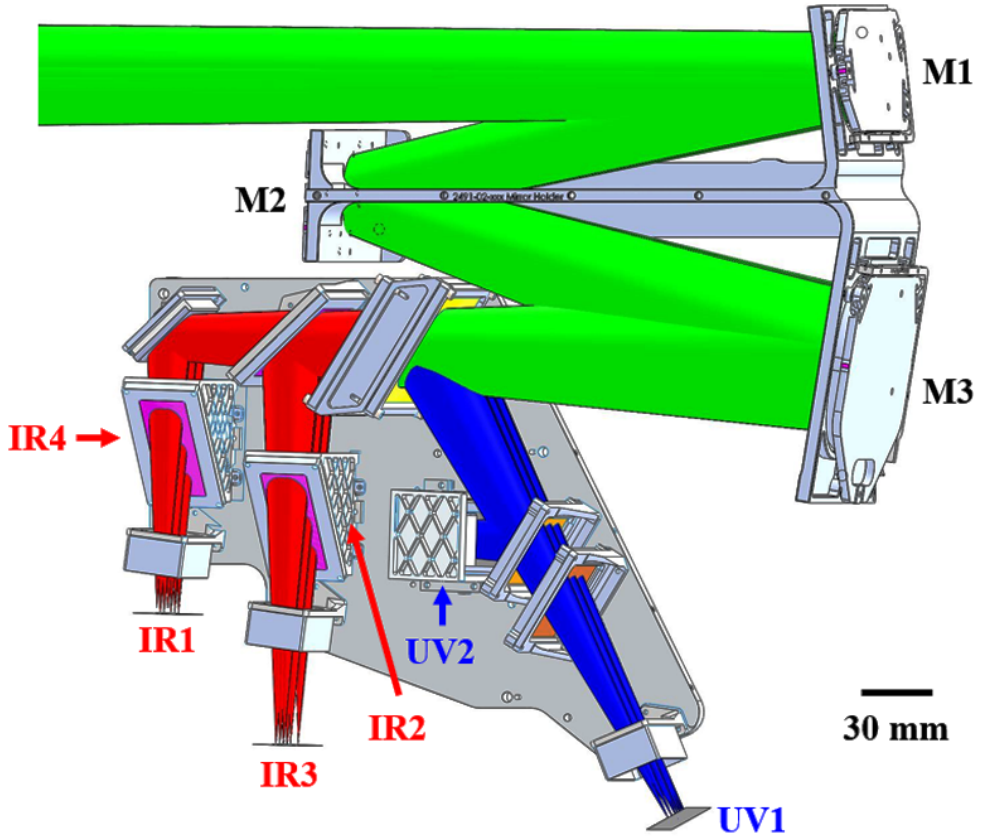

Figure 8.1: The optical layout of the limb telescope. UV2, IR2, and IR4 CCDs are located at the backside of the instrument.

Transmittance and reflectivity of filters and beam splitters have been measured by the component providers. We used the Andor iDus spectrometer and 1kW Xenon lamp to measure specular reflectivity of the mirrors. Measurement results are listed in Table 8.1. Beam splitters, broadband filters, narrowband filters, and folding mirrors are abbreviated as BS, FB, FN, and FM, respectively. All the reflectivity and transmittance values are based on the central wavelength of each channel.

IR1 and IR2 show relatively high total throughput ($> 12\%$) while other channels have

Table 8.1: Bandpass, reflectivity, and transmittance of optical components[a].

Channel	WL (nm)	Mirror (-)	BS1 (-)	FB1 (-)	BS2 (-)	FM (-)	BS3 (-)	FN (-)	CCD QE (-)	Total (%)
UV1	270±1.5	0.86	1.0 (R)	0.70	0.50 (T)	-	-	0.38	0.50	4.2
UV2	304.5±1.5	0.80	1.0 (R)	0.69	0.51 (R)	0.79	-	0.41	0.55	3.2
IR1	762±1.8	0.88	0.96 (T)	0.97	0.45 (T)	0.88	0.60 (T)	1.0	0.78	12
IR2	763±4.0	0.88	0.96 (T)	0.97	0.55 (R)	-	0.75 (R)	0.98	0.78	20
IR3	754±1.5	0.88	0.96 (T)	0.98	0.55 (R)	-	0.25 (T)	0.77	0.80	5.4
IR4	772±1.5	0.88	0.96 (T)	0.98	0.45 (T)	0.88	0.40 (R)	0.81	0.76	6.2

[a] WL: Wavelength, BS: Beam splitter, FB: Broadband filter, FN: Narrowband filter, FM: Folding mirror, QE: Quantum efficiency, (R): Reflectivity, (T): Transmittance

throughput between 3.2 - 6.2%. Low throughput is already expected by design. However, the MATS satellite observes the earth mesosphere, which is bright enough with the adequate CCD gain, and exposure time (∼3 seconds). The three off-axis mirrors have UV enhanced aluminum coating. They are supposed to have 89% and 85% reflectivity for the UV and IR ranges, respectively (Edmund Optics, 2020). The measurement results show that the mirror reflectivity in the UV channels is lower than our expectations, which might be the result of scattering caused by high surface roughness (∼3 nm) (Schmitt, 1990).

8.2 Relative pointing characterization

Total throughput measurements and characterization of optical aberrations are common optical calibration tasks for telescopes (Park et al., 2012), but relative pointing measurements are also necessary for multi-channel telescopes. Two observation targets of the MATS satellite, noctilucent clouds and O_2 atmospheric band dayglow/nightglow, are located at different altitudes. For this reason, the image centers of UV and IR channels are different by design: The four IR channels should share their field of view, and so should the two UV channels.

There are relative pointing errors resulting from mechanical fabrication errors, filter or beam splitter misalignments, etc. Relative pointing measurements enable end-users to know and correct the pointing errors of each channel so that the proper targets can be observed. The relative pointing between the channels was measured by taking point source images that were generated by the 100 μm pinhole and the Inframet CDT11100HR collimator (Figure 7.1) (INFRAMET, 2020). This optical test setup was also used for imaging performance measurements.

Figure 8.2 displays the relative pointing of the IR and UV channels. Black crosses indicate the pointing reference of the satellite that is also considered as the optical axis of the telescope. Red and blue areas show targets for each channel. The field of view for each CCD is overlaid with colored solid lines.

There are tight margins in the vertical direction, especially for UV channels. The IR channels seem to have good alignments while covering the target in all four channels. The maximum separations among IR channels are 0.2° in vertical and 0.4° in horizontal. UV channels are misaligned to the vertical direction by 0.5° while they horizontally misaligned by 0.1°. Even though UV fields are largely separated, they still properly cover their target.

The observed images should be aligned by using relative pointing offset values listed in Table 8.2. The pointing reference (0.00, 0.00) corresponds to black crosses in Figure 8.2. Due to different altitudes of UV and IR targets (70 - 90 km for UV, and 75 - 110 km for IR), y-offsets of each source deviate from 0.00 pixels.

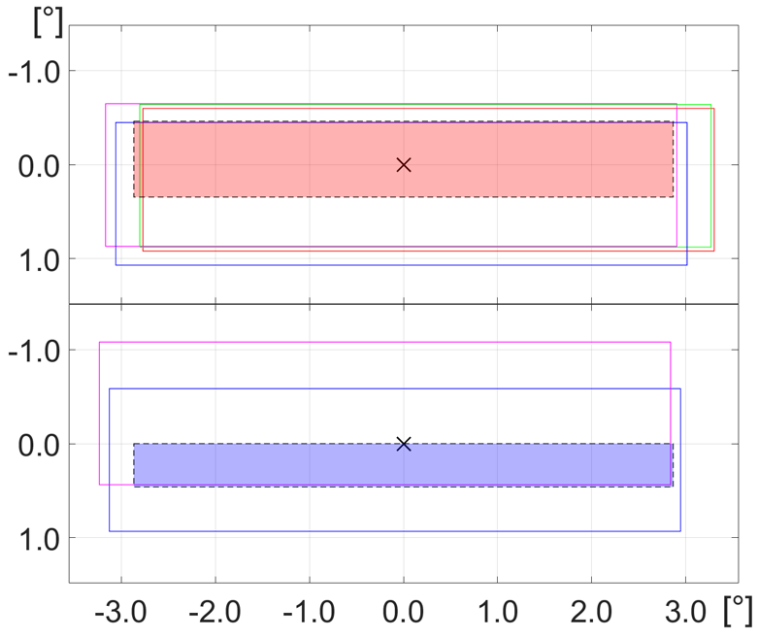

Figure 8.2: Relative pointing of IR (top) and UV (bottom) channels. Field of view of IR1 (red), IR2 (magenta), IR3 (green), IR4 (blue), UV1 (blue), and UV2 (magenta) are illustrated with solid lines.

8.3 Distortion

The MATS satellite will generate 3D cube data by using the tomography technique, which combines a bunch of images. Each frame would not match together if distortion exists, and it creates large errors in the tomography. Distortion is measured with the point source and a distortion target (INFRAMET, 2020). In this test, we accurately rotated the telescope into a specific angle, and compared the rotation angle with the incident angle of the beam derived from the image location at the sensor.

As the result shown in Figure 8.3, there is pincushion-like distortion with more aberrations to the upper-left and the lower-right corners than to the other corners. The maximum distortions to vertical and horizontal directions are 2.57% and 3.70%, respectively. Distortions by design are 0.08% and 2.83% in vertical and horizontal directions.

Table 8.2: Relative pointing offsets of UV and IR targets. Offset values are relative to the pointing reference.

Target / Channel	x-offset (pix)[a]	y-offset (pix)
UV source	0.00	77.60
UV1	-30.72	58.54
UV2	-66.56	-108.38
IR source	0.00	-19.40
IR1	89.79	54.47
IR2	-44.02	37.64
IR3	78.58	40.31
IR4	-7.49	104.92

[a] The pixel size is 13.5 μm square that is for the E2V CCD42-10 CCD.

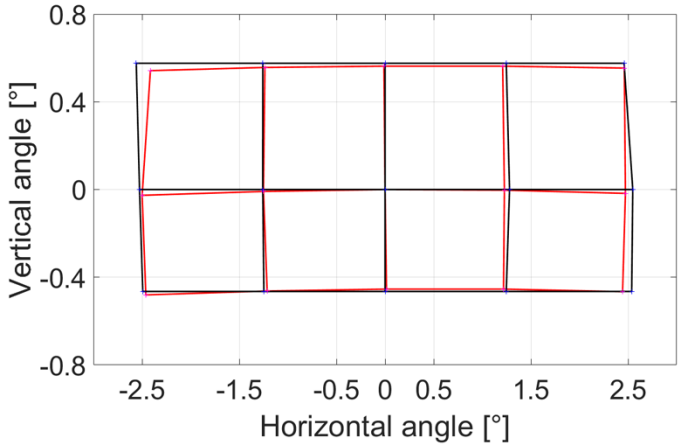

Figure 8.3: Distortion measurements of the limb telescope. Black solid lines indicate the distortion grid by design, while red solid lines represent the measured distortion grid.

Measured distortion can be generated by mirror surface figure errors that mainly come from the fabrication process and by filter bending cased by assembly stress. Note that the background of distortion is already introduced in Section 3.4.5.

Chapter 9

Optomechanical Structures

Optical system performance is primarily determined by optical design and optical component quality but also stability and accuracy of optomechanical structures are significant factors. The key concept of optomechanics is to stably hold optical components in the right position. A few methods to design optomechanical structure for off-axis reflective systems will be introduced in this chapter.

Fabricated optical mirrors (or lens) and optomechanics are not always perfect so alignment mechanisms are required on both optical and optomechanical sides. The detailed alignment mechanism is already introduced in Chapter 6. On the other hand, optomechanics and other test setups such as a collimator and a camera module should be aligned for accurate performance tests. Since off-axis systems are not symmetrical to the optical axis, alignment of optomechanics and the test setups is a more challenging job. Figure 9.1 represents some optomechanical features that help to align optomechanics to the test setups. The surface that is indicating by the blue arrow is parallel to the optical axis of the incident light. The pink arrows point mechanical surfaces that are aligned with the optical axis of the system, which can be useful for optical tests. The camera mount (blue) and optomechanics are facing together so they have a better alignment for the camera.

The mirror mounting to optomechanical structure is a careful task. Some supports or

Contents of this chapter are published in the publication [2], and [3].

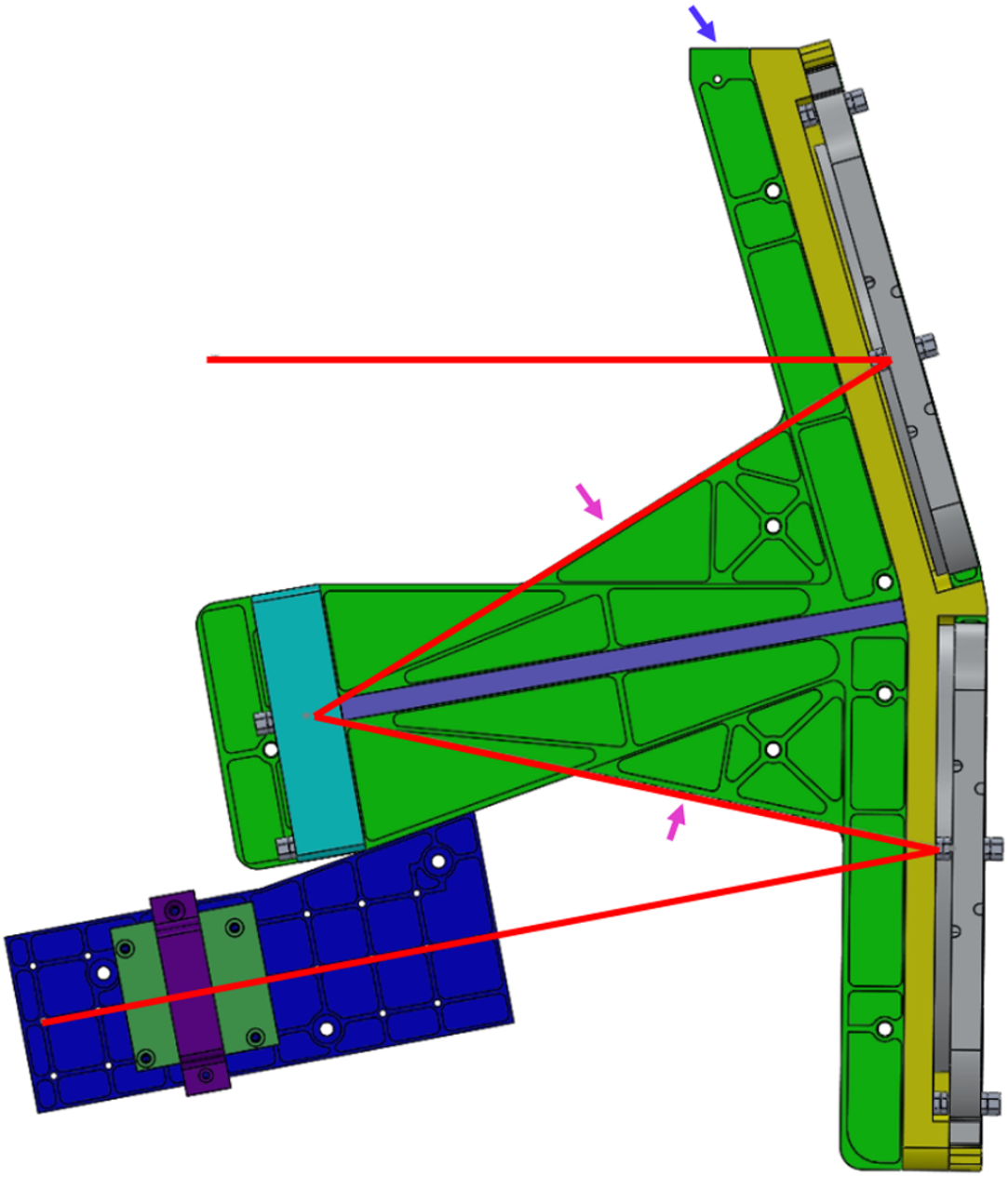

Figure 9.1: Optomechanical structure design of LAF-TMS. Red solid lines represent the optical axis ray of the system.

holders assist in the accurate mounting process. Figure 9.2 shows the secondary mirror mounting process of LAF-TMS. The Mirror mounting support screws onto a rear side of the mirror and the holder slides along with the pins to optomechanics. This method prevents accidents and helps accurately positioning the mirror.

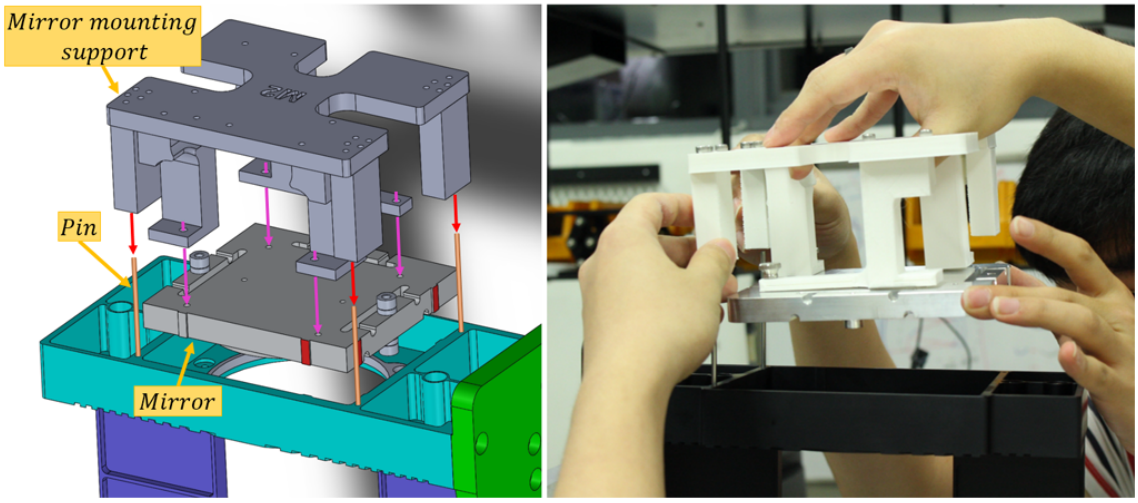

Figure 9.2: Accurate mirror mounting mechanism (left) and a picture of mounting the mirror (right).

Optomechanical structure of LAF-TMS adapts the L-bracket for positioning the mirror (see Figure 6.3). The key to optical alignments is to decide alignment references. The secondary mirror surface of LAF-TMS is the aperture stop of the system so the contact points on the side of the mirror are selected as the alignment references for x- and y-axes. Therefore, there is no L-bracket for the secondary mirror to align it (the left panel in Figure 9.3) that is different to the primary and the tertiary mirrors.

Mechanical surfaces of optomechanical structures generally anti-reflecting black anodized to reduce internal reflection of the stray light. Groove features on the specific mechanical surface can minimize the stray light (the right panel in Figure 9.3).

A prototype of optical systems has potential risks to be changed optical or optomechanical designs. Modular design separates optomechanical structure into a few modules

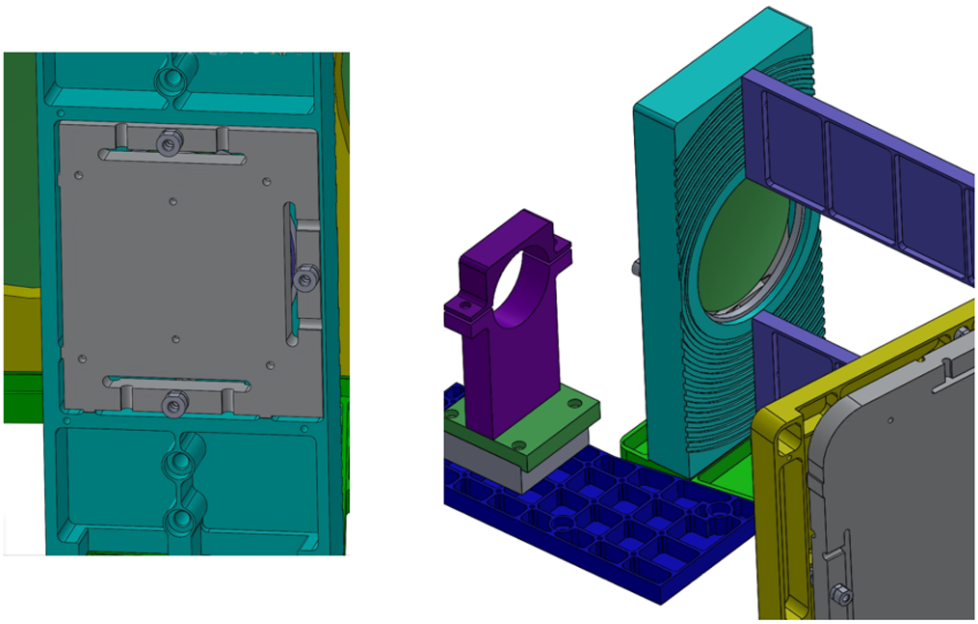

Figure 9.3: Reference points on the secondary mirror of LAF-TMS (left) and groove features on the mirror holder (right).

thus each module is replaceable to the different model and is fabricated within higher accuracy than the one body structure (Figure 9.4). But this design is possibly distorted when assembling modules. For this reason, the final model is recommended to be fabricated into the one body structure if it is fabricable within a tolerance range.

Light-weighted features for LAF-TMS are presented in Figure 9.4. Weight of the optical system is extremely important, especially for satellites. Light-weight mirrors and optomechanical structures are generally adapted for the space telescope. Honeycomb and isogrid designs reduce the weight of optics and optomechanics to 60 - 80%.

Another optomechanical feature that useful for the optical experiment kit is an optical table style design. It contains an array of holes and taps for various optical tests in different configurations (Figure 9.5). This feature is also adapted for the camera or telescope mounting that requires position adjustments.

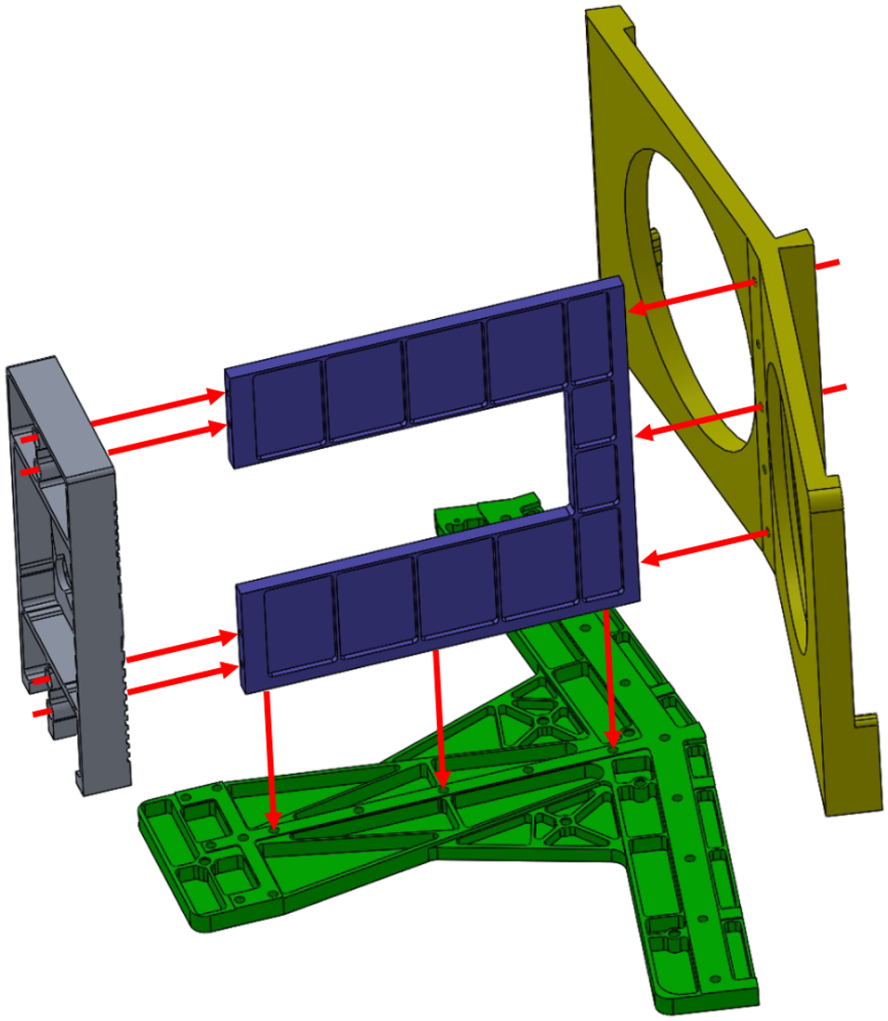

Figure 9.4: The modular design concept for the prototype telescope.

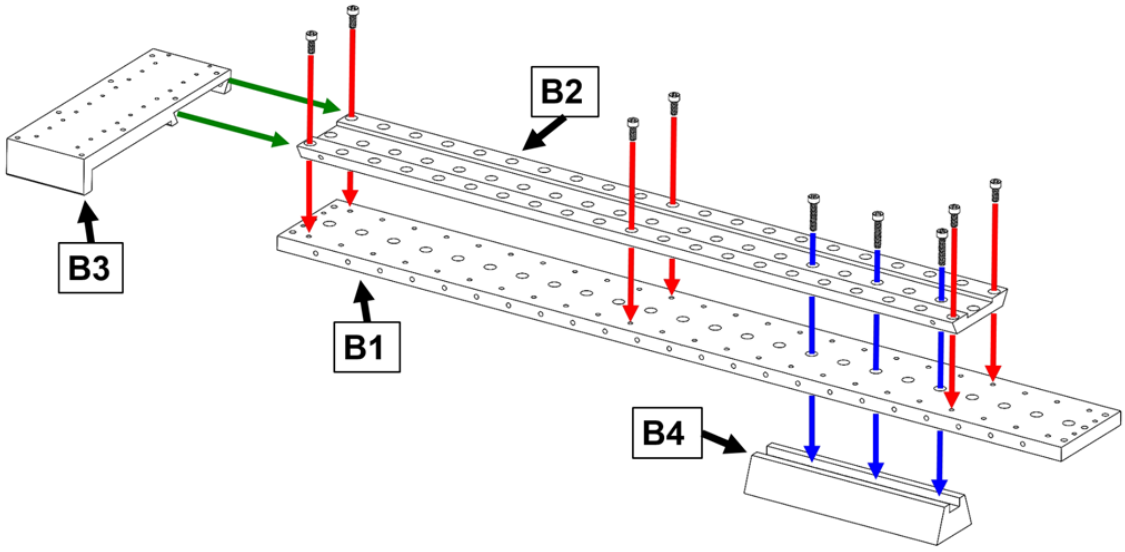

Figure 9.5: An optical table style design for optical experiments and measurements.

Chapter 10

Finite Element Analysis

Designed mechanical structures need to be confirmed in their stability, variance, and strength to various environments such as temperature, vibration, load, shock, assembly stress, etc. Finite element analysis (FEA) simulates the mechanical design to predict real-world behaviors by using a subdivided 3D model into small elements called mesh. Accuracy of the simulation relies on the number of the mesh but more mesh requires more simulation time. In this chapter, we will introduce some basic parameters and methods for FEA simulations with examples of LAF-TMS cases.

10.1 Safety factor and margin of safety

Safety factor is an indicative factor of the level of the confidence in accuracy of the criterion. In most cases, yield or ultimate stress from the FEA simulations becomes the criterion. Figure 10.1 illustrates how safety factor provides its confidence in accuracy of yield (or ultimate) stress. Based on European Cooperation for Space Standardisation (ECSS) standards, safety factor is 1.1 when using yield stress, and 1.25 for ultimate stress (ESTEC, 2008a,b, 2009, 2014).

Finite element analysis provides the maximum von Mises stress, which derives Margin

Contents of this chapter are published in the publication [3].

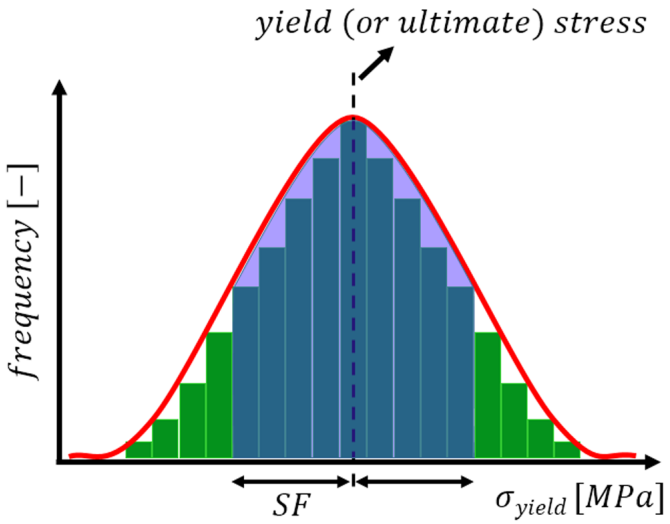

Figure 10.1: An illustration for safety factor (SF) to yield (σ_{yield}) or ultimate ($\sigma_{ultimate}$) stress.

of Safety (MoS) with equation (10.1.1) (Jeong et al., 2018),

$$MoS(\%) = \left[\left(\frac{\sigma_{yield}}{\sigma_{max} \times SF}\right) - 1\right] \times 100\%. \tag{10.1.1}$$

In equation (10.1.1), σ_{yield} is the yield stress of the material, and σ_{max} is the maximum von Mises stress, which is the result of the FEA simulation. The mechanical structure is safe for the corresponding load if MoS is positive.

10.2 Vibration analysis

Satellites are exposed to various vibrational environments during critical launch events, such as left-off, wind and gust, stage separations, etc. The stability of the satellite system needs to be confirmed in vibration environments. Vibration environments are simulated using three analyses: quasi-static, harmonic, and random analysis. Modal analysis is also performed to calculate the system's natural frequency and mode shape (Abdelal et al., 2013).

10.2.1 Quasi-static analysis

Quasi-static analysis applies a quasi-static load, meaning that the load is applied very slowly so the inertial force is negligible. Technically static and qusi-staitic analysis are different in the presence of the inertial force, but practically those analyses can be performed in the same way.

Mass acceleration curve (MAC) has been adopted over many years for quasi-static analysis (Figure 10.2),

$$MAC(G) = \frac{G_0}{\sqrt{m/M + (\xi_s + \xi_l)^2}} e^{-\alpha/\tan\alpha}, \tag{10.2.1}$$

$$\alpha = \tan^{-1}\frac{\sqrt{m/M}}{\xi_s + \xi_l}, \qquad G_0 = A_0 e^{\xi_s + \xi_l}. \tag{10.2.2}$$

where, A_0 is the initial acceleration, m and M are the effective mass of a payload and a launch vehicle, and ξ_s and ξ_l are the damping of the payload and the launch vehicle modes. The sum $\xi_s + \xi_l$ is the more commonly used for a damping parameter, instead of using each damping separately.

Because it gives bound accelerations for each effective mass of the payload, quasi-static analysis with MAC is considered as the worst-case analysis (Trubert, 1989). This analysis can be adapted to a payload mass of less than 500 kg.

We used Space Shuttle and Inertial Upper Stage (STS/IUS) MAC to calculate quasi-static accelerations to LAF-TMS (Chang, 2001). The total mass of LAF-TMS is 9.47 kg, corresponding to 37.42-G, so we took the acceleration value of 40-G for all three axes. We fixed seven mounting positions and put accelerations on the same locations (red circles in Figure 10.3). Quadratic tetrahedral 3D solid mesh elements were applied. The total number of nodes and elements are 144,404 and 79,128, respectively. All contact points and connections of parts are considered to be bonded.

The simulation is performed in three separate acceleration axes, x-, y-, and z-accelerations. Figure 10.4 shows the simulation results with the color scale representing von Mises stress.

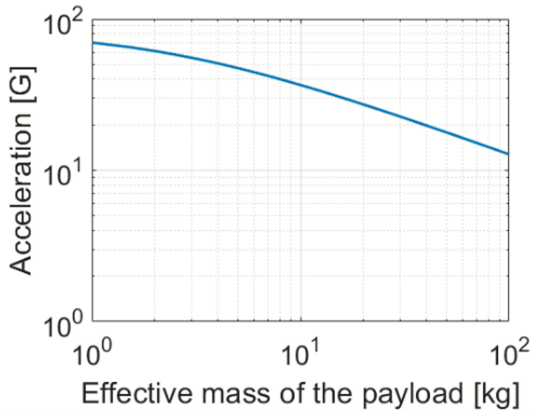

Figure 10.2: STS/IUS Mass acceleration curve that corresponds to $G_0 = 1.60$ G, $\xi_s + \xi_l = 0.02$, and $M = 6000$ kg.

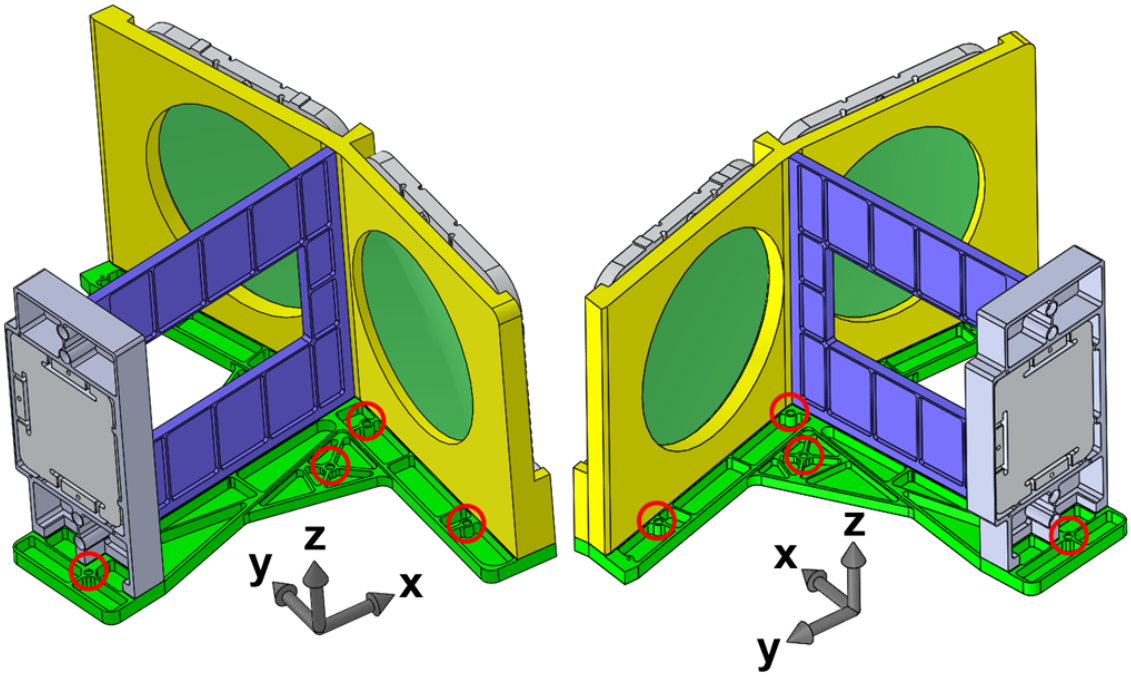

Figure 10.3: Optomechanical design of LAF-TMS. Red circles are mounting positions of the base plate.

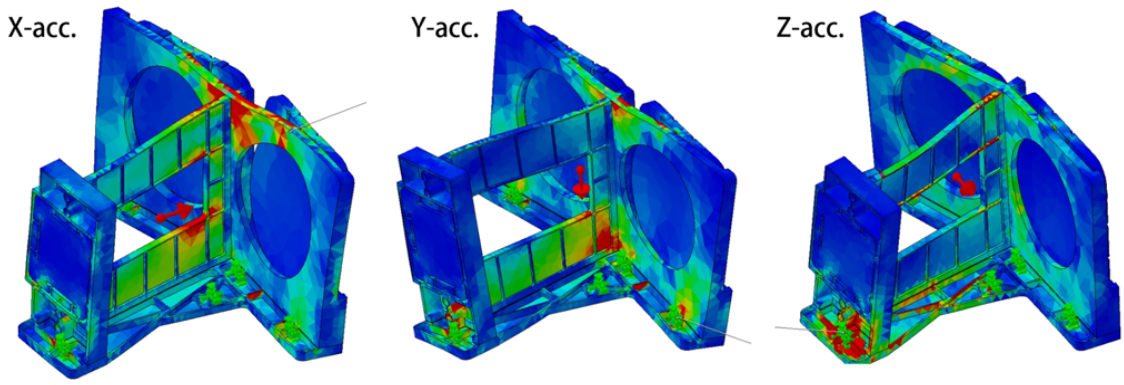

Figure 10.4: Quasi-static analysis results in x-axis (left), y-axis (middle), and z-axis (right) accelerations.

The maximum von Mises stress, which derives Margin of Safety (MoS) with Equation 10.1.1, implies stability of the system. We used aluminum alloy 6061-T6 for the entire system that has the yield stress of 275 MPa (Kaufman, 2000).

Table 10.1: Quasi-static loads and stress simulation results of LAF-TMS

Load-axis	Quasi-static load (G)	σ_{max} (MPa)	MoS (%)
x	40	78.30	220
y	40	152.70	64
z	40	34.86	620

Table 10.1 shows input quasi-static load, maximum von Mises stress, and MoS for each load axis. For all axes, LAF-TMS has positive MoS, indicating high stability of the telescope that overcomes the worst-case quasi-static environments.

10.2.2 Modal analysis

Natural frequency and mode shape of mechanical structures are examined with modal analysis. This analysis is the study of dynamic properties of the system in the frequency domain and helps optomechanics avoid exposure to vibration resonance (Ramesha et al., 2015).

Natural frequency is determined when structure shape, material, boundary conditions, etc. are decided. The modal analysis results of LAF-TMS are summarized in Table 10.2 and Figure 10.5.

Table 10.2: Natural frequency of LAF-TMS

Frequency mode	Natural frequency (Hz)
1	121.57
2	157.88
3	202.09
4	418.97
5	455.50

The fundamental frequency (frequency mode 1) is 121.57 Hz. Mode shape of frequency mode 1 shows that M2 might tilt in harsh vibration environments (Figure 10.5). We selected nodes for each vibration mode that specialize in measuring responses from harmonic and random vibrations.

10.2.3 Harmonic and random analysis

Harmonic and random analysis determine responses to sinusoidal and random loads, so it verifies whether the satellite system can survive these environments or not. Here, we input vibration loads of the Souyz-2/Freget launch system (see, Figure 10.6 and Table 10.3) for harmonic and random analysis of LAF-TMS. These input vibration loads imply the envelopes of input vibration loads in the real world. The damping ratio of 0.02 modal damping is set for both analyses. Simulations are performed in x-, y-, and z-acceleration axes. We selected nodes for each vibration mode that specialize in measuring responses from harmonic and random vibrations

Figure 10.7 displays response curves from harmonic and random analysis. Power spectral density (PSD) is used to characterize simulated random vibration signals. Each acceleration axis has five response curves that correspond to each of the response nodes (Figure 10.5).

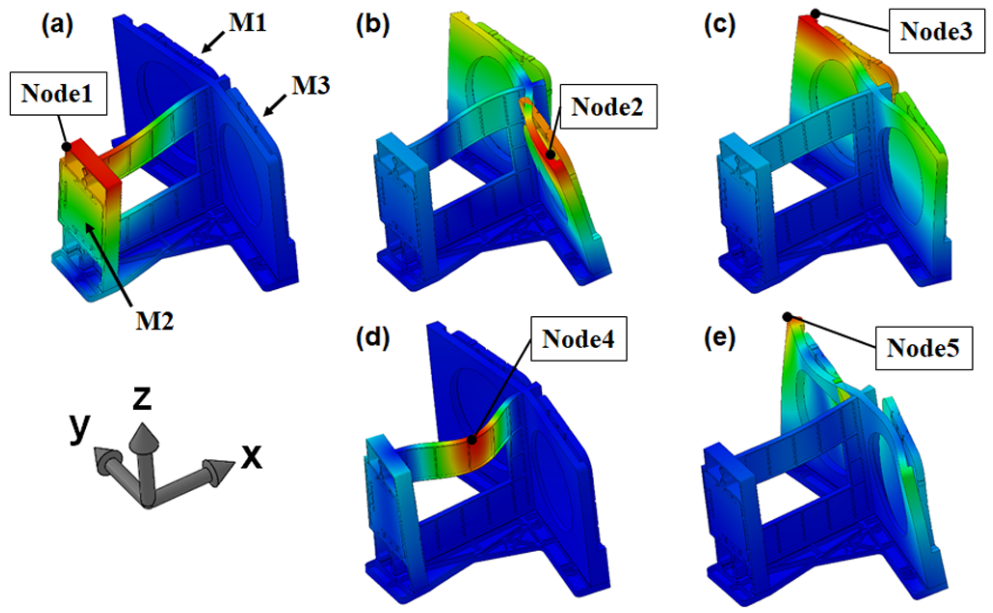

Figure 10.5: Vibrational mode shapes, and harmonic and random vibration response nodes of LAF-TMS. Mechanical deformations in frequency (a) mode 1, (b) mode 2, (c) mode 3, (d) mode 4, and (e) mode 5 are illustrated.

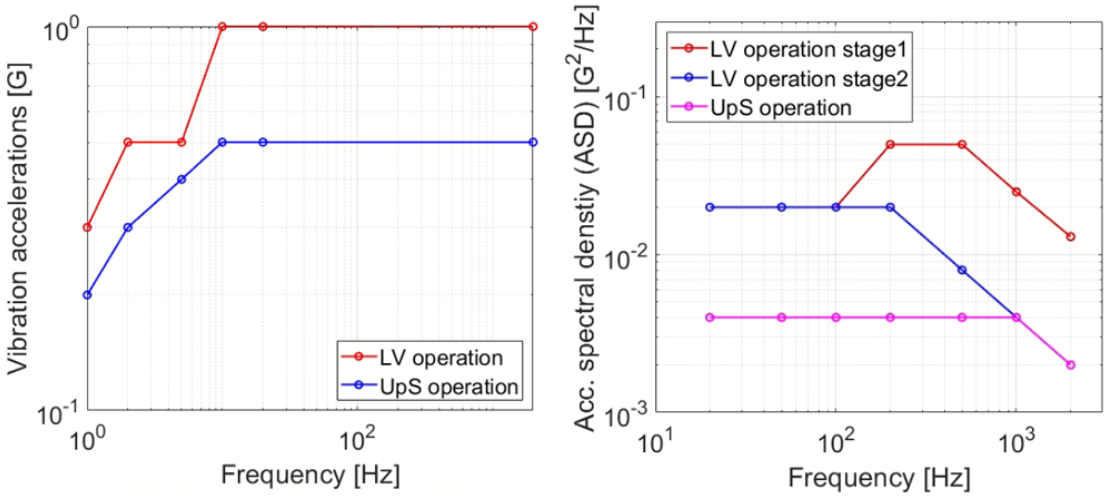

Figure 10.6: Harmonic and random vibration qualification levels of the Souyz-2/Freget launch system.

Table 10.3: Harmonic and random vibration qualification levels of the Souyz-2/Freget launch system

Harmonic vibration	Frequency sub-range (Hz)	1 - 2		2 - 5		5 - 10		10 - 2000
	Vibration accelerations (G) (G = 9.81 m/s^2)	0.3 - 0.5		0.5		0.5 - 1.0		1.0
Random vibration	Frequency sub-range (Hz)	20 - 50	50 - 100	100 - 200	200 - 500	500 - 1000	1000 - 2000	Acceleration RMS (G)
	Acceleration spectral density (ASD) (G^2/Hz)	0.02	0.02	0.02 - 0.05	0.05	0.05 - 0.025	0.025 - 0.013	7.42

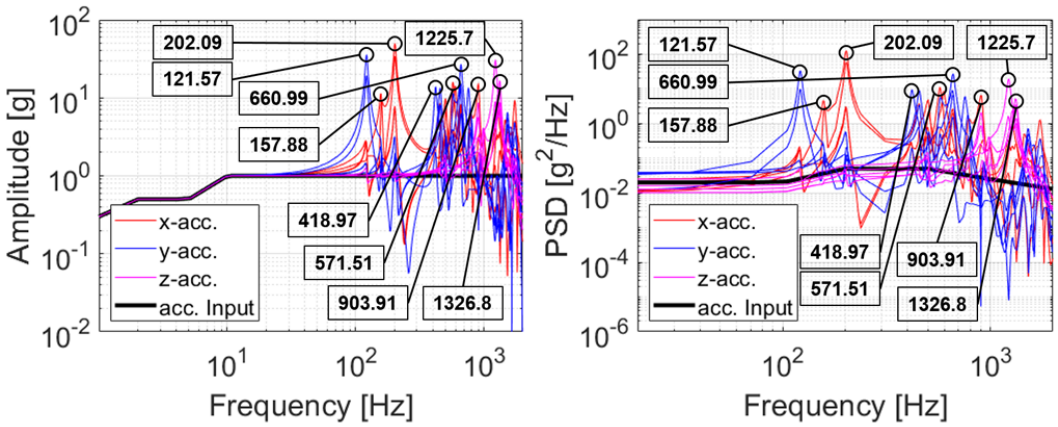

Figure 10.7: Response curves from harmonic (left) and random (right) analysis.

We identified eight dominant resonance frequencies, which are 121.57 Hz (mode 1), 157.88 Hz (mode 2), 202.09 Hz (mode 3), 418.97 Hz (mode 4), 571.51 Hz (mode 7), 660.99 Hz (mode 9), 903.91 Hz (mode 14), 1225.70 Hz (mode 18) and 1326.80 Hz (mode 20). Von Mises stress is calculated in these frequencies and the corresponding acceleration axes.

Table 10.4 lists the dominant resonance frequencies. The maximum von Mises stress and MoS of each analysis are also presented. MoSs in all frequencies for both analyses are

Table 10.4: The maximum von Mises stress at nine dominant resonance frequencies from harmonic and random analysis

Resonance frequency (acceleration axis)	Harmonic analysis		Random analysis	
	σ_{max} (MPa)	MoS (%)	σ_{max} (MPa)	MoS (%)
121.57 (y)	94.54	165	173.14	45
157.88 (x)	14.31	1653	37.64	567
202.09 (x)	56.09	347	166.94	50
418.97 (y)	2.27	10968	9.67	2496
571.51 (x)	2.77	8961	14.42	1640
660.99 (y)	12.17	1962	50.26	399
903.91 (x)	2.90	8552	16.11	1458
1225.70 (z)	6.80	3591	27.41	815
1326.80 (z)	7.10	3433	26.89	833

positive, indicating that LAF-TMS is safe from harmonic and random vibration environments of the launch system.

10.3 Bolt connection analysis

Mechanical stress from a mirror mounting to optomechanics distorts the optical surface. Optimizations of the mirror or the mirror holder design using FEA in bolt connections reduce the stress. Figure 10.8 shows LAF-TMS mirror parameters, width (w) and length (l) of the thermal expansion slot and the mirror height (h), that are optimized to minimize a mirror surface deformation by the assembly stress. The bolt connection analysis is performed by applying assembly torque of screws that are referenced from Elliott (2012) (Table 10.5). Since the LAF-TMS mirrors are mounted on optomechanics with M4 screws, $20kgfcm$ torque has been adapted as an external load for the LAF-TMS mirror simulation. For the bolt connection, the stainless steel (ferritic) bolt, the head diameter of 6.15 mm, and the nominal shank diameter of 4.1 mm are applied. The L-bracket supports the LAF-TMS mirror so the bracket and mirror holders are fixed in the simulation. All mechanical

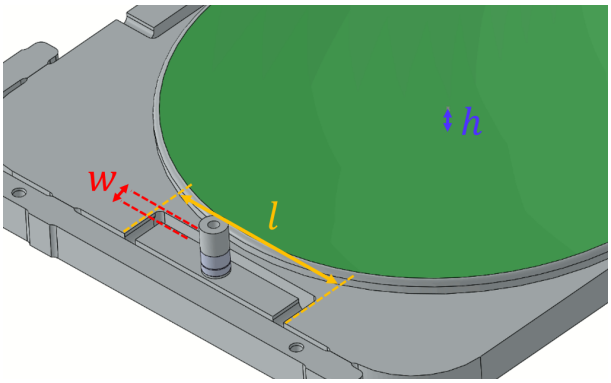

Figure 10.8: LAF-TMS mirror optimization parameters for the bolt connection analysis.

Table 10.5: ESA mechanical torque values (Elliott, 2012)

Size (UNC)	Size (mm)	inf·lb	ozf·in	N·m	kgf·cm
0-80 (UNF)	1.52	0.8	12.8	0.09	0.92
2-56	2.18	2.3	36.8	0.26	2.65
4-40	2.84	4.9	78.4	0.55	5.61
6-32	3.50	9.2	147.2	1.04	10.61
8-32	4.31	17	272	1.92	19.58
10-32 (UNF)	4.82	28	448	3.16	32.23
1/4-20	6.35	58	928	6.55	66.81

components are no penetration contacted with the coefficient of friction to 0.3.

Figure 10.9 illustrates bolt connection analysis results in von Mises stress and displacement for the LAF-TMS mirror. The maximum von Mises stress is 134.2 MPa that corresponds to MoS of 86.29 (from Equation 10.1.1). The mirror surface RMS deformation is derived from the displacement plot (the right panel in Figure 10.9). The plot (colors) indicates displacement of the whole mirror, and a standard deviation of the mirror surface displacement is calculated in order to extract the surface RMS errors that is 47.4 nm in this case. The mean displacement of the whole mirror is 7.49 μm that is required to be considered as a mirror displacement error from the nominal position.

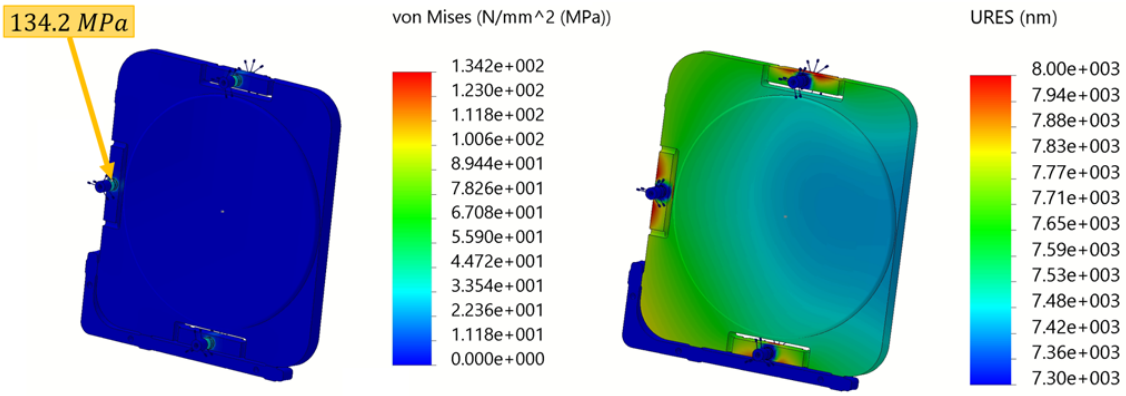

Figure 10.9: Bolt connection analysis results in von Mises stress (left) and displacement (right) for the LAF-TMS mirror. The maximum stress by bolt connections is 134.2 MPa.

Chapter 11

Stray Light Analysis and Baffle Design

Stray light analysis and effective baffle design are necessary to suppress unwanted light that degrades the image quality. Stray light is extraneous, unwanted light which is detected by the sensor reflection from mechanical structures or scattering from optical components. Stray light presents itself as noise in the image, reducing the signal to noise ratio (SNR).

The baffle design of on-axis reflective optical systems, such as Cassegrain, and Ritchey-Chrétien telescopes is a well-defined process described by mathematical models. An iterative method is needed to design proper baffle systems (Ho & Chang, 2009; Kumar et al., 2013; Song et al., 2002). For portable optical device, stray light suppression is critical and even more important than it is for instruments operated indoors, as there are more potential stray light sources outdoors.

Initial baffle design starts with the analysis of stray light boundaries. Figure 11.1 illustrates the boundary of stray light suitable for classical two mirror systems, e.g. Newtonian, Cassegrain, and Gregorian telescopes. The plate baffles behind the primary and secondary mirrors are designed to effectively suppress critical stray light paths that can directly illuminate the detector. These critical stray light paths are of particular importance for the

Contents of this chapter are published in the publication [2].

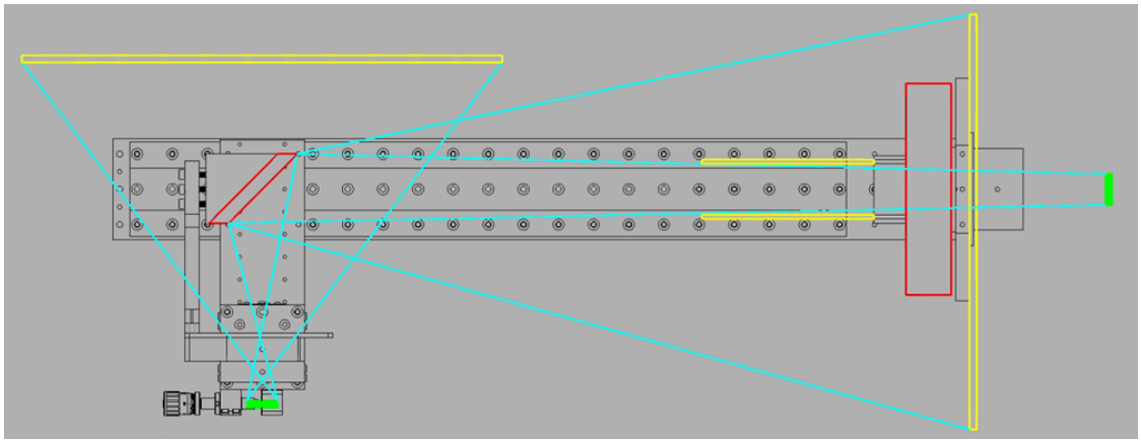

Figure 11.1: Boundaries of stray lights (cyan) incident to the TRT Kit detectors (green). Baffles and mirrors are indicated in yellow and red.

Newtonian system, which is susceptible to stray light from potential sources because of the location of the focal plane.

Figure 11.2 demonstrates 3D modeling of designed baffle structures based on the analysis of boundary paths of stray light. Baffle surfaces are black-anodized in most cases, but other dark surfaces can be used. Vantablack is one of the extremely dark material with reflectivity of 0.2 - 0.4% in visible that is coated on baffles for satellites.

Stray light analysis is completed with LightTools software (Synopsys Inc.) after initial baffle was designed (Figure 11.3). In the simulation, a 6500 K black body source was used to illuminate the TRT Kit optical system, approximating the spectral distribution of daylight. Assuming black-anodized diffusive surfaces, baffles and optomechanical structures scatter light with 1% and 5% Lambertian reflectance, respectively. Incidence angles of simulated stray light paths span 0° - 180° for all systems.

The amount of stray light suppression can be defined with the point source transmittance (PST):

$$PST(\theta, \lambda_0) = \frac{L_{\mathrm{D}}(\theta, \lambda_0)}{L_{\mathrm{A}}(\theta, \lambda_0)} \tag{11.0.1}$$

,where $L_{\mathrm{D}}(\theta,\lambda_0)$ is spectral radiance on the detector, and $L_{\mathrm{A}}(\theta,\lambda_0)$ is spectral radiance on the entrance aperture. The PST represents how much stray light can be suppressed by

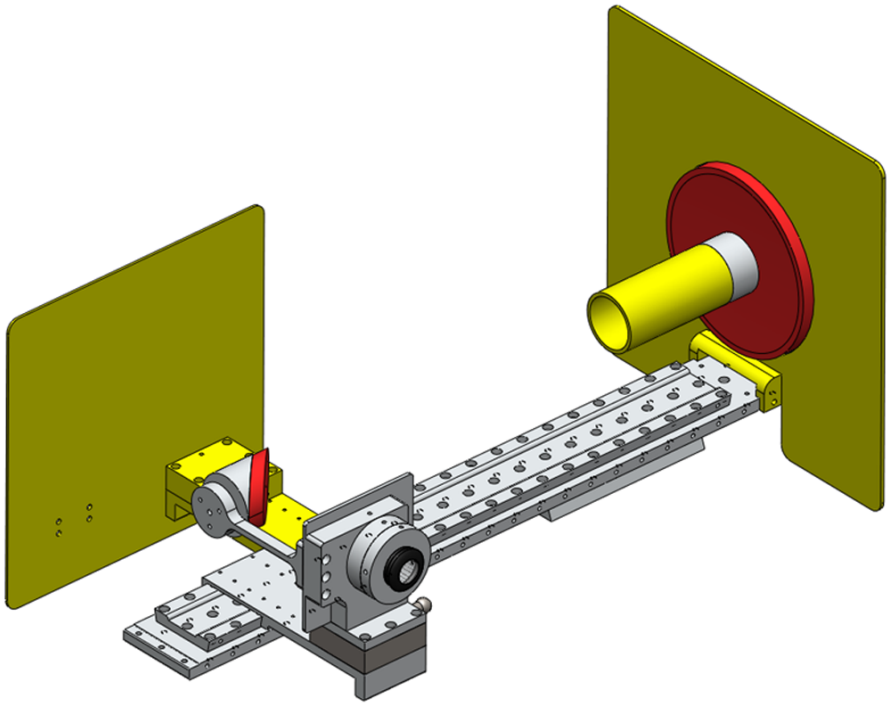

Figure 11.2: The TRT Kit with baffle structures. Yellow colors represent the baffles of the telescope.

the baffle structure as a function of the incidence angle. Figure 11.4 presents results from stray light analysis for the TRT Kit. Blue dots represent the PST with baffles, and red dots indicate the PST without baffles.

Baffles suppress 75% - 95% of stray light from all incidence angles (0° to 180°). The PST reaches a minimum of around 10^{-8} with baffles. Note that some of the sharp drops in PST near the 20° to 90° incidence angles for the Gregorian system are a result of under-sampling.

Compared to the other systems, the detector is most exposed to stray light without the baffle in the Newtonian system. Incoming stray light from the specific angle (95° - 118°, and around 170°) causes substantial degradation of image quality without the use of baffles. Suppression of stray light for incidence angles between 40° - 180° is particularly

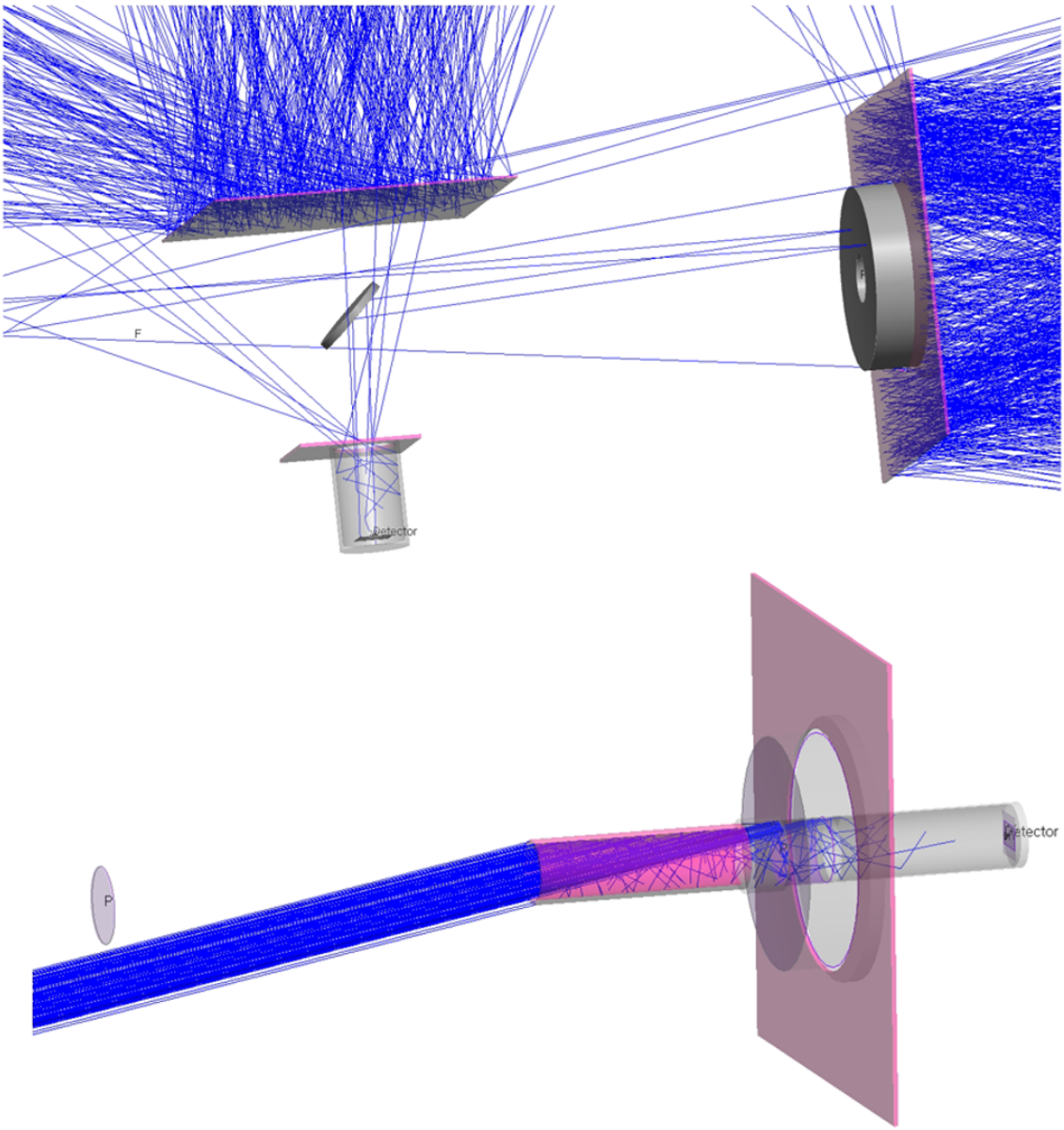

Figure 11.3: Stray light analyses of the Newtonian telescope (top), and Cassegrain and Gregorian telescopes (bottom).

significant for the Newtonian system with the addition of baffles. 90% to 99.99% of stray light is suppressed in this region.

Stray light measurements require higher than an ISO class 5 cleanroom to suppress

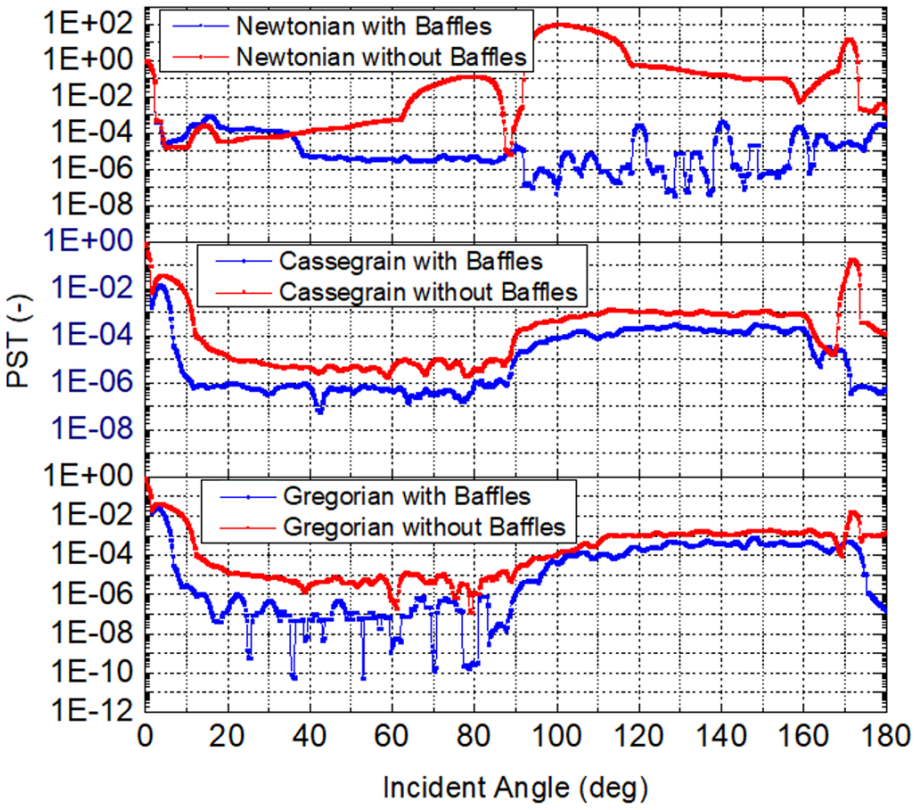

Figure 11.4: Stray light analysis results of (a) Newtonian, (b) Cassegrain, and (c) Gregorian systems. Blue dots represent the PST with baffles, and red dots indicate the PST without baffles.

scattering of the incident light by dust in the air. As the light that reaches the detector after reflection on baffle surfaces is the dim light, the light source should have strong power like a 1kw xenon lamp.

Chapter 12

Summary

This thesis summarizes the key steps of optical system developments for astronomical telescopes. It includes tolerance analysis, optical alignments, performance tests, characterizations, design methods of optomechanical structures, finite elements analysis, and stray light analysis and baffle design. Geometrical optics and optical types of reflecting telescopes are introduced for backgrounds of the optical design.

Linear astigmatism is a second order aberration that only exists in off-axis systems, so it is more critical to optical performance than third order aberrations such as coma, third order astigmatism, spherical aberrations, etc. Linear-astigmatism-free off-axis systems avoid scattering, diffraction, and obscuration by the secondary mirror, and provide high optical performance over wide field of view by eliminating linear astigmatism. A combination of linear-astigmatism-free off-axis system and freeform mirrors not only eliminates linear astigmatism but reduces third order aberrations without any correcting lenses.

Tolerance analysis is performed into two steps, sensitivity analysis and Monte Carlo simulation. Sensitivity analysis explores an individual tolerance budget of each parameter. Monte Carlo simulation assesses the system performance by implementing a statistical analysis. Feasibility of the optical system can be evaluated through the comparison of sensitivity analysis and Monte Carlo simulation, and fabrication and alignment errors.

Three-point laser and 3-2-1 position alignments are introduced for optical alignment

methods. The position of the point source image or other targets at the focal plane directly reflects the system alignment errors. The existence of specific aberrations measured by MTF measurements, point source tests, or field tests implies optical performance of the system and also its alignment errors.

Characterizations of the optical system are necessary for scientific research. Total throughput, pointing characterization, and distortion measurement are introduced in this thesis, which are especially critical to multi-channel optical systems, but there are more ways to characterize the optical system.

Optomechanical structure supports the optical components and enables the components to locate in the correct position. They should be analyzed by external forces through finite element analysis, and it is more important to satellite systems. Baffles suppress the stray light, which degrades the image contrast, so stray light analysis and baffle design are essential for high signal to noise images.

The telescope system development is an interdisciplinary study of optics, mechanics, electronics, astronomy, etc. Therefore, understanding in various fields is important to successfully build a complex system.

Bibliography

Abdelal, G. F., Abuelfoutouh, N., & Gad, A. H. 2013, in Finite Element Analysis for Satellite Structures: Applications to their design, manufacture and testing (Springer), 83–202

Bauman, B. J., & Schneider, M. D. 2018, Optics Express, 26, 13819

Birney, D. S., Gonzalez, G., & Oesper, D. 2005, in Observational astronomy (Cambridge University Press), 170–182

Blank, R., Anglin, S., Beletic, J. W., et al. 2012, Proc. SPIE, 8453, 845310

Born, M., & Wolf, E. 1999, in Principles of Optics: Electromagnetic Theory of Propagation, Interference and Diffraction of Light (Cambridge University Press), 142–227

Burge, J. H., Benjamin, S., Dubin, M., et al. 2010, Proc. SPIE, 7733, 77331J

Chang, K. Y. 2001, ESASP, 468, 295

Chang, S. 2013, Proc. SPIE, 8860, 88600U

—. 2015, Journal of the Optical Society of America A, 32, 852

—. 2016, Proc. SPIE, 9948, 99481B

—. 2019, Optical Design and Fabrication (Freeform, OFT), FM2B, FM2B.6

Chang, S., & Aluizio Prata, J. 2005, Journal of the Optical Society of America A, 22, 2454

Chang, S., Lee, J. H., Kim, S. P., et al. 2006, Applied Optics, 45, 484

Chen, C.-W., & Chen, C.-R. 2015, Proc. SPIE, 9602, 96020P

Edmund Optics. 2011, Distortion, https://www.edmundoptics.com

—. 2020, Metallic mirror coatings, https://www.edmundoptics.com

Elliott, B. 2012, in ESA mechanical torque value (THEMIS ESA), 1–1

ESTEC. 2008a, Space engineering Threaded fasteners handbook, ECSS-E-ST-32C Rev.1

—. 2008b, Space engineering Threaded fasteners handbook, ECSS-E-ST-32-03C

—. 2009, Space engineering Threaded fasteners handbook, ECSS-E-ST-32-10C Rev.1

—. 2014, Space engineering Threaded fasteners handbook, ECSS-E-ST-32-08C Rev.1

Fujita, H., Tsai, D.-Y., Itoh, T., et al. 1992, IEEE Transactions on medical imaging, 11, 34

Funck, M. C., & Loosen, P. 2010, Proc. SPIE, 7652, 76521M

Hagen, N. 2014, Optical Engineering, 53, 123107

Harvey, J. E. 2013, Optical Engineering, 52, 073110

Ho, C.-F., & Chang, S.-T. 2009, Proc. SPIE, 7506, 75061S

INFRAMET. 2020, INFRAMET, https://www.inframet.com

Ingers, J., & Breidne, M. 1989, Proc. SPIE, 1029, 111

Jeong, G., Kim, J. H., Chae, J., & Jeon, H.-Y. 2018, Journal of Aerospace System Engineering, 12, 47

Judy, P. F. 1976, Medical Physics, 3, 233

Kaufman, J. G. 2000, in Introduction to Aluminum Alloys and Tempers (ASM International), 39–76

Kim, S., Pak, S., Chang, S., et al. 2010, J. Korean Astron. Soc., 43, 169

Kumar, M. S., Narayanamurthy, C. S., & Kumar, A. S. K. 2013, Applied Optics, 52, 1240

Kuś, A. 2017, Applied Optics, 56, 9247

Lee, H., Hill, G. J., Marshall, J. L., Vattiat, B. L., & DePoy, D. L. 2010, Proc. SPIE, 7735, 77353X

Mahajan, V. N. 1982, J.Opt.Soc.Am., 72, 1258

—. 2011, in Optical Imaging and Aberrations, Part II. Wave Diffraction Optics, Second Edition (SPIE), 1–78

Michalet, X., & Weiss, S. 2006, Proc. Natl. Acad. Sci. USA, 103, 4797

Padgett, R., & Kotre, C. J. 2006, Radiation Protection Dosimetry, 117, 283

Park, W., Hammar, A., Pak, S., et al. 2020, Flight model characterization of the wide-field off-axis telescope for the MATS satellite

Park, W.-K., Pak, S., Im, M., et al. 2012, Publication of the astronomical society of the pacific, 124, 839

Ramesha, C. M., Abhijith, K. G., Singh, A., Raj, A., & Naik, C. S. 2015, IJETAE, 5, 323

Samei, E., Flynn, M. J., & Reimann, D. A. 1998, Medical Physics, 25, 102

Sasian, J. M. 1994, Optical Engineering, 33, 2045

Schmitt, D.-R. 1990, Proc. SPIE, 1125, 94

Schroeder, D. J. 2000, Astronomical Optics (San Diego: Academic Press)

Smith, W. J. 2007, in Modern Optical Engineering, 4th Ed (McGraw-Hill Education), 356–360

Song, N., Yin, Z., & Hu, F. 2002, Optical Engineering, 41, 2353

Trappey, J. C., & Liu, C. R. 1990, Int. J. Adv. Manuf. Technol., 5, 240

Trubert, M. 1989, Mass acceleration curve for spacecraft structural design

Vladimir Sacek. 2019, Telescope-optics, https://www.telescope-optics.net

Wang, Q., Cheng, D., Wang, Y., Hua, H., & Jin, G. 2013, Applied Optics, 52, C88

Wikipedia. 2020, Spherical aberration, https://en.wikipedia.org/wiki

Wu, K.-H., Lie, C.-C., Lin, Y.-C., et al. 2016, Proc. SPIE, 9947, 99470X

Zhang, X., Kashti, T., Kella, D., et al. 2012, Proc. SPIE, 829307, 829307

Reference Textbook

Warren J. Smith (2004). Modern Lens Design (2nd ed.). McGraw Hill Education. ISBN-13: 978-0071438308.

Warren J. Smith (2007). Modern Optical Engineering (4th ed.). SPIE Press. ISBN-13: 978-0071476874.

Michael Bass (2009). Handbook of Optics (3rd ed.). OSA. ISBN-13: 978-0071498890.

Robert E. Fischer (2008). Optical System Design (2nd ed.). McGraw-Hill Education. ISBN-13: 978-0071472487.

Hecht, Eugene (2002). Optics (4th ed.). Addison Wesley. ISBN-13: 978-0-321-18878-6.

Greivenkamp, John E. (2004). Field Guide to Geometrical Optics. SPIE. ISBN-13: 978-0-8194-5294-8.

Virendra N. Mahajan (1998, 2011, 2013). Optical Imaging and Aberrations: Part I, II, III. SPIE Press. ISBN: 9780819425157, 9780819486998, and 9780819491114.

H. P. Brueggemann (1968). Conic Mirrors. Focal press. ISBN-13: 978-0240506685

Keith B. Doyle, Victor L. Genberg, and Gregory J. Michels (2012). Integrated Optomechanical Analysis (2nd ed.). SPIE. ISBN: 9780819492487.

J. Jaap Wijker (2008). Spacecraft structures. Springer. ISBN-13: 978-3-540-75553-1. (for vibration analysis)

Thomas P. Sarafin and Wiley Larson (1995). Spacecraft structures and mechanisms. Springer. ISBN-13: 978-1881883036. (for vibration analysis)

Publications, Patents, and Presentations

Contents of this thesis is based on the publications [1], [2], [3], and [5]. Publication [4] is the paper for the Master degree.

Refereed Publications

[1] **Park, W.**, Hammar, A., Chang, S., Gumbel, J., Rouse, J., Megner, L., Kim, D. W., and Pak, S. 2020, "Optical performance and calibration of the wide-field off-axis telescope for the MATS satellite," Applied Optics, 59(17), 5335

[2] **Park, W.**, Pak, S., Chang, S., Lee, S., Kim, S., Jeong, B., Kim, G. H., Brendel, T. J., and Kim, D. W. 2020, "Transformable Reflective Telescope for optical testing and education," Applied Optics, 59(18), 5581.

[3] **Park, W.**, Pak, S., Chang, S., Lim, J. H., Lee, S., Ahn, H., Kim, Y., Kim, S., Hammar, A., Jeong, B., Kim, G. H., Kim, D. W. 2020, "Development of Linear Astigmatism Free – Three Mirror System (LAF-TMS)," Publication of the Astronomical Society of the Pacific, 132(1010), 044504

[4] **Park, W.**, Pak, S., Shim, H., Le, H. A. N., Im, M., Chang, S., and Yu, J. 2016, "Photometric transformation from RGB Bayer filter system to Johnson–Cousins BVR filter system," Advances in Space Research, 57(1), 509

[5] **Park, W.**, Pak, S., Chang, S., Lee, H., Lee, S., and Kim, D. W. "Optical sensitivity analyses of various reflective systems: on-axis, common off-axis, and confocal off-axis designs," Proc. SPIE, in preparation.

[6] Shin, S., Im, M., Kim, Y., Hyun, M., Pak, S., Jeon, Y., Ji, T-. G., Ahn, H., Byeon, S., Han, J., Hwang, S., Kim, S., Lim, G., Paek, I., Paek, G. S. H., Taak, Y. C., Choi, C., Hong, J., Jun, H. D., Kim, D., Kim, D., Kim, M., Kim, J-. W., Kim, J. H., Lee, H-. I., Lee, S-. K., Park, W-. K., **Park, W.**, and Yoon, Y. 2020, "The Infrared Medium-

deep Survey. VII. Faint Quasars at z $\sim$ 5 in the ELAIS-N1 Field", Astrophysical Journal, 893(45), 13

[7] Gumbel, J., Megner, L., Christensen, O. M., Chang, S., Dillner, J., Ekebrand, T., Giono, G., Hammar, A., Hedin, J., Ivchenko, N., Karlsson B., Kruse, M., Li, A., McCallion, S., Murtagh, D. P., Olentšenko, G., Pak, S., **Park, W.**, Rouse, J., Stegman, J., and Witt, G. 2020, "The MATS Satellite Mission – Gravity Waves Studies by Mesospheric Airglow/Aerosol Tomography and Spectroscopy", Atmospheric Chemistry and Physics, 20(1), 431.

[8] Im, M., Choi, C., Hwang, S., Lim, G., Kim, J., Kim, S., Paek, G. S. H., Lee, S-. Y., Yoon, S-. C., Jung, H., Sung, H-. I., Jeon Y-. B., Ehgamberdiev, S., Brhonov, O., Milzaqulov, D., Parmonov, O., Lee, S. G., Kang, W., Kim, T., Kwon, S-. G., Pak, S., Ji, T-. G., Lee, H-. L., **Park, W.**, Ahn, H., Byeon, S., Han, J., Gibson, C., Wheeler, J. C., Kuehne, J., Krull, C. J-., Marshall, J., Hyun, M., Lee, S-. K. J., Kim, Y., Yoon, Y., Paek, I., Shin, S., Taak, Y. C., Kang, J., Choi, S., Jeong, M., Jung, M-. K., Kim, H., Kim, J., Lee, D., Park, B., Park, K., and Seong, A. O. 2019, "Intensive Monitoring Survey of Nearby Galaxies (IMSNG)," Journal of the Korean Astronomical Society, 52(1), 11

[9] Hammar, A., **Park, W.**, Chang, S., Pak, S., Emrich, A., and Stake, J. 2019, "Wide-field off-axis telescope for the Mesospheric Airglow/Aerosol Tomography Spectroscopy satellite," Applied Optics, 58(6), 1393

[10] Kim, Y., Im, M., Jeon, Y., Kim, M., Pak, S., Taak, Y. C., Choi, C., Hong, J., Hyun, M., Ji, T-. G., Jun, H. D., Karouzos, M., Kim, D., Kim, D., Kim, J-. W., Kim, J. H., Lee, H-. I., Lee, S-. K., Park, W-. K., Yoon, Y., Byeon, S., Hwang S., Kim, J., Kim, S., Lim, G., Paek, I., **Park, W.**, and Shin, S. 2019, "The Infrared Medium-deep Survey. VI. Discovery of Faint Quasars at z$\sim$5 with a Medium-band-based Approach," Astrophysical Journal, 870(86), 19

[11] Hammar, A., Christensen, O. M., **Park, W.**, Pak, S., Emrich, A., and Stake, J. 2018, "Stray light suppression of a compact off-axis telescope for a satellite-borne instrument for atmospheric research," Proc. SPIE, 10815, 108150F

[12] Jeon, Y., Im, M., Kim, D., Kim, Y., Jun, H. D., Pak, S., Taak, Y. C., Baek, G., Choi, C., Choi, N., Hong, J., Hyun, M., Ji, T-. G., Karouzos, M., Kim, D., Kim, J-. W., Kim, J. H., Kim, M., Kim, S., Lee, H-. I., Lee, S-. K., Park, W-. K., **Park, W.**, and Yoon, Y. 2017, "The Infrared Medium-deep Survey. III. Survey of Luminous Quasars at $4.7 \leq z \leq 5.4$," Astrophysical Journal Supplement Series, 231(2), 16

[13] Kim, S., Jeon, Y., Lee, H-. I., **Park, W.**, Ji, T-. G., Hyun, M., Choi, C., Im, M., and Pak, S. 2016, "Development of SED Camera for Quasars in Early Universe (SQUEAN)," Publication of the Astronomical Society of the Pacific, 128(969), 115004

[14] Jeon, Y., Im, M., Pak, S., Hyun, M., Kim, S., Kim, Y., Lee, H-. I., and **Park, W.** 2016, "The Infrared Medium-Deep Survey. V. A New Selection Strategy for Quasars at $z > 5$ Based on Medium-Band Observations with SQUEAN," Journal of The Korean Astronomical Society, 49(1), 25

Patents

[1] "Off-Axis Optic Device in which Linear Astigmatism is Removed," Korean Intellectual Property Office, (Patent number 10-2023875, 2019)

[2] "Optical Filter Apparatus," Korean Intellectual Property Office, (Patent number 10-1815769, 2017)

[3] "Jig for Error Compensation Machining of Off-axis Mirror and Machining Method Thereof," Korean Intellectual Property Office, (Patent number 10-1802199, 2017)

[4] "Experiment device of reflecting telescope," Korean Intellectual Property Office, (Patent number 10-1749818, 2017)

Presentations

[1] **Park, W.**, Pak, S., Shim, H., Le, H.A.N., and Im, M. 2014, "Astronomical Photometry with the RGB Bayer Filter System," 4th Annual Meeting of Asia and Pacific Nation Network

[2] **Park, W.**, Pak, S., Shim, H., Le, H.A.N., and Im, M. 2014, "Photometry Transformation from RGB Bayer Filter System to Johnson-Cousins BVR Filter System," The Bulletin of the Korean Astronomical Society 39 (2), 104.2

[3] **Park, W.**, Pak, S., Shim, H., Le, H.A.N., Im, M., Chang, S., and Yu, J. 2014, "Photometry Transformation from RGB Bayer Filter System to Johnson-Cousins BVR Filter System," Goheung forum

[4] **Park, W.**, Pak, S., Kim, S., Lee, H-. I., Hyun, M., Shim, H., and Im, M. 2015, "Transformation of Filter Systems for Time-Domain Observations," The 3rd Workshop on Large Aperture Sub/mm Telescope in the ALMA Era

[5] **Park, W.**, Pak, S., Kim, S., Lee, H-. I., Hyun, M., Shim, H., and Im, M. 2015, "Transformation of Filter System for SQUEAN (SED camera for QUasar in EArly uNiverse)," The Bulletin of the Korean Astronomical Society 40 (1), 52.1

[6] **Park, W.**, Pak, S., Shim, H., Le, H. A. N., Im, M., Chang, S., and Yu, J. 2015, "Photometric transformation from RGB Bayer filter system to Johnson-Cousins BVR filter system," The Bulletin of the Korean Astronomical Society 40 (2), 43.2

[7] **Park, W.**, Pak, S., Shim, H., Le, H.A.N., Im, M., Chang, S., and Yu, J. 2016, "Derivation of Johnson-Cousins Magnitudes from DSLR Camera Observation," 227th Meeting of American Astronomical Society

[8] **Park, W.**, Chang, S., Pak, S., Kim, S., Kim, Y., and An, J. 2016, "Baffle design of Schwarzschild-Chang off-axis telescope," The 26th Workshop on Optical Technology

[9] **Park, W.**, Pak, S., Chang, S., Kim, G. H., Jeong, B., Kim, S., Lee, H-. I., Ji, T-. G., Gwak, J., Lee, K. J., Kim, H., Choi, S., and Park, S. 2016, "Development of TRT Kit for Optical Experiments with Reflective Telescopes," The Bulletin of the Korean Astronomical Society 41 (2), 52.3

[10] **Park, W.**, Lee, K. J., Pak, S., Gwak, J., Chang, S., and Jeong, B. 2017, "Characterization of Transformable Reflecting Telescopes," The 28th optical Society of Korea Winter Annual Meeting

[11] **Park, W.**, Pak, S., Chang, S., Jeong, B., Lee, K. J., Kim, Y., and Ji, T-. G. 2017, "Optic-axis Alignment and Performance Test of the Schwarzschild-Chang Off-Axis Telescope," The Bulletin of the Korean Astronomical Society 42 (1), 56.4

[12] **Park, W.**, Pak, S., Chang, S., Lee, S., Hammar, A., Jeong, B., and Lee, K. J. 2017, "Performance Test of the Schwarzschild-Chang Off-axis Telescope," The 3rd COSPAR symposium

[13] **Park, W.**, Pak, S., Chang, S., Kim, S., Kim, D. W., Lee, H., and Lee, K. J. 2017, "Design of Linear Astigmatism Free Three Mirror System (LAF-TMS) for Sky Monitoring Program," The Bulletin of the Korean Astronomical Society 42 (2), 88.1

[14] **Park, W.**, Hammar, A., Lee, S., Chang, S., and Pak, S. 2018, "Optical Performance Measurement of the MATS Satellite," The Bulletin of the Korean Astronomical Society 43 (1), 49.1

[15] **Park, W.**, Hammar, A., Lee, S., Chang, S., and Pak, S. 2018, "Optical Performance Measurement of the Swedish science satellite, MATS," International year of light workshop

[16] **Park, W.**, Hammar, A., Lee, S., Chang, S., Kim, S., Jeong, B., Kim, G. H., Kim, D. W., and Pak, S. 2018, "Mirrors and Optomechanical Structures Design and Analysis for Linear Astigmatism Free – Three Mirror System (LAF-TMS)," The Bulletin of the Korean Astronomical Society 43 (2), 55.4

[17] **Park, W.**, Hammar, A., Pak, S., Chang, S., and Gumbel, J. 2019, "Optical performance measurement of the Swedish atmospheric-research microsatellite, the MATS satellite," Instrumentation for Astronomy and Space Science

[18] **Park, W.**, Lim, J. H., Lee, S., Hammar, A., Kim, S., Kim, Y., Jeong, B., Kim, G. H., Chang, S., and Pak, S. 2019, "Optomechanical Design and Vibration Analysis for Linear Astigmatism Free Three Mirror System (LAF TMS)," The Bulletin of the Korean Astronomical Society 44 (2), 47

[19] **Park, W.**, Hammar, A., Pak, S., Chang, S., Gumbel, J., and Kim, D. W. 2019, "Optical calibration and performance measurement of the Mesospheric Airglow/Aerosol Tomography Spectroscopy (MATS) satellite," The Bulletin of the Korean Space Science Society 28 (2), 8

국문 초록

광학계 개발은 광학, 기계공학, 전자공학 등 여러 학문이 복합적으로 적용되는 종합학문이다. 지난 10여년 동안 광학계는 산업과 학술연구 모든 분야에서 급격한 성장을 이뤄왔다. 특히 천체망원경은 그 크기가 커지고 복잡해지면서 이를 개발하는데 다양한 분야의 최신기술들이 요구된다. 이 논문에서는 천체망원경에 적용되는 광학계의 설계 및 평가 방법을 소개한다. 이는 광설계, 공차분석, 정렬, 성능평가, 광학성질평가, 광기계부 설계 및 해석, 그리고 산란광 차단에 관한 내용을 포함한다. 또한, 논문의 이해를 돕기 위해 간단한 광학 및 수차 이론이 논문 초반부에서 소개된다. 본 논문은 주로 LAF-TMS와 MATS 인공위성, 두 개의 동초점 비축 광학계를 기반으로 한다. 두 광학계 모두 선형비점수차가 제거된 광학 설계 이론을 바탕으로 개발되었으며, 넓은 시야각에 걸쳐서 매우 좋은 광학 성능을 보여준다. 독특한 광학 이론 덕분에 독창적인 광설계, 정렬, 그리고 반사경과 광기계부 설계가 이루어졌다. 광학계 실험 장치인 TRT Kit도 정렬, 산란광 분석 및 배플 설계의 예제로 소개된다. 이 논문에서 소개되는 모든 설계 및 해석 방식은 선형비점수차가 제거된 비축 반사 광학계뿐만 아니라 다른 일반적인 광학계 개발에도 활용될 수 있다.